Investigation into the Role of Ions and Excited Molecules in the Corona Process in Air

Andrew Graham Swanson

June 29, 2015

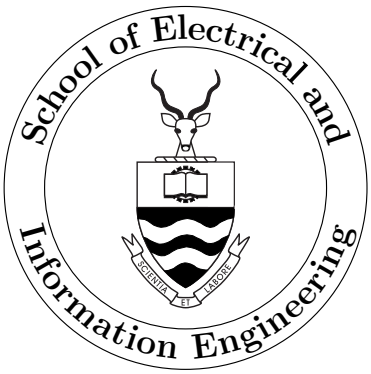

Investigation into the Role of Ions and Excited Molecules in the Corona Process in Air

Andrew Graham Swanson

June 29, 2015

A thesis submitted to the Faculty of Engineering and the Built Environment, University of the Witwatersrand, Johannesburg, in fulfilment of the requirements for the degree of Doctor of Philosophy.

Johannesburg, June 29, 2015

Declaration

I declare that this thesis is my own, unaided work, except where otherwise acknowledged. It is being submitted for the degree of Doctor of Philosophy to the University of the Witwatersrand, Johannesburg. It has not been submitted before for any degree or examination to any other university.

Signed this _____ day of _____ 2015

_____

Andrew Graham Swanson

Abstract

Corona is the partial breakdown of a gas in an electric field and involves many complex phenomena including the production of space charge and excited molecular states of its constituents. Air is predominantly made up of nitrogen and oxygen, both of which have a wide range of excited states. Oxygen itself is additionally an electronegative gas and has the ability to attach electrons. Together these phenomena combine to influence the electric field and the production of secondary electrons to give corona its distinctive modes.

A particular state of excited molecular oxygen, known as singlet oxygen, has the characteristic that it remains excited for a relatively long period of time. It is known that singlet oxygen plays a role in the detachment of electrons from the negative oxygen ions and its role in corona discharges has been accounted for through theory and models, but due to the difficulties of measurement of the singlet oxygen, the influence it does have on corona discharges is not entirely clear.

On this basis the gas processes associated with the corona discharge in air

have been explored, where a Boltzmann equation solver, the electron energy distribution function, transport coefficient and Townsend coefficients are used to understand the phenomena and provide input to a flux correct transport algorithm model. The model clearly indicates the presence of singlet oxygen, however its the space charge that plays the critical role in the repetitive nature of corona due to the collapse and recovery of the electric field.

Experimentally it was convenient to define and compare the modes of corona under different conditions by its peak amplitude and repetition rate. The experiments included manipulated the environment with air-flow and exciting oxygen through a 1064 nm Nd:YAG laser as well as detecting 1270 nm emission from singlet oxygen. There was no evidence to suggest that the repetition rate of the corona discharge could be related to singlet oxygen. There were no emissions detected from various configurations, whilst visible corona was clearly seen.

Together with the evidence from the model, the results showed that the presence of both negative ions and singlet oxygen is relatively low in the region that should provide seed electrons. It could be inferred that a relationship between repetition rate and the presence of singlet oxygen is not a dominant process in the corona discharge.

Acknowledgements

I would like to thank my family and friends for keeping me together throughout my studies. I would like to thank Ian Jandrell who supported and encouraged the research as well as Michael Grant, Thavenesen Govender, Nicholas West, Hugh Hunt, Ken Nixon, Cuthbert Nyampangedengu, Jessie Liu, John van Coller, Ivan Hofsajer, and Jan Reynders for the interesting and thought provoking ideas and discussions on the subject as well as for the entertainment.

I would like to thank Roel Stolper from the CSIR for the loan of lenses to aid in the detection experiments and Bathusile Masina and Thomas du Plooy from the CSIR National Laser Centre for allowing the use of the Nd:YAG laser for the experiments.

I would like to thank Eskom for the support of the High Voltage Engineering Research Group through the TESP programme. I would also like to thank CBI-electric for support, the department of Trade and Industry (DTI) for THRIP funding as well as to the National Research Foundation (NRF) for direct funding.

Contents

List of Figures

List of Tables

List of Symbols

The list of symbols and constants used in the thesis are summarised below, where the units are given in square brackets and the equation number in round brackets. Refer to the local definitions should the symbol be repeated.

f	Distribution function, Equation (2.1), (2.2), (2.7), (2.8), (2.10)
m	Mass [g], Equation (2.1), (2.2), (2.7), (2.8)
T	Temperature [K], Equation (2.1), (2.2)
v_i	Velocity of particle [m.s^{-1}], Equation (2.1), (2.2)
s	Speed of particle [m.s^{-1}], Equation (2.1), (2.2)
$\vec{F}$	Lorentz force [N], Equation (2.3)
q	Charge [C], Equation (2.3), (2.7), (2.8)
$\vec{E}$	Electric field [V.m^{-1}], Equation (2.3), (2.7), (3.1)
$\vec{v}$	Velocity of particle [m.s^{-1}], Equation (2.3), (2.7), (3.1)
$\vec{B}$	Magnetic field strength [T], Equation (2.3), (3.1)
σ	Collisional cross-section [cm^2], Section (2.1.1)
N	Neutral number density [cm^{-3}], Equation (2.8), (2.9), (2.10)
ε	Energy [eV], Equation (2.8), (2.10)
μ	Mobility [cm^2.V^{-1}.s^{-1}], Equation (2.8), (2.9), (2.10), (2.14)
v_d	Drift velocity [cm.s^{-1}], Equation (2.9), (2.14)
α_k	Townsend coefficient [cm^{-1}], Equation (2.10)
ν	Photon energy [eV], Equation (2.10)
W_a	Material Work function [eV], Equation (2.17)
W_k	Particle kinetic energy [eV], Equation (2.17)
W_p	Particle potential energy [eV], Equation (2.17)

$i(t)$	Current [mA], Equation (2.18), (2.19)
i_p	Peak current [mA], Equation (2.17), (2.19)
$N_{e/p/n/o}$	Number densities of electron, positive ions, negative ions and singlet oxygen [cm^{-3}], Equation (3.3), (3.4), (3.5), (3.6)
$v_{e/p/n}$	Velocity of electron, positive ions, negative ions [$cm.s^{-1}$], Equation (3.3), (3.4), (3.5), (3.6)
α	Ionisation coefficient [cm^{-1}], Equation (3.3), (3.4)
η	Attachment coefficient [cm^{-1}], Equation (3.3), (3.5)
ψ	Singlet oxygen coefficient [cm^{-1}], Equation (3.5).
S	Photoionisation term [$C.cm^{-3}$], Equation (3.3), (3.4)
β	Recombination coefficient [$cm^3.s^{-1}$], Equation (3.3), (3.4), (3.5).
$D_{e/p/n}$	Diffusion coefficient [$cm^2.s^{-1}$], Equation (3.3)
k_d	Detachment rate coefficient [$cm^3.s^{-1}$], Equation (3.5), (3.6)
k_q	Quenching rate coefficient [$cm^3.s^{-1}$], Equation (3.5), (3.6)
N_P	Number of photo ion pairs produced per second [$cm^{-3}.s^{-1}$], Equation (3.7)
N_D	Number of ions pairs produced per second [$cm^{-3}.s^{-1}$], Equation (3.7)
ϕ	Space potential [V], Equation (3.11)
ρ	Space charge density [$C.cm^{-3}$], Equation (3.11)
E_L	Laplacian electric field [$V.cm^{-1}$], Equation (3.14)
E_P	Poissonian electric field [$V.cm^{-1}$], Equation (3.14)
$\sigma_{+,-}$	Surface charge of cathode and anode, Equation (3.15)
$A_{+,-}$	Surface area of cathode and anode, Equation (3.15)
$I(t)$	Current [A], Equation (3.16), (3.17)
V_A	Applied voltage [V], Equation (3.17)
R	Resistance [Ω], Equation (3.17)
λ_D	Debye Length [m], Equation (3.20)

$\vec{J}_c$	Conductive current density [A.m^{-2}], Equation (4.1)
$\vec{J}_d$	Displacement current density [A.m^{-2}], Equation (4.1)
W	Energy [J]
$\vec{J}$	Current density [A.m^{-2}], Equation (4.4)
W_{loss}	Energy loss [J], Equation (4.4), (4.5), (4.6)
P_{ave}	Average power [W], Equation (4.4), (4.9)

The list of constants used in the thesis are summarised below, where the values and units are given in square brackets and the equation number in round brackets. The constants are used in multiple equations as such the equation number is not given.

ϵ_0	Permittivity of free space [8.85×10^{-12} F.m^{-1}]
k_B	Boltzmann's constant [1.38×10^{-23} J.K^{-1}]
h	Plank's constant [6.626×10^{-34}m^{2}kgs^{-1}]
q_e	Charge of an electron [-1.6×10^{-19} C]
m_e	Mass of an electron (at rest) [9.11×10^{-31} kg]

Chapter 1

Introduction

Corona is the partial breakdown of a gas and is caused by the acceleration and collision of various charged particles in a high electric field. Corona presents a high complex gas discharge phenomena due to its various modes, some of which are repetitive in nature. High voltage engineers consider corona as a source of radio interference, audible noise, electromagnetic interference and power loss, while corona under AC conditions has been more understood than under HVDC conditions. There is a need for ongoing research due to the non-linear nature of the phenomena, notably the influence the space charge has on the electric field and the subsequent influence on the mechanisms and modes of corona.

The gas discharge in air is a highly complex mechanism that involves processes that lead to numerous states of its constituents including positive ions, negative ions and excited states. The behaviour of these states contribute directly to the gas discharge process. Coupled to this under HVDC conditions the problem becomes more complex due to this space charge which alters the behaviour of corona over a longer duration. The complexity is explored in the thesis with the emphasis on a metastable state of oxygen also know as singlet oxygen.

An interesting occurrence in an experiment where airflow was applied to

positive onset streamers informed the direction of the thesis. Further investigating the corona process by looking at the fundamental electron collisions brought attention to the reactions that were involved in the corona process. One particular set of reactions that has been proposed by Lowke to be a major contributing factor in gas discharges is the production of singlet oxygen and the subsequent detachment of electrons due to the negative ion and singlet oxygen reaction [1, 2]. Morrow subsequently included the set of reactions in the theory of positive glow as a major contributing factor of seed electrons [3]. Singlet oxygen itself is the lowest electronic excited state of molecular oxygen and is one of the excited states that has been taken into account in only a few numerical studies.

The research direction was informed by the initial experiment and a model was developed to identify the role of singlet oxygen under negative and positive conditions. The model was to be used to identify the influences that the reaction between singlet oxygen and negative ions could have. A number of experiments would be undertaken based on the conclusions established from the modelling and would include the detection of singlet oxygen and the excitation of singlet oxygen in the system.

1.1 Hypothesis

It has been stated that space charge plays a dominant role in the mechanism of corona under both negative and positive coronas. The role it plays differs greatly between the two and while negative corona in the form of Trichel pulses is also dependent on electron release through cathode processes to aid in initialisation, it is not known whether there is a similar characteristic in positive corona. It has also been stated that singlet oxygen, which is a metastable state of oxygen, plays an important role in the detachment of electrons, which may become seed electrons to initialise a discharge in such a manner as to cause the onset streamers to repeat, which to the best of the authors knowledge, has not been measured, tested nor quantified.

This study therefore postulates that singlet oxygen excited at 0.97 eV has an influence on the creation of seed electrons for corona and that a relationship may be drawn between excited oxygen and the repetition rate of onset streamers.

1.2 Importance of Study and Contribution

In the field of high voltage engineering, it is essential to understand the physics behind the gas discharge. The thesis presents a 1.5 dimensional model of a gas discharge with the emphasis on the extended period of the gas discharge. While this is not unique in itself, the importance of the research is the manner in which the model was used to investigate the role of a specific excited state of oxygen and provides a basis for analysing any of the excited states of N_2 or O_2 in the corona and gas discharge processes and could be further extended to other insulating gases and engineering applications such as the design of transmission lines and outdoor high voltage equipment as well as circuit breakers that contain any type of gaseous insulation.

The thesis investigates the role of a particular state of excited oxygen, namely singlet oxygen and identifies the role of the singlet oxygen in the corona process in air. Positive corona in particular needs to be initiated through electrons in the air, any repetitive nature of positive corona, such as positive onset streamers would require a constant supply of electrons. The thesis contributes to the body of knowledge of the role of singlet oxygen through the modelling both negative and positive corona and through a set of experiments that have not been done in this manner previously.

1.3 Structure

The thesis has been structured as follows:

Chapter 2 - Theory of Gas Discharges and Corona

The relationship between the gas discharge and the Maxwell-Boltzmann distribution equation is discussed. A discussion of the mechanism of positive and negative corona and on the role of singlet oxygen in a gas discharge is presented. Together these set the foundation for the following modelling and experimentation chapters .

Chapter 3 - Modelling of Gas Discharges and Corona

Modelling of gas discharges is discussed, where the fluid approach is promoted and described. The results for positive and negative corona with a discussion focused on the role of the space charge and the role of singlet oxygen are presented.

Chapter 4 - Experiments

The measurement system and experiments are described and assessed including the testing of positive and negative corona, altering the system through air flow, relating corona to energy and power, the measurement of the near infrared emissions to detect singlet oxygen and impact of a Nd:YAG laser to influence the density of singlet oxygen.

Chapter 5 - Conclusion

The conclusions reached and recommendations drawn from the thesis are formulated.

Appendix A - Electric Field Solver

The electric field plays a dominant role in the process of corona. The appendix describes the electric field and presents the algorithm to solve for the electric field through the finite difference method.

Appendix B

Here it is shown how a discrete coupled circuit equation for the models for a coupling capacitor and a series resistor measurement system are derived.

Appendix C

Important aspects related to the Bohr model and the kinetic theory of gases are summarised and provided. The appendix also provides a more comprehensive coverage of aspects such as mean free path, collisional cross-section and energy transfer than Chapter 2.

Appendix D - Plasma Physics

Aspects of plasma physics referred to in Chapter 3 are described.

Appendix E - Modelling

Details of the numerical algorithm are described including the high and low orders solvers, the flux limiters, diffusion, and source term integration.

Appendix F - Detector Calibration

The infrared detector and lens used to measure the emissions from corona was calibrated through an incandescent lamp is described.

Appendix G - Code

The appendix provides the full code for the algorithm.

Appendix H - Results

The test vessel is presented and the experimental methodology and results together with environmental conditions are tabulated.

Appendix I - Associated Publications

The associated publications are listed.

Chapter 2

Theory of Gas Discharges and Corona

The chapter presents the fundamentals of gas discharges in air and is considered critical for understanding the following chapters as it lays the basis for understanding the hypothesis and complexity of the processes involved. The kinetic theory of gases is reviewed with an emphasis on the probability of energy levels under thermal equilibrium and an electric field. The electron energy distribution function and the cross sectional area are introduced as these concepts are used to derive the Townsend coefficients, the transport coefficients and mean electron energies for air. The theory of positive and negative corona is presented with an emphasis on the role of ions and singlet oxygen in the gas discharge.

2.1 Kinetic Theory of Gases

Particles of a gas are in constant random motion, which can be related to the temperature and molecular weight of the gas. For a gas in thermal equilibrium, the Maxwell-Boltzmann probability distribution is used to describe the probability of finding a particle with velocity (v_x, v_y, v_z) as given by the

equation [4]:

$$f(v) = \left(\frac{m}{2\pi k_B T}\right)^{\frac{1}{2}} \exp\left(-\frac{mv_i^2}{2k_B T}\right) \tag{2.1}$$

Where:

m = Mass of the particle [g]
k_B = Boltzmann's constant
T = Temperature [K]
v_i = Velocity of particle [m.s^{-1}]

The Maxwell-Boltzmann probability distribution function for electron speed, s, for different gas temperatures is illustrated in Figure 2.1 according to the equation:

$$f(s) = 4\pi \left(\frac{m}{2\pi k_B T}\right)^{\frac{3}{2}} s^2 \exp\left(-\frac{ms^2}{2k_B T}\right) \tag{2.2}$$

Where:

s = Speed of particle [m.s^{-1}]

It is evident from the graph that the higher the temperature the greater the probability of finding an electron at a higher speed.

Microscopically these particles are in constant collision with other particles in the gas and the collisions generally form two types [4]:

- an elastic collision where energy exchange is kinetic referred to as a momentum collision
- an inelastic collision where kinetic energy is transferred into potential energy where the potential energy could excite a molecule into a rotational, vibrational, or electronic state, or could cause attachment to and ionisation of the molecule.

The type of collision depends on a probability related to the energy of the

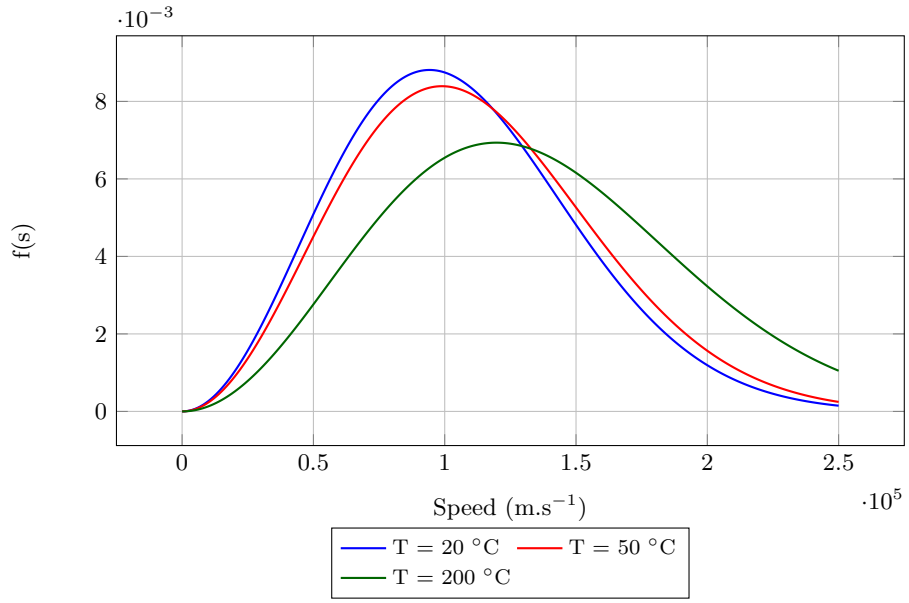

Figure 2.1: Maxwell-Boltzmann Distribution of Speed

particle as it is energy that needs to be transferred to the molecule to change in state. Rewriting the distribution in terms of energy where $\varepsilon = \frac{1}{2}m\vec{v}^2$ is a useful concept in understanding this. Figure 2.2 illustrates an example of the probability distribution in terms of energy and indicates that a minimum energy ε_{ion} is required for an ionisation reaction to take place upon a collision. This concept is explored further by applying an external stress or electric field.

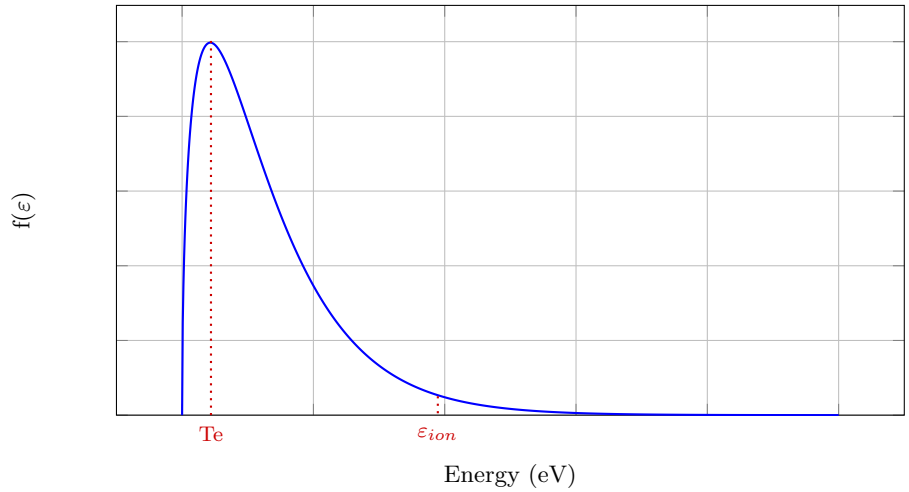

Figure 2.2: Electron Energy Distribution Function

The presence of an electric or magnetic field has the effect of accelerating a charged particle in the direction of the field through the Lorentz force [5]:

$$\vec{F} = q(\vec{E} + \vec{v} \times \vec{B}) \tag{2.3}$$

Where:

$\vec{F}$ = Force exerted on the particle [N]
q = Charge of particle [C]
$\vec{E}$ = Electric field [V.m^{-1}]
$\vec{v}$ = Velocity of particle [cm^{-1}]
$\vec{B}$ = Magnetic field [T]

The charged particles are accelerated and will experience collisions and a corresponding loss of energy. Specifically considering electrons in the electric field, the electron may gain enough kinetic energy that upon an inelastic collision with a neutral particle enough energy will be transferred to the particle to release another electron (Figure 2.3) or to excite the molecule to a higher energy state (Figure 2.4) [4].

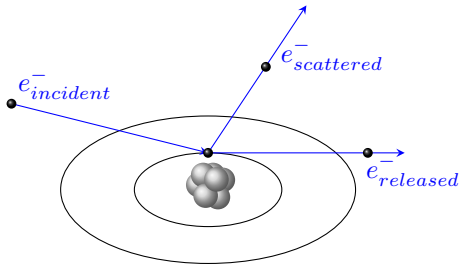

Figure 2.3: Ionisation by Collision

The ionisation reaction is represented by the equation [4]:

$$X + e^- = X + e^- + e^- \tag{2.4}$$

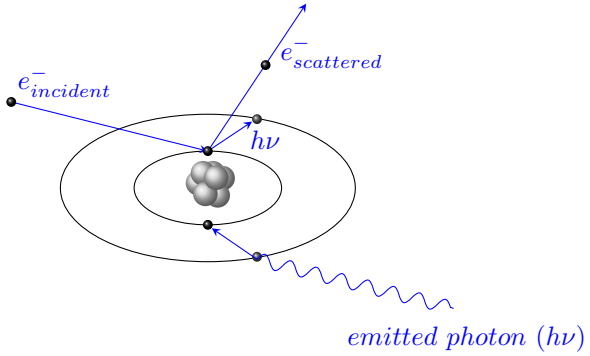

Figure 2.4: Electronic Excitation by Collision

The excitation reaction is represented by the equation [4]:

$$X + e^- = X^* + e^- \tag{2.5}$$

An electron will remain in an excited state for a certain time before it emits the energy in the form of a photon and returns to its normal state.

In the presence of oxygen, an electronegative gas, an electron could also become attached to the gas particle and form a negative ion as represented

by the reaction equation [4]:

$$O_2 + e^- = O_2^- \tag{2.6}$$

Each inelastic collision, including those that cause rotational and vibrational excitations, performs a role in the probability of an electron having a certain energy and the performance characteristic of the gas under the electrical stress.

2.1.1 Collisional Cross-Sections

All of the elastic and inelastic collisional reactions are based on a probability phenomenon related to the energy of an electron and a collisional cross-section, σ, for each type of reaction [4], where the collisional cross-section is defined as the cross-sectional area for interception relating the area of the colliding particle to the area of the struck particle $\sigma = \pi(r_1 + r_2)^2$ [4].

Electron Collisions in Nitrogen

The collisional cross-sections for Nitrogen are illustrated in Figure 2.5 and tabulated in Table 2.1. The cross-sections are based on the data collated by Itikawa [6, 7]. The data from the LXcat database, which is used for the modelling, is similar [8, 9]. Figure 2.5 illustrates only the momentum, electronic excitation and ionisation cross sections, while Table 2.1 lists the entire range of reactions including the energy transferred for the reaction, the maximum cross-section and the wavelength of an emission. It is evident that for an electron with any given energy that there are a number of reactions that could take place where the most likely is the momentum collision for the whole range of energies. As the electron energy increases the ionisation cross-section tends towards the momentum cross-section. There are multiple excited states of nitrogen, which act as energy sinks and is the reason it is often considered a good insulator, as these excited states retard the growth of a streamer.

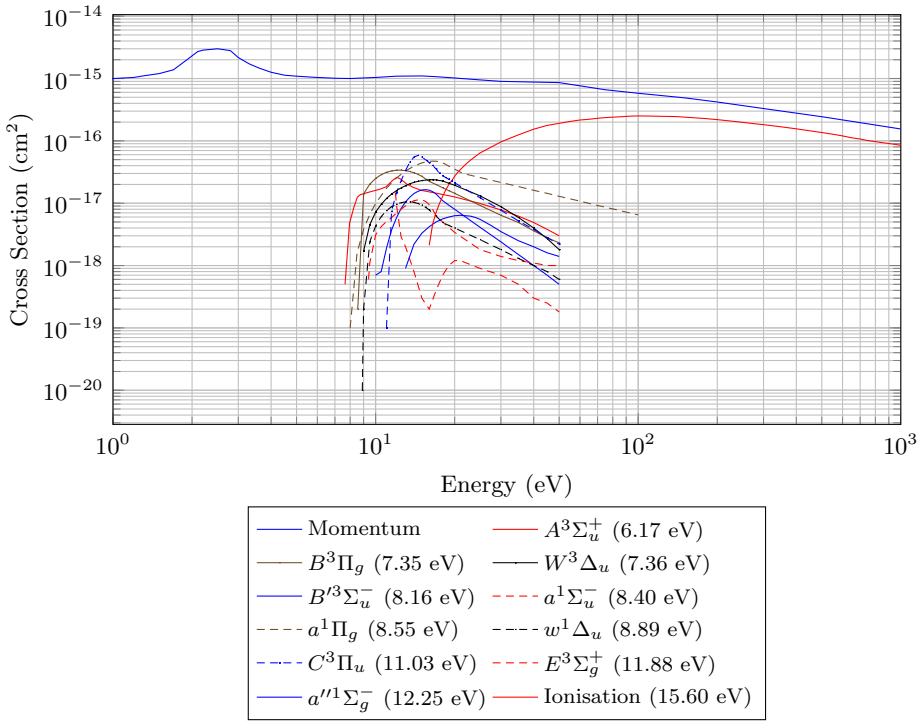

Figure 2.5: Electron Collision Cross-Sections in Nitrogen

Table 2.1: Electron Collision - Characteristics of Nitrogen

Reaction	Energy (eV)	Max Cross-Section (10^{-16} cm^2)	Wavelength (nm)
N_2 Momentum	0.00	30.00	0.0
N_2 Rotational	0.02	6.90	0.0
N_2 Vibrational (v=1)	0.29	2.565	0.0
N_2 Vibrational (v=2)	0.59	2.115	0.0
N_2 Vibrational (v=3)	0.88	2.055	0.0
N_2 Vibrational (v=4)	1.17	2.385	0.0
N_2 Vibrational (v=5)	1.47	1.53	0.0
N_2 Vibrational (v=6)	1.76	1.74	0.0
N_2 Vibrational (v=7)	2.06	0.96	0.0
N_2 Vibrational (v=8)	2.35	0.36	0.0
N_2 Excitation $A^3\Sigma_u^+$	6.17	0.257	199.66
N_2 Excitation $B^3\Pi_g$	7.35	0.339	167.61
N_2 Excitation $W^3\Delta_u$	7.36	0.238	167.38
N_2 Excitation $B'^3\Sigma_u^-$	8.16	0.165	150.97
N_2 Excitation $a^1\Sigma_u^-$	8.40	0.113	146.65
N_2 Excitation $a^1\Pi_g$	8.55	0.473	144.08
N_2 Excitation $w^1\Delta_u$	8.89	0.105	138.57
N_2 Excitation $C^3\Pi_u$	11.03	0.583	111.69
N_2 Excitation $E^3\Sigma_g^+$	11.88	0.148	103.70
N_2 Excitation $a''^1\Sigma_g^-$	12.25	0.064	100.56
N_2 Ionisation	15.60	2.510	78.97

Electron Collisions in Oxygen

The collisional cross-sections for Oxygen are illustrated in Figure 2.6 and tabulated in Table 2.2. The cross-sections are based on the data collated by Itikawa [10, 11]. The data from the LXcat database is again similar [9]. Figure 2.6 illustrates only the momentum, electronic excitation and ionisation cross sections, while Table 2.2 lists the entire range of reactions including the energy transferred for the reaction, the maximum cross-section and the wavelength of an emission. There are fewer excited states for oxygen when compared with nitrogen, there is however the additional attachment cross-section. In the case here the two-body attachment is included. It is evident that it is in a lower energy region of the graph when compared to the ionisation. The excited state $a^1\Delta_g$ is known as singlet oxygen and it is shown that the cross-section is spread over a wide range of energies.

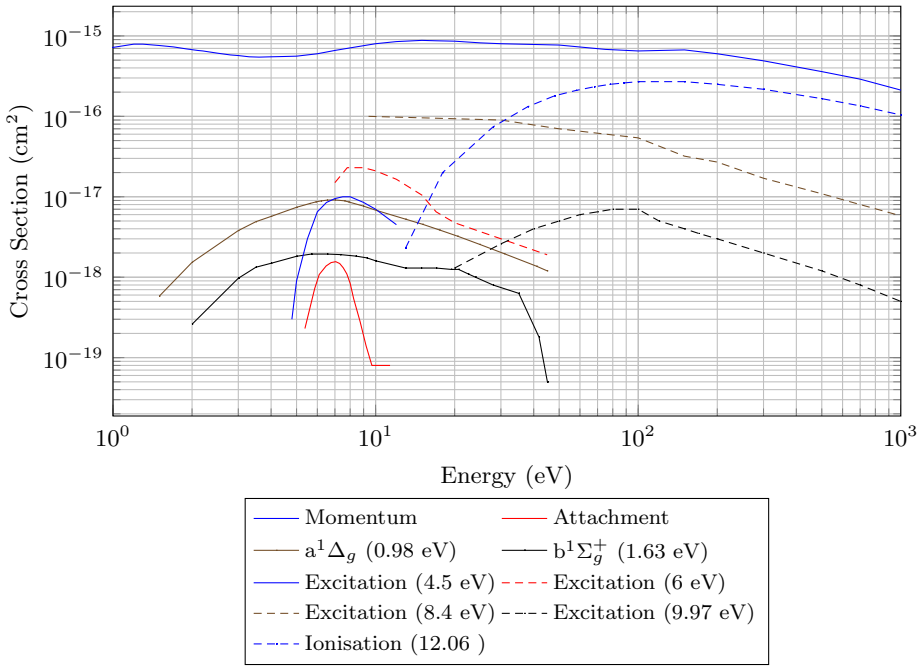

Figure 2.6: Electron Collision Cross-Sections in Oxygen

Table 2.2: Electron Collision - Characteristics of Oxygen

Reaction	Energy (eV)	Max Cross-Section (10^{-16} cm^2)	Wavelength (nm)
O_2 Momentum	0.00	8.800	0.0
O_2 Attachment	0.00	0.016	0.0
O_2 Rotational	0.02	0.094	0.0
O_2 Vibrational (v=1)	0.19	1.85	0.0
O_2 Vibrational (v=2)	0.38	0.535	0.0
O_2 Vibrational (v=3)	0.57	0.115	0.0
O_2 Vibrational (v=4)	0.75	0.046	0.0
O_2 Excitation $a^1\Delta_g$	0.97	0.091	1270.0
O_2 Excitation $b^1\Sigma_g^+$	1.63	0.019	755.77
O_2 Excitation	4.50	0.100	270.75
O_2 Excitation	6.00	0.230	205.32
O_2 Excitation	8.40	1.000	146.65
O_2 Excitation	9.97	0.700	123.56
O_2 Ionisation	12.00	2.700	102.66

2.1.2 Boltzmann Equation, EEDF and Coefficients

Bolsig is the Boltzmann equation solver used to determine the transport, rate and Townsend coefficients for the set of cross-sections. The coefficients involving electrons are dependent on the electron energy distribution function (EEDF), which is a convenient function used to describe the distribution of electron energies under various conditions [12].

The Boltzmann equation is given by [12]:

$$\frac{\partial f}{\partial t} + \vec{v}.\nabla f - \frac{q}{m}\vec{E}.\nabla_V f = \left(\frac{\partial f}{\partial t}\right)_{collision} \tag{2.7}$$

Where:

$\vec{v}$ = Velocity of electron [m.s^{-1}]
q = Charge of electron [C]
m = Mass of electron [g]
$\vec{E}$ = Electric field [V.m^{-1}]

Solving the Boltzmann equation for a mixture approximating air of N_2 78% and O_2 22 % gives the EEDFs illustrated in Figure 2.7. It is shown that the application of an electric field is the dominant factor in the distribution of electron energies. As expected the higher the electric field, the higher the energy levels that the electrons achieve i.e. a larger number of electrons will lead to ionisation. This does not however mean that the other reactions are neglected as it can be seen that for 125 kV.cm^{-1}, there is still a large proportion of electrons under 12 eV (the ionisation energy of oxygen). This supports the concept and use of electric field to determine the Townsend or rate coefficients for fluid modelling.

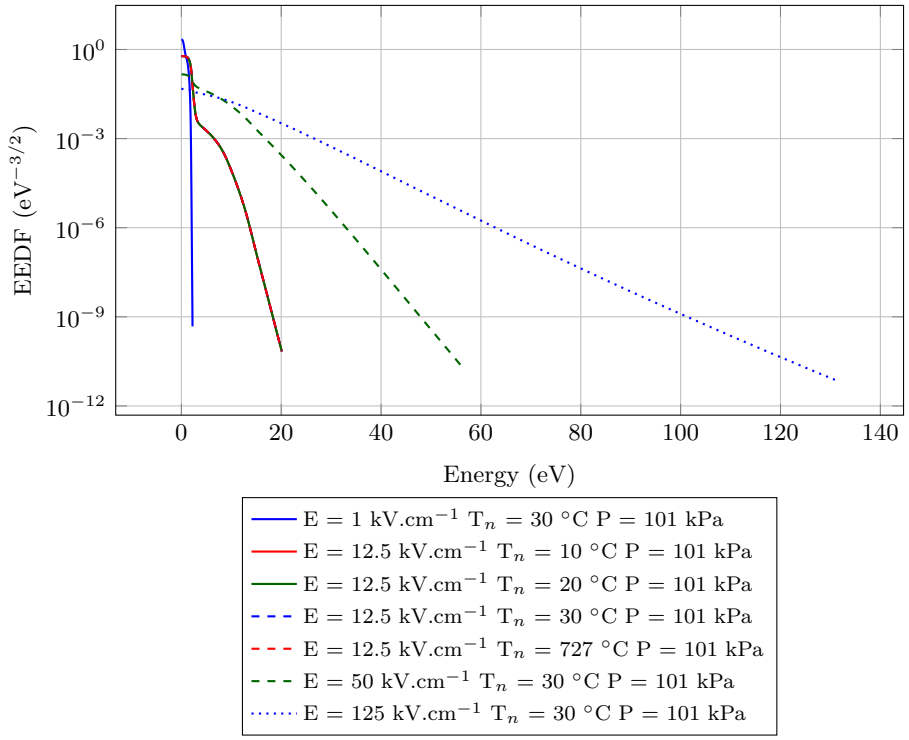

Figure 2.7: Electron Energy Distribution Function in Air

The mobility of electrons is described by the integral relationship between the energy and all collisional cross-sections as follows [12]:

$$\frac{\mu}{N} = -\frac{1}{3}\sqrt{\frac{2q}{m}}\int_0^\infty \frac{\varepsilon}{\sigma_m}\frac{\partial f}{\partial \varepsilon}d\varepsilon \tag{2.8}$$

Where:

μ = Mobility of electron [cm^2.V^{-1}.s^{-1}]]

N = Number density of neutral [cm^{-3}]

ε = Energy of electron [eV]

σ_m = Total collisional cross-section [cm^2]

The mobility is used to determine the drift velocity of the electron for a given electric field. The drift velocity, v_d, is given by [4]:

$$\vec{v_d} = \mu\vec{E} \tag{2.9}$$

In Figure 2.8 the drift velocity for air is determined through the mobility calculated from Bolsig and compared with that of Morrow [3, 13]. It is shown that the velocities are similar.

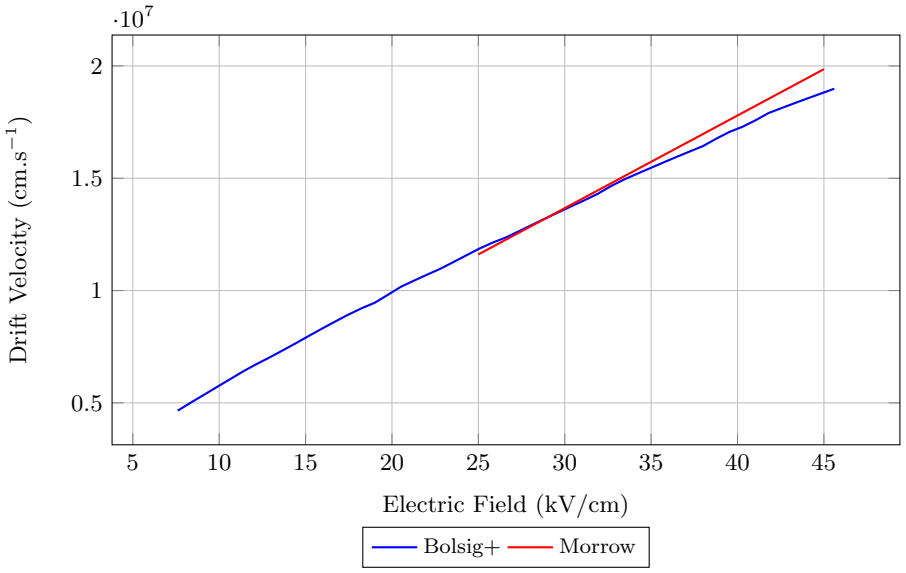

Figure 2.8: Drift Velocity of Electrons

The Townsend coefficients can be determined for each type of collision, in particular for collisions where particles are lost or gained, by the integral relationship of the particle energy, electric field and cross-section using the following equation [12]:

$$\frac{\alpha_k}{N} = \sqrt{\frac{2q}{m}} \frac{\int_0^\infty \varepsilon \sigma_k f d\varepsilon}{\mu E} \tag{2.10}$$

Where:

σ_m = Collisional cross-section of collision type k [cm^2]

The calculated Townsend coefficients for ionisation and attachment are illustrated in Figure 2.9 and compared with measured data by Geballe and Harrison and published data from Morrow [3, 4, 13, 14]. There are some differences in the data, referring to the ionisation, it should be noted that the Bolsig coefficients only include the collisional data, whereas the measured data would be influenced by other means. The Bolsig data is additionally valid across a wider range of electric fields.

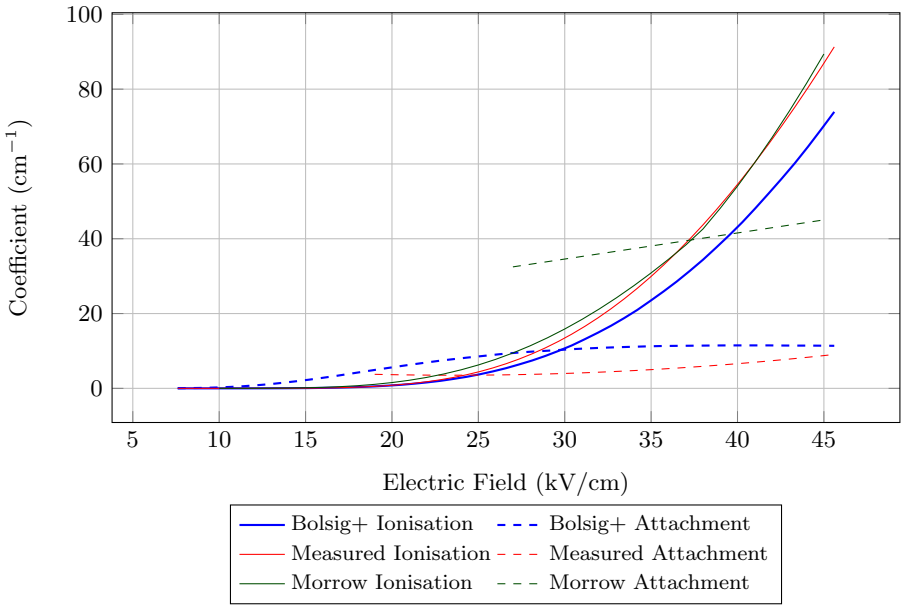

Figure 2.9: Coefficients

2.1.3 Ion Collisions and Mobilities

The ionisation and attachment processes produce positive and negative ions which through the Lorentz force gain energy from the electric field, accelerate and collide with each other or the neutral which may result in recombination, and electron detachment [4].

Recombination is represented by [4]:

$$O_2^- + X^+ = O_2 + X \tag{2.11}$$

Electron detachment with a neutral is represented by [4]:

$$O_2^- + X = O_2 + X + e \tag{2.12}$$

Electron detachment with an excited state is represented by [4]:

$$O_2^- + X^* = O_2 + X + e \tag{2.13}$$

The acceleration of the ions and the collisions lead to the concept of drift velocity and the concept of mobility which is the drift velocity per unit strength of field [4]:

$$\mu = \frac{v}{E} \tag{2.14}$$

The mobility values for positive and negative ions in air have been measured as 1.36 and 2.1 $cm^2.V^{-1}.s^{-1}$ respectively [4]. Mobility values of 2.34 and 2.7 $cm^2.V^{-1}.s^{-1}$ are, however, used in the fluid models implemented by Morrow [3, 13].

2.1.4 Photoionisation and Photoemission

Any photon with a high enough energy may cause an electron to be released from a molecule or to be excited to a higher energy state [4]:

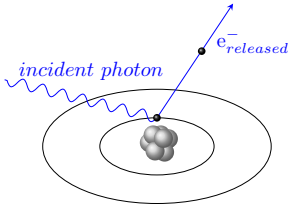

Figure 2.10: Photoionisation

The photoionisation reaction shown in Figure 2.10 is represented by [4]:

$$X + h\nu = X^+ + e \tag{2.15}$$

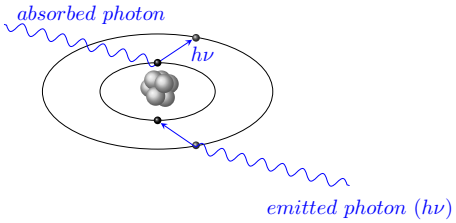

Figure 2.11: Photoexcitation

The photoexcitation reaction shown in Figure 2.11 is represented by [4]:

$$X + h\nu = X^* + e \tag{2.16}$$

The electron will remain in an excited state for a certain time before it emits the energy as a photon of the same wavelength and returns to its normal state. These photons may be emitted by molecules in the gas itself and may through photon absorption cause excitation or ionisation in other molecules. Tables 2.1 and 2.2 list the wavelengths of the electronic excited states of nitrogen and oxygen. It is shown that photons emitted from the highest excited state of nitrogen ($a''^1\Sigma_g^-$) have an energy of 12.25 eV and corresponding

wavelength of 100.56 nm, which is sufficient to excite or ionise oxygen.

Additionally Table 2.3 lists the wavelengths and corresponding photon energy of a part of the electromagnetic spectrum. Correlating the information shown with that of Tables 2.1 and 2.2, it can be seen that numerous reactions and wavelengths overlap particularly in the UV range.

Table 2.3: Electromagnetic Spectrum

Wavelength (nm)	Energy (eV)	Details
10-390	124.02-3.18	Ultraviolet
390-455	3.18-2.73	Violet
455-492	2.73-2.52	Blue
492-577	2.52-2.15	Green
577-600	2.15-2.07	Yellow
600-625	2.07-1.99	Orange
625-760	1.99-2.07	Red
760-3000	1.63-0.41	Near infrared
3000-50×10^3	0.41-0.025	Mid infrared
50×10^3-1×10^6	0.025-0.001	Far infrared

2.1.5 Cathode Processes

As the gas discharge is bounded by electrodes, it is important to account for the processes at this boundary.

Positive Ion Bombardment

A positive ion striking the cathode may cause electron emission, the energy is required to be twice the work function as two electrons are required, the first to neutralise the ion and the second to be released into the system [4].

$$W_k + W_p \geq 2W_a \tag{2.17}$$

Where:
W_a = Work function
W_k = Kinetic energy of the particle
W_p = Potential energy of the particle

Photoelectric Emission

Photons that incident upon the cathode whose energies exceed the work function may eject electrons from the surface [4]. Work functions for aluminium range from 2.98 eV to 4.43 eV and copper from 4.07 to 4.7 eV [4]. Noting the emission spectra of the molecules in Tables 2.1 and 2.2 as well as the electromagnetic spectrum in Table 2.3, it is clear that the work function is within emitted photon range of excited molecules particularly the UV range.

2.2 Corona

2.2.1 Positive Corona

In the case of positive corona the electron avalanche is initiated by natural processes in the air, at the position where the ionisation constant is greater than zero (illustrated in Figure 2.12). The avalanche develops towards the

conductor in the increasing electric field. The highest field-intensified ionisation activity occurs near the conductor surface [14, 15].

Secondary ionisation occurs due to photoionisation or other natural methods. Clouds of space charge are formed by the various molecules in the gas, where negative ions are created away from the conductor as electrons are neutralised closer to the conductor. These space charge clouds modify the electric field and the discharge development leading to various modes of corona including Burst Corona, Onset Streamer, Positive Corona and Breakdown Streamer [14, 15].

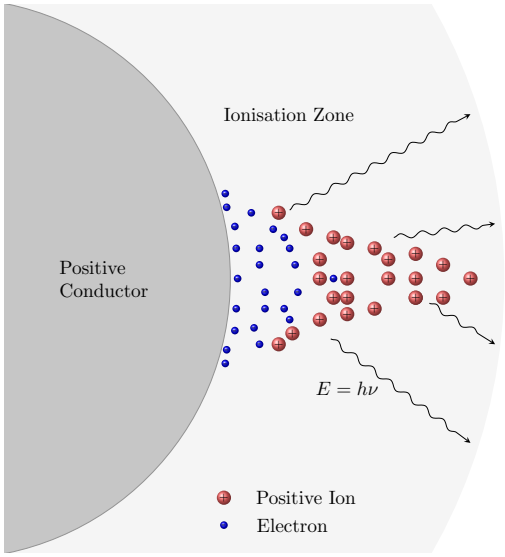

Figure 2.12: Positive Corona

Burst corona occurs at the onset of positive corona where electrons lose their energy due to ionisation activities before they get absorbed by the conductor. The discharge directs radially outwards from the electrode. Positive ion space charge cloud is formed around the conductor which suppresses the discharge. The spread of electrons then moves to another part of the conductor. As the ionisation spreads around the conductor and is suppressed by the space charge cloud a positive corona current pulse is produced [14, 15].

Onset streamers result from radial development of the discharge. A large amount of positive ion space charge is left behind by electron avalanches and this space charge cloud enhances the electric field away from the conductor, causing successive avalanches. The positive ion space charge cloud created from the avalanches reduces the electric field near the conductor surface and suppresses the streamer. When the space charge cloud is cleared, the original field is restored and the cycle repeats itself. The onset streamer is manifested as a faint blueish glow as illustrated in Figure 2.13, where the amplitudes of the pulses range from a few milliamps to a few hundred milliamps, and the repetition rate increases with the voltage up to a critical point where it is then suppressed by the negative charge and becomes positive glow. The pulses have larger amplitudes and occur less frequently than the Trichel Streamers. Positive onset streamers characteristically have a high pitched sound and are the main source of radio interference and audio noise on transmission lines [14, 15].

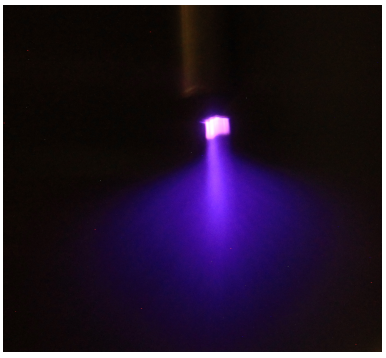

Figure 2.13: Onset Streamer

The shape of the measured corona pulse and the expected parameters are illustrated in Figure 2.14 and is represented by the double exponential equation [14].

$$i(t) = 2.335 i_p (e^{-0.01t} - e^{-0.0345t}) \tag{2.18}$$

Where:

t = time [ns]

i_p = peak current [mA]

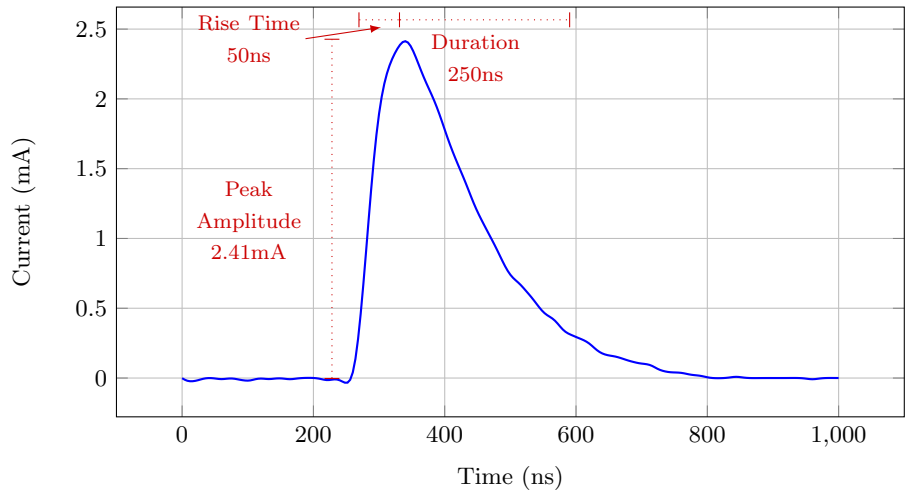

Figure 2.14: Onset Streamer Current Pulse

Positive glow corona is a stable glow without a pulsating nature and occurs under a particular condition of creation and removal of positive ions, where the field distribution allows for the rapid removal of positive ions while not allowing for the development of discharges and streamers. Glow corona manifests itself as a thin visible luminous layer over the conductor surface as illustrated in Figure 2.15, where the discharge current is a direct current with a small superimposed pulsating current with a high repetition rate [14, 15].

Positive breakdown streamers are characteristically similar to onset streamers

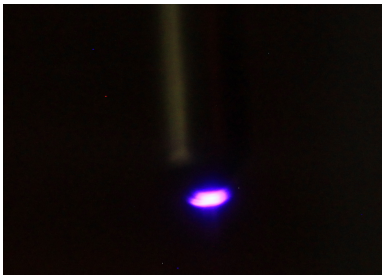

Figure 2.15: Positive Glow

but extend further into the gap and lead to breakdown of the gap. The streamer current and repetition rate are higher than onset streamers [14, 15].

2.2.2 Negative Corona

Negative corona occurs where a nonuniform electric field distribution exists in the gap, with the highest value at the conductor surface. At a high enough voltage the electric field at the surface of the conductor becomes sufficiently high to begin ionisation. Naturally created free electrons initiate electron avalanches, which progress to a position from the conductor where ionisation and attachment are equal. Beyond the boundary all electrons attach to form negative ions. The impact of the positive ions on the conductor and photoionisation produce the secondary ionisation that causes a self-sustaining discharge or corona [14].

Following the initial electron avalanche, two ion space charge clouds (illustrated in Figure 2.17) are formed from the positive and negative ions, moving towards the conductor and ground respectively. The space charge increase the electric field closer to the conductor and decreases the field away from the conductor, resulting in subsequent electron avalanches due to the higher field, but a shorter travelling distance for the avalanche [14].

Three modes of corona exist depending on how the electric field is modified, namely Trichel Pulses, Negative Glow and Negative Streamer. Each mode has distinct electrical, physical and visual manifestations [14].

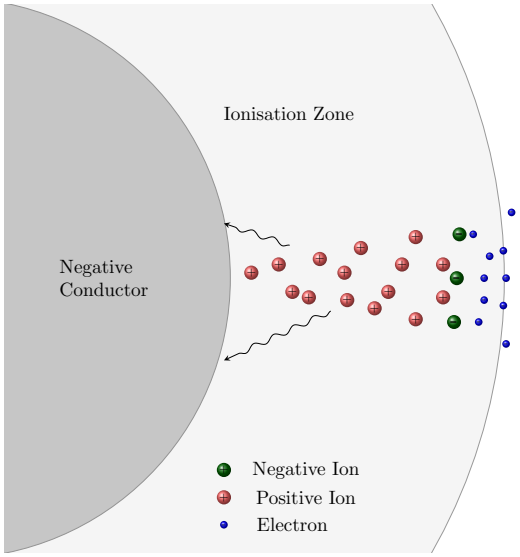

Figure 2.16: Negative Corona

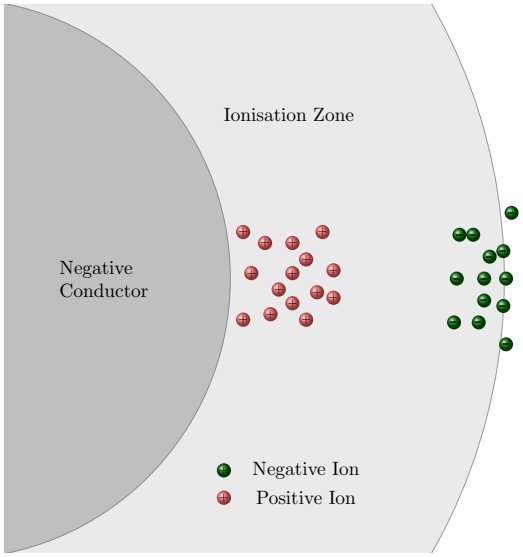

Figure 2.17: Negative Corona

Trichel Pulses occur slightly above the corona onset, where the positive space charge is absorbed and neutralised by the conductor leaving only the negative cloud. This decreases the electric field below the electron avalanche initiation

value. After the negative space charge cloud clears, the electric field reverts to its original state. The frequency of the Trichel pulses is dependent on the applied voltage [14, 16].

Lama and Gallo undertook a systematic study of Trichel pulses in needle to plane gaps, where they found that the time average corona current and the pulse frequency are linearly related, that the discharge is localised to a small volume around the tip and the Trichel pulse repetition rate is proportional to the mobility [17].

Measured Trichel pulses and parameters are illustrated in Figure 2.18, where it can be seen that the pulses have a consistent repetition rate. The pulse is represented by the double exponential equation [14].

$$i(t) = 1.3 i_p (e^{-0.019t} - e^{-0.285t}) \tag{2.19}$$

Where:
t = time [ns]
i_p = peak current [mA]

As the voltage is increased, the frequency of the Trichel Pulses reaches a critical value, where the pulses merge and become Negative Glow. This mode of corona is characterised by a bright spherical discharge and a steady corona current [14].

Negative Streamers occur over a certain range of voltage. In this mode the corona is characterised by a discharge current consisting of pulses superimposed on a constant DC component. Further increase in voltage leads to breakdown [14].

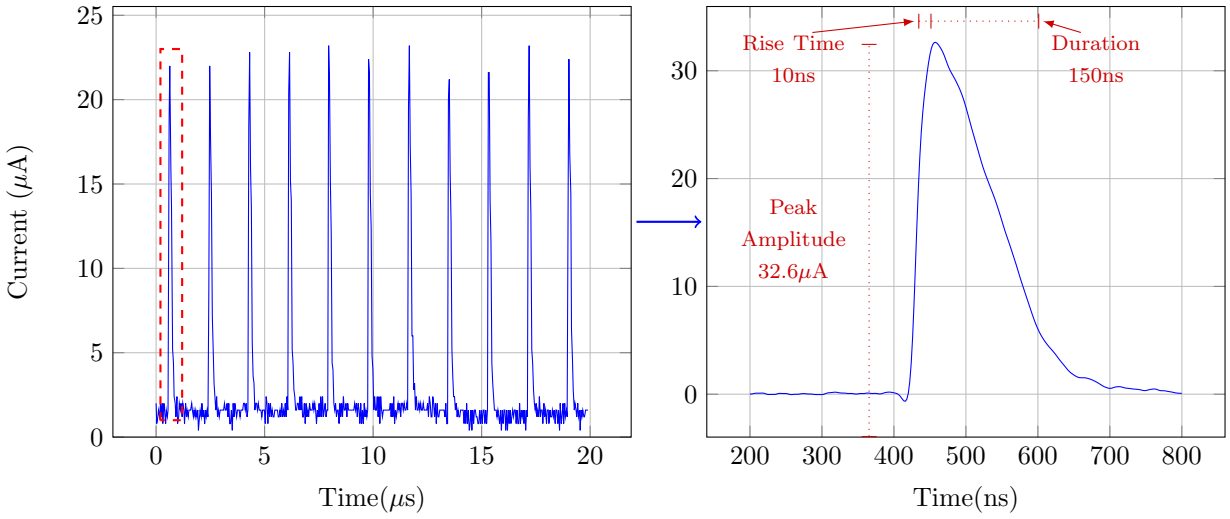

Figure 2.18: Trichel Pulses

2.3 Role of Singlet Oxygen

Singlet oxygen is the lowest excited state of molecular oxygen with the formulae of $O_2(a^1\Delta_g)$ [18]. The energy transition between the ground state Σ and $a^1\Delta_g$ is 0.97 eV or 1270 nm. The nature of singlet oxygen allows it to remain in the excited state for a relatively long period of time, where the radiative lifetime is approximately 45 minutes, but with the addition of quenching, a state will survive for 100 ms [1, 2, 18].

Molecular oxygen has the following single molecule transitions [19]:

$$O_2(^3\Sigma) \rightarrow O_2(a^1\Delta_g) \text{ @ } 1269 \text{ nm}$$

and the following simultaneous transitions [19]:

$$\begin{aligned} 2 \times O_2(^3\Sigma) &\rightarrow 2 \times O_2(a^1\Delta_g) \text{ @ } 634 \text{ nm} \\ 2 \times O_2(^3\Sigma) &\rightarrow O_2^1\Sigma + O_2(a^1\Delta_g) \text{ @ } 476 \text{ nm} \end{aligned}$$

The emission of photons due to singlet oxygen collisions occur when:

$$O_2 + O_2(a^1\Delta_g) = 2O_2 + h\nu_{(1270nm)}$$

$$O_2(a^1\Delta_g) + O_2(a^1\Delta_g) = 2O_2 + h\nu_{(634nm)}$$

The emission at 1270 nm is important as there are no other photon emissions near this in oxygen or nitrogen, and it should be possible to isolate singlet oxygen by measuring this wavelength.

2.3.1 Role in Detachment

In a gas discharge in air a significant number of excited nitrogen and oxygen molecules are produced, most of which will return to their ground state almost immediately upon emission of a photon; singlet oxygen does not and as such is thought to contribute in some manner to the process of a gas discharge. Kearns summarises that the concentrations of metastable oxygen molecules are up to 10% of the oxygen in the gas discharge and are shown to survive outside of the discharge [18]. Lowke proposed in his work that the singlet oxygen has a dominant role in the pre-breakdown corona and streamer process because of its ability to detach electrons from negative ions [1, 2].

$$O_2^- + O_2(a^1\Delta_g) = 2O_2 + e$$

Morrow included singlet oxygen in his modelling and simulations and deemed that the role of the metastable oxygen is a crucial component for the theory of positive glow [3]. This includes the effect of electron detachment from negative ions.

The rate coefficients used by Lowke are [1, 2]:

2×10^{-10} cm^3.s^{-1}	$O_2^- + O_2(a^1\Delta_g) \rightarrow 2O_2 + e$	metastable detachment
2.2×10^{-18} cm^3.s^{-1}	$O_2 + O_2(a^1\Delta_g) \rightarrow 2O_2$	metastable quenching

Fehsenfeld et al made use of a PbS photometer to determine the associative and collisional electron detachment reaction rate constants of singlet oxygen [20], which are also presented as recommended rates by Phelps [21].

3×10^{-10} cm^3.s^{-1}	$O^- + O_2(a^1\Delta_g)$	associative detachment
2×10^{-10} cm^3.s^{-1}	$O_2^- + O_2(a^1\Delta_g)$	collisional detachment

Belostotsky et al investigated the negative ion destruction by oxygen atoms and singlet oxygen molecules in a plasma through time resolved actinometry and IR spectroscopy and found the following detachment rate [22].

$1.9 \pm 0.4 \times 10^{-10}$ cm^3.s^{-1}	$O^- + O_2(a^1\Delta_g)$

As the reaction rate for singlet oxygen in the neutral is approximately 2×10^{-18} cm^3.s^{-1}.

Gudmunsson and Franklin presented the role of recombination and detachment in discharges [23, 24]. Franklin reported that the half life is longer at 64 min [24].

Gudmunsson reviewed which of the reactions is dominant under certain conditions. The rates proposed by Gudmunsson are listed as follows [23, 25]:

1.3×10^{-10} cm^3.s^{-1}	$O^- + O_2(a^1\Delta_g) \rightarrow products$	collisional detachment
3.3×10^{-11} cm^3.s^{-1}	$O^- + O_2(a^1\Delta_g) \rightarrow O_3 + e$	collisional detachment
2×10^{-10} cm^3.s^{-1}	$O_2^- + O_2(a^1\Delta_g) \rightarrow 2O_2 + e$	collisional detachment

2.3.2 Role in Photoionisation

In addition to the role singlet oxygen is expected to play in electron detachment from negative ions, it is known that as singlet oxygen has an energy (0.97 eV) and a relatively long lifespan, a number of authors have stated that

singlet oxygen will play a role in photoionisation [26].

$$O_2(a^1\Delta_g, \nu = 0) + h\nu = O_2^+(X^2II_g) + e$$

Clark and Wayne have stated that the photoionisation of singlet oxygen at wavelengths above 103 nm are important in atmospheric chemistry and that solar radiation becomes important to this ionisation process [27]. They measured the absolute cross sections of singlet oxygen and suggested that there is a distinct difference between cross sections for singlet and ground state (allow a transition to ionised state) [27]. Subsequently Ogawa and Ogawa found that the the singlet cross sections are larger below 129 nm apart from specific wavelengths for the ground state [28].

In a gas discharge where sufficient singlet oxygen is produced, where ground state oxygen is ionised by emitted photons at 102.66 nm, singlet oxygen may additionally have a greater role in ionisation than previously understood. It would be difficult to isolate this, however detection of singlet oxygen from a corona discharge is the first step.

Chapter 3

Modelling of Gas Discharges and Corona

A 1.5 dimensional model, where the transport equations are modelled in one dimension and the electric field in two dimensions, is presented in this chapter. The chapter presents the implemented model that uses the flux corrected transport algorithm and the chapter offers a short critique on the particle method. The objective of the model is to implement the theory presenting in Chapter 2 to understand the gas discharge and corona process under the conditions of applied voltages. The model investigates the corona process including the role of the space charge and to support the hypothesis in determining the presence and role of singlet oxygen. The model attempts to illustrate the long term processes and role that may influence the corona including the role that the reaction of oxygen and negative ions and negative ions and singlet oxygen may play in releasing secondary electrons.

3.1 Particle Model of a Gas Discharge

The particle mesh method represents numerous physical particles as a super particle, where these super particles have the same charge to mass ratio as

the physical particles which allows the super particles to be moved by the Lorentz Force and follow the Newtonian equations of motion [29, 30].

$$\vec{F} = q(\vec{E} + \vec{v} \times \vec{B}) \tag{3.1}$$

Where:
$\vec{F}$ = Force exerted on the particle [N]
q = Charge of particle [C]
$\vec{E}$ = Electric field [V.m^{-1}]
$\vec{v}$ = Velocity of particle [m.s^{-1}]
$\vec{B}$ = Magnetic field [T]

The super particles have a finite size, charge and mass and are interpolated to a computational spacial grid to solve for the electric field through Poisson's equation. The particle mesh method has been applied to a number of gas discharge solutions [31, 32, 33, 34, 35].

Because of this cloud nature of the super particles, the short-range particle-particle interactions are smoothed and the development of a suitable collision model is necessary to account for these particle-particle interactions, which take place within distances shorter that the grid width. The focus of a number of works is the Monte Carlo Collision (MCC) code for the particle mesh technique, where the MCC codes are probabilistic in nature, related directly to the collisional cross sections of a particle for an electron energy level and described by the equation [29, 35, 36].

$$P = 1 - exp(-\Delta x_i \sigma_T(\epsilon_i) n_t(\vec{x}_i)) \tag{3.2}$$

Where:
Δx_i = Displacement over time Δt [cm]
$\sigma_T(\epsilon_i)$ = Collisional cross-section of collision type T for energy ϵ_i [cm^2]
$n_t(\vec{x}_i)$ = Number density of incident particle species [cm^{-3}]

The theory of the collisional model is consistent with the understanding of fluid dynamics in a gas, however the implementation of the MCC has proven difficult. The model is implemented by comparing the probability above to a random number, on the basis that if there enough particles and collisions the correct weighting of type of collision should be produced. The author found that this did not occur [30] when implemented and it was thought that it was due to the dependence on the time step. The above model is based on the displacement of the particle (Δx) during a time step and the collisional cross-section (σ_T) of the particle related to the energy of that particle. The average kinetic energy is a good indicator of bias; and the total collisional probability is biased towards that average kinetic energy [30].

- If the time step is too small, the electrons in the model suffer from a lack of average kinetic energy and the probabilities of collision are biased towards the lower range of collisions including momentum, excitation and attachment. Although this should be accounted for by the momentum collision or null collision, which has minimal or no kinetic energy loss, and the electrons should gain enough energy to ionise, the implementation has not proven successful.

- If the time step is too large, the electrons in the model suffer from a gain of average kinetic energy that is too high and unrealistic and biased towards the higher range of collisions including ionisation. A higher average kinetic energy also means that electrons move out of bounds before having a chance to ionise any other particles.

There were a number of additional shortcomings that limit its use for corona modelling including the time steps, the particle size, the grid width for accuracy, stability and efficiency [29].

- Larger time steps lead to a more computational efficient model, however particles moving out of the boundary space rendering the model invalid.
- Due to its discrete nature, the number of particles must be sufficient to overcome graininess, which leads to a limitation of simulation time. Whilst this may be ok for the initial discharge development, the simulation is required to look at the effects of space charge after the initial discharge development.
- Discrete particles may exaggerate fluctuations and oscillations.
- Round-off and truncation errors lead to errors growing in time and an unstable code.

3.2 Fluid Model of a Gas Discharge

The fluid model of a gas discharge counters the shortcomings of the particle model, however does not take into account the probabilistic nature of the electron collisions in the plasma. Instead coefficients that have been measured or derived through the Boltzmann equation are used, meaning that the model will be averaged and at some point may not give the required results, for example, if the modelled electric field reaches 0 $kV.cm^{-1}$, drift does not occur and the fluids stagnate. It is, however, still the most appropriate, versatile and successful method which has been used to model gas discharges in uniform and non-uniform fields, for corona, for surface discharges and in modelling the development of lightning streamers.

Morrow et al proposed the use of the flux corrected transport algorithm (initially described by Boris and Book) as a numerical solution to the flow of charged particles in a gaseous system [13, 37, 38, 39, 40]. Morrow and Lowke applied the algorithm to the modelling of a streamer [13]. The work has

provided a basis for extensive modelling use.

Shim et al further built on the FDM FCT methods for a two dimensional analysis of needle plane corona [41].

The finite difference schemes used in FCT however limit the shape of the grid, limit the type of complex geometries expected in discharges and can be computationally expensive. Georghiou et al proposed an improved finite element FCT method [42] and continued to implement it for various cases including the modelling of the gas discharge in two dimensions and investigating the role of photoionisation [43, 44].

Sattari et al have developed finite element methods to investigate Trichel pulses [45]. Importantly Sattari has modelled the repetition rate and the role of space charge in Trichel pulses.

Recently Deng et al have modelled the Trichel pulse under air flow conditions in two dimensions and successfully illustrated the influence the air flow by showing that there was a decrease in repetition rate of Trichel pulses for 18 $m.s^{-1}$ [46].

The commercial package COMSOL Multiphysics® has become more popular in solving the drift diffusion equations and has been applied to gas discharges. Kim et al have investigated the breakdown voltage in air using COMSOL Multiphysics® [47]. Tran et al have investigated negative discharges in air with and without a dielectric barrier. The use of the fluid equations through COMSOL Multiphysics® in investigating surface charges on a dielectric barrier found good correlation with experiments [48].

Recently Zhuang and Zeng have developed a local discontinuous Galerkin method that combines the advantages of finite volume and finite element stating that it is a compact, local conservative and high order accurate method [49].

The FCT methods extend further into other research areas. Liu and Pasko, for example, have used similar algorithms to model positive and negative streamers that originate from quasi-static electric fields developed during lightning activity [50].

Whilst the authors have concentrated on negative corona and Trichel pulse, apart from the work done on positive glow by Morrow [3, 13], positive corona in the modes of onset and breakdown streamers has an unnoticeable presence in literature, possibly due to the unknown mechanisms that lead to initiation and possibly due to the space charge and electric field calculations for the discharge model.

Whilst a more complex solution could be developed, the purpose of the thesis is to illustrate and understand certain physical phenomena using the information from the solution of the Boltzmann equation and as such the 1.5D FDM model is considered sufficient.

3.2.1 Algorithm

The gas discharge algorithm is illustrated in Figure 3.1, where the electrons, and the positive and negative ions are each considered a fluid. The algorithm begins with an initial plasma consisting of electrons, and positive and negative ions, such that the quasi-neutrality of a plasma is preserved. Following this the routine begins with the application of the voltage on the anode for positive gas discharge and cathode for the negative gas discharge, from the applied voltage the Laplacian electric field is found, the space charge determines the Poissonian electric field and from the addition of the two, the transport and Townsend coefficients, pre-determined through Bolsig, are read. The algorithm is now ready to transport the fluids through the application of the drift-diffusion equations, which also includes the addition of sources and sinks. Following the transport of the fluids, the external circuit current is determined, and subsequently taken into account as a voltage drop

in the next iteration of the algorithm.

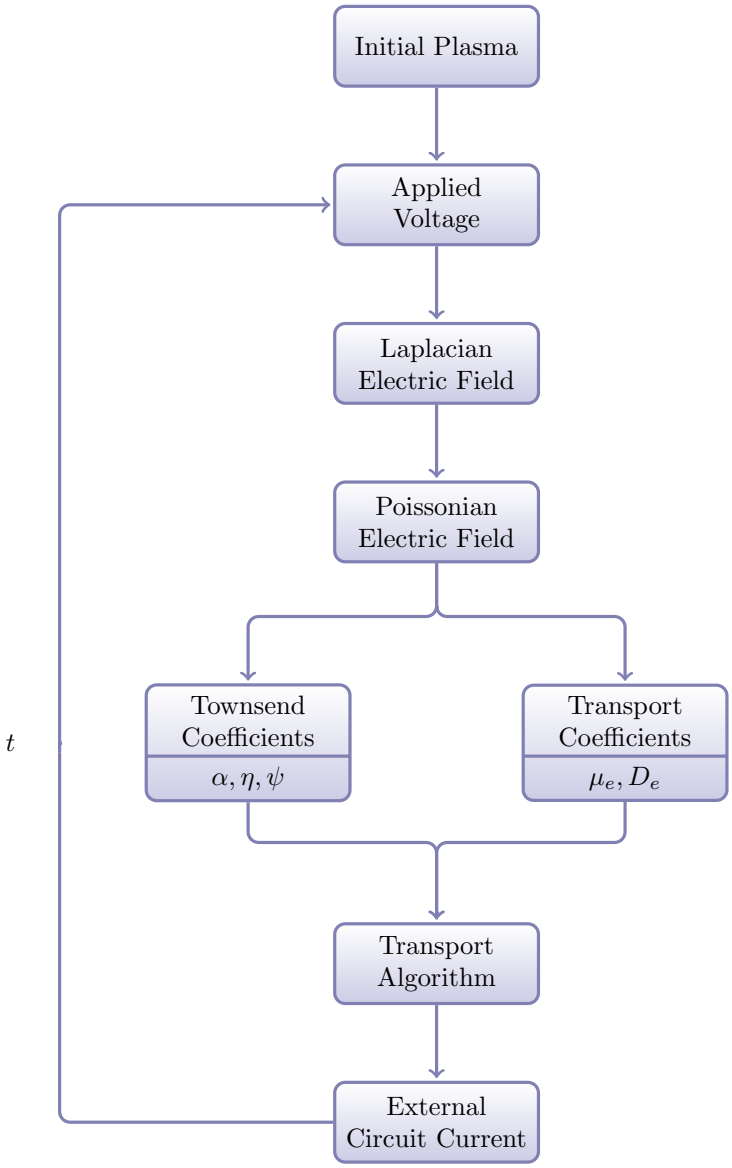

Figure 3.1: Solution Flowchart

3.2.2 Drift-Diffusion Equations

The continuity equations written for electrons, negative and positive ions in one dimension are given by:

$$\frac{\partial N_e}{\partial t} = S + N_e\alpha|\vec{v}_e| - N_e\eta|\vec{v}_e| - N_eN_p\beta - \frac{\partial(N_e\vec{v}_e)}{\partial z} + \frac{\partial}{\partial z}\left(D_e\frac{\partial^2 N_e}{\partial z^2}\right) \quad (3.3)$$

$$\frac{\partial N_p}{\partial t} = S + N_e\alpha|\vec{v}_e| - N_eN_p\beta - N_nN_p\beta - \frac{\partial(N_p\vec{v}_p)}{\partial z} + \frac{\partial}{\partial z}\left(D_p\frac{\partial^2 N_p}{\partial z^2}\right) \quad (3.4)$$

$$\frac{\partial N_n}{\partial t} = N_e\eta|\vec{v}_e| - N_nN_p\beta - N_nN_ok_d - \frac{\partial(N_n\vec{v}_n)}{\partial z} + \frac{\partial}{\partial z}\left(D_n\frac{\partial^2 N_n}{\partial z^2}\right) \quad (3.5)$$

$$\frac{\partial N_o}{\partial t} = N_e\psi|\vec{v}_e| - N_nN_ok_d - N_oN_{O_2}k_q \quad (3.6)$$

Where:

$N_{e/p/n/o}$ = Number densities of electrons, positive ions, negative ions and singlet oxygen [cm^{-3}]

N_{O_2} = Number density of oxygen [cm^{-3}]

$\vec{v}_{e/p/n}$ = Velocities of electrons, negative ions and positive ions [cm.s^{-1}]

α = Ionisation coefficient [cm^{-1}]

η = Attachment coefficient [cm^{-1}]

ψ = Singlet oxygen coefficient [cm^{-1}]

S = Photoionisation term [$\text{cm}^{-3}.\text{s}^{-1}$]

β = Recombination coefficient [$\text{cm}^{3}.\text{s}^{-1}$]

$D_{e/p/n}$ = Diffusion coefficient [$\text{cm}^{2}.\text{s}^{-1}$]

3.2.3 Townsend Coefficients

The collision Townsend coefficients are calculated from the numerical Boltzmann equation solver Bolsig for electrons in weakly ionised gases in uniform fields [12].

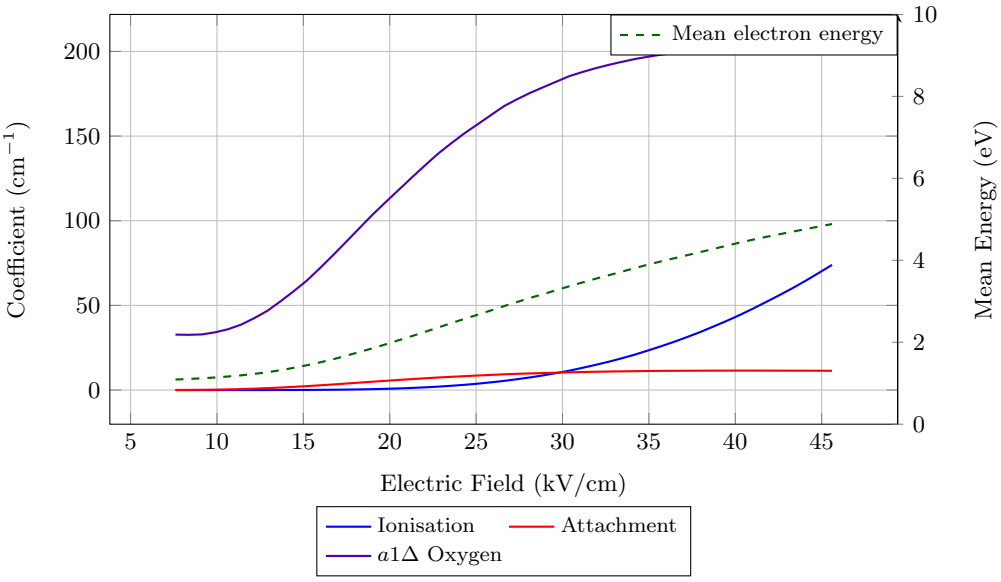

Figure 3.2: Townsend Coefficients and Mean Electron Energy for Air

The coefficients for ionisation, attachment and for singlet oxygen excitation are considered the most important and are shown in Figure 3.2 together with the mean energy of the electron. It is evident that singlet oxygen excitation has a higher coefficient than the ionisation or attachment across the given electric field. It is shown that as the mean energy increases, that the ionisation and attachment coefficients increase and the singlet oxygen decreases. These are important aspects in the investigation of the role of singlet oxygen.

3.2.4 Photoionisation

A model of photoionisation was developed by Penny and Hummert, where they related the number of photo-electrons produced to the number of ionisation events [51]. They showed that the photoionisation events are dependent on the pressure and distance from the discharge with a function given by [51].

$$\phi = \frac{N_P}{N_D}\theta PD \tag{3.7}$$

Where:

N_D = Number of ion pairs produced per second
N_P = Number of photon pairs produced per second
PD = Pressure distance relationship [cm torr]
θ = Angle subtended by volume

The physical model for photoionisation was developed by Zheleznyak et al [52] partially based on the data, where the model was based on the assumption that excited nitrogen atoms will emit radiation which is absorbed by oxygen and leads to photoionisation. The ultraviolet radiation effect of nitrogen molecules is in the wavelength range of 98 - 102.5 nm where the ionisation threshold for oxygen is 102.4 nm. The rate of photoionisation is dependent on the absorption of the emission and as such the partial pressure of oxygen [44, 52, 53]. Kulikovsky implemented a photoionisation model based on the the Zheleznyak model, where the number of photoionisation events (electron-ion pairs produced per second) in incremental volume dV_1 due to ionisation events in volume dV_2 is given by [53]:

$$S_{photo}(dV_1, dV_2) \simeq \frac{I(dV_2)f(r)}{4\pi r^2}dV_2 \tag{3.8}$$

$$I(dV_2) = \xi\frac{P_q}{P + P_q}\alpha N_e\frac{dx}{dt} \tag{3.9}$$

$$f(r) = \frac{\exp\left(-\chi_{min} P_{O_2} r\right) - \exp\left(-\chi_{max} P_{O_2} r\right)}{r \log(\chi_{max}/\chi_{min})} \tag{3.10}$$

Where:

r = distance between volumes dV_1 and dV_2

P = Pressure [760 torr]

P_q = Quenching pressure [30 torr]

P_{O_2} = Partial pressure of oxygen [22%P]

$\chi_{max,min}$ = Max and min absorption coefficients of oxygen [cm^{-1}.torr^{-1}]

Pancheshnyi et al investigated the role of background ionisation and indicate that this background ionisation can be neglected when the photoionisation is included [54].

3.2.5 Electric Field

The electric field is solved through Poisson's equation, which is derived from Gauss' law and describes the potential at a point [5, 55, 56]:

$$\nabla^2 \phi = -\frac{\rho}{\epsilon_0} \tag{3.11}$$

Where:

ϕ = Space potential [V]

ρ = Space charge [C.m^{-3}]

ϵ_0 = Permittivity of free space

Poisson's equation can be rewritten as:

$$\nabla^2\phi = -\frac{q_e}{\epsilon_0}(-N_p + N_n + N_e) \tag{3.12}$$

Where:

q_e = Charge of electron [C]
N_p = Number density of positive ions [m^{-3}]
N_n = Number density of negative ions [m^{-3}]
N_e = Number density of electrons [m^{-3}]

Poisson's equation is solved with $\rho = 0$ using the finite difference methods in Appendix A giving the Laplacian electric field E_L.

Davies stated that the using a uniform or cylindrical form of Poisson's equation overestimates the influence of the space charge on the electric field, as the discharge is only limited to a channel. A solution using disc's of space charge is that takes account of the radius of the channel, r, is proposed where the axial field at point along the axis is given by [40, 57, 58]:

$$E(x) = \frac{1}{2\varepsilon_0}\int_{-x}^{0}\rho(x+x')\left[-1 - \frac{x'}{\sqrt{x'^2 + r^2}}\right]dx' + \int_{0}^{d-x}\rho(x+x')\left[1 - \frac{x'}{\sqrt{x'^2 + r^2}}\right]dx' \tag{3.13}$$

Image charges placed outside of the boundaries are used to correctly model the electric field [57, 58].

The total field is then the addition of the Laplacian electric field due to the voltage difference of the electrodes and the Poissonian (or Space Charge) electric field due to the space charge between the electrodes:

$$E = E_L + E_P \tag{3.14}$$

3.2.6 External Circuit Current

Referring to the system bounded by a path S illustrated in Figure 3.3, Gauss' Law for the system is given by [59]:

$$\oint_S \vec{E}.ds = \int_V \frac{\rho}{\varepsilon} dV + \frac{\sigma_+ A_+ + \sigma_- A_-}{\varepsilon} = 0 \tag{3.15}$$

Where:

$\vec{E}$ = Electric field [v.m^{-1}]
V = Volume [cm^3]
ρ = Space charge [C.cm^{-3}]
ε = Permittivity
σ_+ = Surface charge of anode [C.m^{-2}]
σ_- = Surface charge of cathode [C.m^{-2}]
A_+ = Area of anode [m^2]
A_- = Area of cathode [m^2]

Considering the moving charge $+q$, the current induced in the external circuit will be related to the change in surface potential of the electrodes which is equal to that movement of charge $+q$ [59].

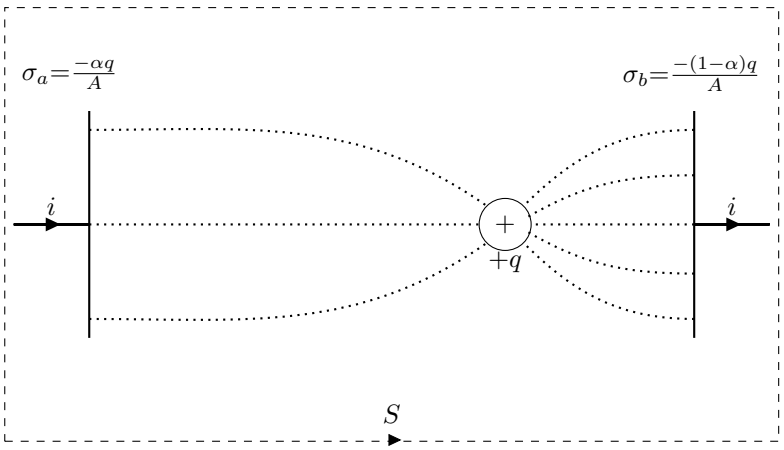

Figure 3.3: Gauss Law and External Circuit Currents

Sato applied this concept to the movement of space charge in gas discharges and Morrow subsequently completed it to the form given by [60, 61]:

$$I(t) = \pi r^2 \frac{q_e}{V_A} \int_0^d (N_p v_p - N_n v_n - N_e v_e + \frac{\partial^2 D N_e}{\partial^2 x}) E_L dx \tag{3.16}$$

This form is however incomplete when trying to relate it to the circuit as this current will affect the voltage applied to the circuit [62]. In a simplified arrangement, a series resistor and capacitor would give a voltage drop which is applied iteratively to the applied voltage.

$$V_A = I(t)R - \frac{1}{C} \int I(t) dt \tag{3.17}$$

A far more complex solution including inductance, additional coupling capacitors and resistors is completed in Appendix B.

3.2.7 Boundary Conditions

The following boundary conditions are applicable and implemented in the model. The boundary conditions indicate that the ions are absorbed and the electrons are released where applicable.

Table 3.1: Boundary Conditions for the Model

Type	Boundary	Value
Convective and diffusive N_p	Anode/Cathode	0
Convective and diffusive N_n	Anode/Cathode	0
Convective and diffusive N_e	Anode	0
Convective and diffusive N_e	Cathode	$\gamma \frac{v_p N_p}{v_e}$
Outer Boundary ϕ_d	Anode/Cathode	0
Inner Boundary ϕ_0	Anode/Cathode	V_a

3.2.8 Accuracy, Stability and Noise

Courant-Friedrichs-Lewy and von Neuman conditions are required to be fulfilled when solving an explicit algorithm and are respectively given by [13]:

$$\Delta t < \frac{\Delta x}{v_e} \tag{3.18}$$

$$\Delta t \leq \frac{\Delta x^2}{2D} \tag{3.19}$$

Although more applicable in particle simulations; the Debye length, λ_D, is taken into account as it is a phenomena related to the plasma itself [63]. In particle simulations it is shown that the most appropriate value occurs when [63]:

$$\Delta x < \pi \lambda_D \tag{3.20}$$

3.3 Results

3.3.1 Negative Corona

The parameters used in the model are listed in Table 3.2, where a uniform grid is used. The grid spacing has to be fine close to the electrode for the solution to be meaningful and this comes at the expense of a shorter time step.

Table 3.2: Input Parameters for Negative Corona Model

Parameter	Symbol	Value
Pressure	P	760 torr
Temperature	T	20 °C
Cathode radius	r	0.02 cm
Electrode spacing	d	2.5 cm
Grid size	N_g	800
Grid spacing	dx	0.03 cm
Time step	dt	1×10^{-12}
Secondary ionisation coefficient	γ	0.01
Recombination coefficient	β	2×10^{-7}
Ion-singlet detachment coefficient	k_d	2×10^{-10}
Singlet quenching coefficient	k_q	2×10^{-18}
Mobility of positive ion	μ_p	2.34 $cm^2.V^{-1}.s^{-1}$
Mobility of negative ion	μ_n	2.7 $cm^2.V^{-1}.s^{-1}$
Diffusion of positive ion	D_p	$5{\times}10^{-2}$ $cm^2.s^{-1}$
Diffusion of negative ion	D_n	$5{\times}10^{-2}$ $cm^2.s^{-1}$
Applied voltage	V_a	-8 kV

An initial plasma number density is applied to the system, which gives a peak electron and positive ion density of 0.9995 cm^{-3} at 0.02 cm.

$$N_i = \exp(-(x + dx)^2) \tag{3.21}$$

Initial Corona Pulse

The initial Trichel pulse is illustrated in Figure 3.4 with the development of the space charge and its modification of the electric field between 0 and 40 ns illustrated in Figures 3.5 and 3.6 for the 1.5 cm of the gap closest to the electrode. The *Laplacian Field* refers to the electric field determined only by the voltage between the electrodes and the *Space Charge Field* refers to the electric field determined only by the space charge. The space charge developed and its influence on the electric field are critical for the mechanism of corona. The point where ionisation is equal to attachment is additionally illustrated in Figure 3.6.

As is shown at 10 ns the current is still negligible, but the space charge is continuing to build, with an electron density peak of 450 cm^{-3}, which is too small to influence the electric field. After 25 ns the exponential growth of the space charge is evident as the current maintains an increasing trend and there is a peak electron density of 6×10^8 cm^{-3}, which is enough to start influencing the electric field. It is noticeable that the densities of the positive ions are dominant closer to the cathode and the negative ions are dominant away from the electrode. It is also noticeable that all species continue to build rapidly. After 35 ns the electric field has collapsed, the current begins decreasing as the electrons start drifting away from the electrode at a lower velocity. The influence of the positive ions on the current becomes evident as the density is high at the electrode, where the electric field and drift velocities are the highest. The influence of the negative ions on the current is minimal, as the negative ions move slowly away from the electrode into a lower electric field. The movement of the positive and negative ions is far less than the electrons after 40 ns, as the mobility of these ions is far less than that of the electrons and the electric field has collapsed causing stagnation (i.e. the only movement possible is diffusion). This is thought to be a limitation of the 1.5D finite difference model over a full 2D finite element model.

Trichel postulated a similar theory to that illustrated, where the enhance-

ment of the field close to the electrode and the collapse of the field away from the electrode leads to the shape Trichel pulse [16].

The continual development of the space charge and modification of the electric field between 40 and 200 ns is illustrated in Figures 3.7 and 3.8. The point where ionisation is equal to attachment is additionally illustrated in Figure 3.8. The electron movement is diffusion dominated at this stage as the field has collapsed. The movement and recombination of positive and negative ions start allowing for the field to recover. The generation of singlet oxygen due to the moving electrons is particularly evident and expected as the collisional cross-section and the Townsend coefficient have a high value across a range of electron energies.

The external circuit current, number densities and collapsing electric field are similar to the modelling results produced by Morrow and Tran [40, 48], with obvious differences in magnitude due to different configurations and differences in the shape due to the implementation of the code. Importantly the Trichel pulse has similar shape to that expected and measured in Figure 2.18.

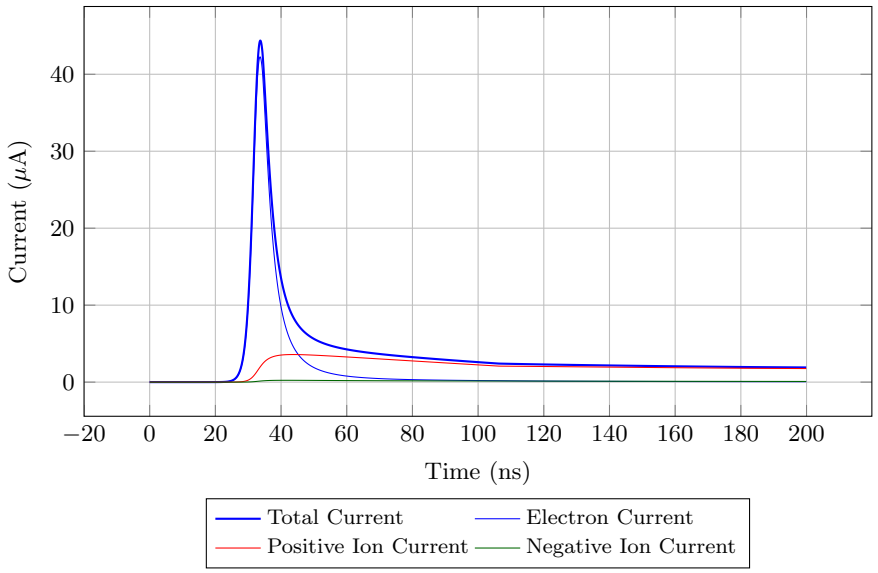

Figure 3.4: Initial Trichel Pulse

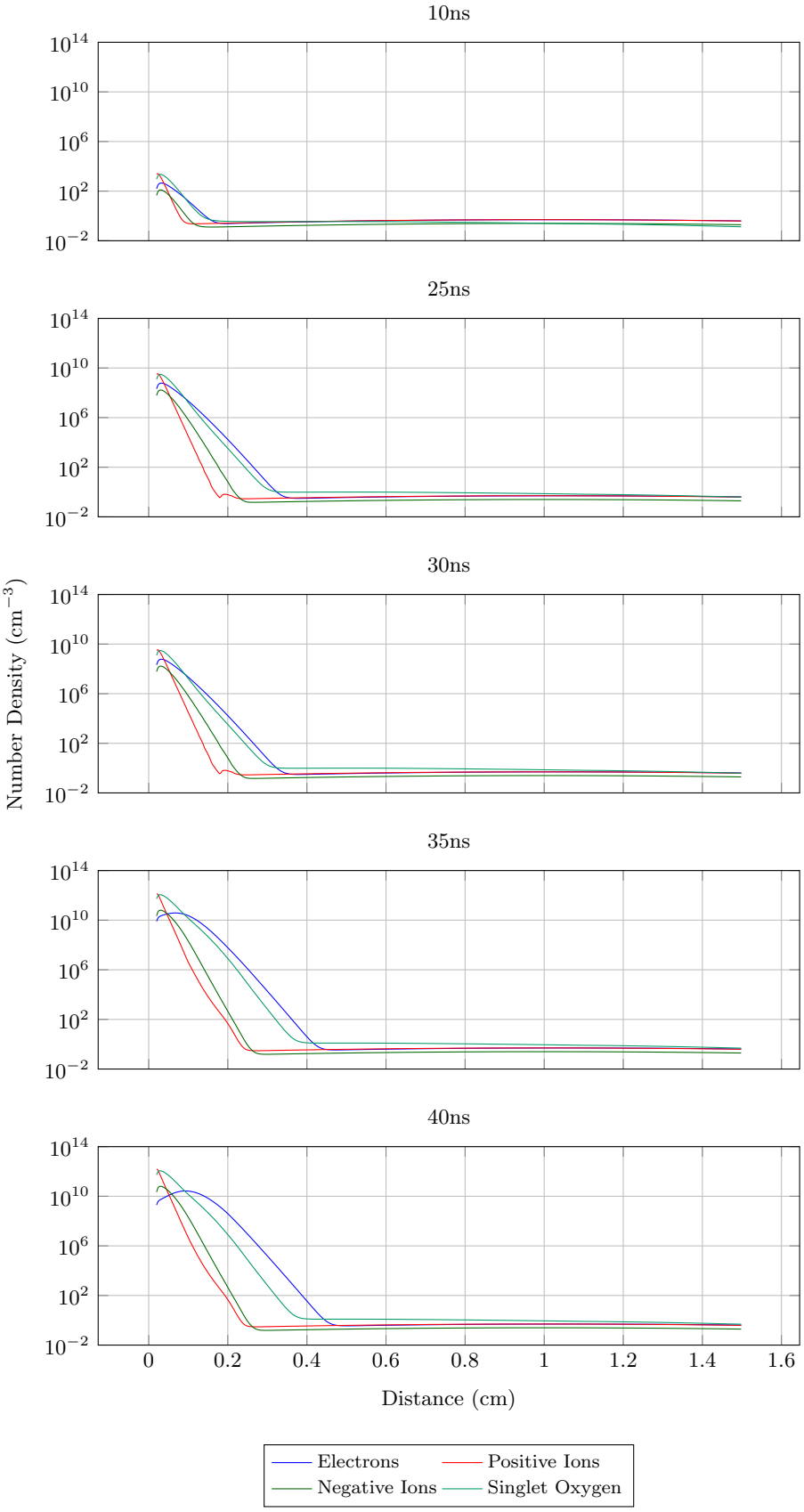

Figure 3.5: Development of Space Charge during Trichel pulse

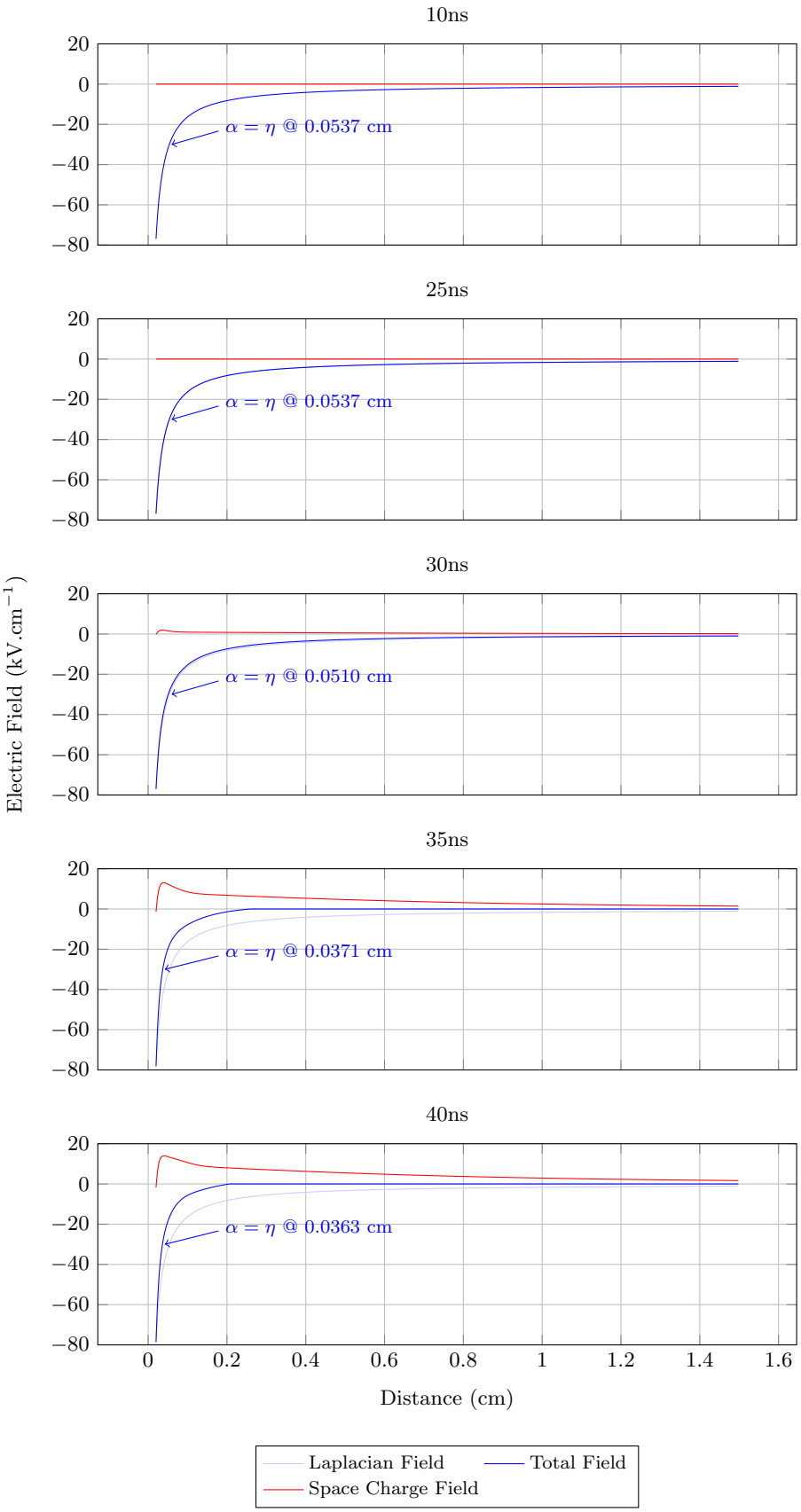

Figure 3.6: Development of Electric Field during Trichel pulse

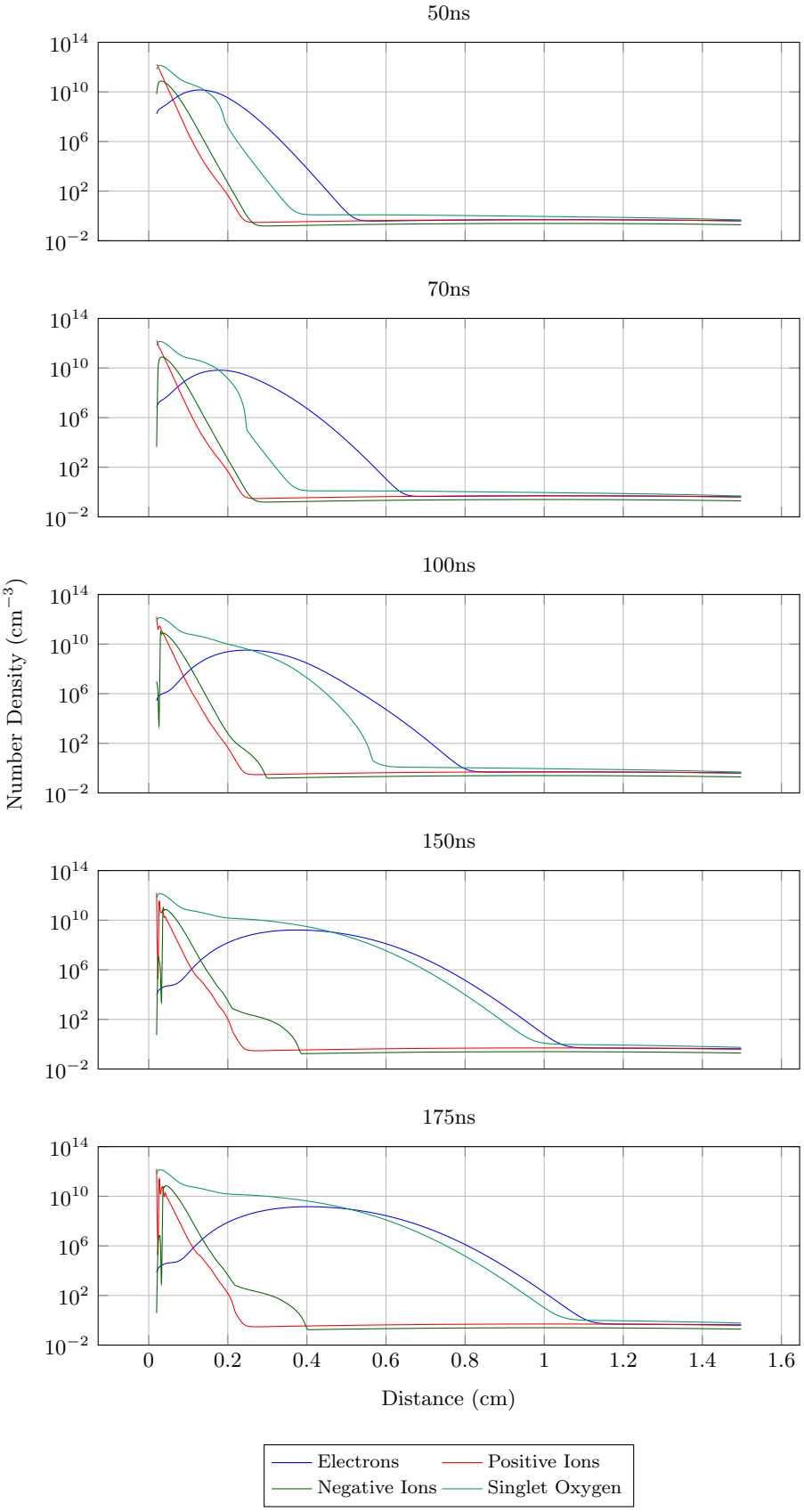

Figure 3.7: Development of Space Charge during Trichel pulse

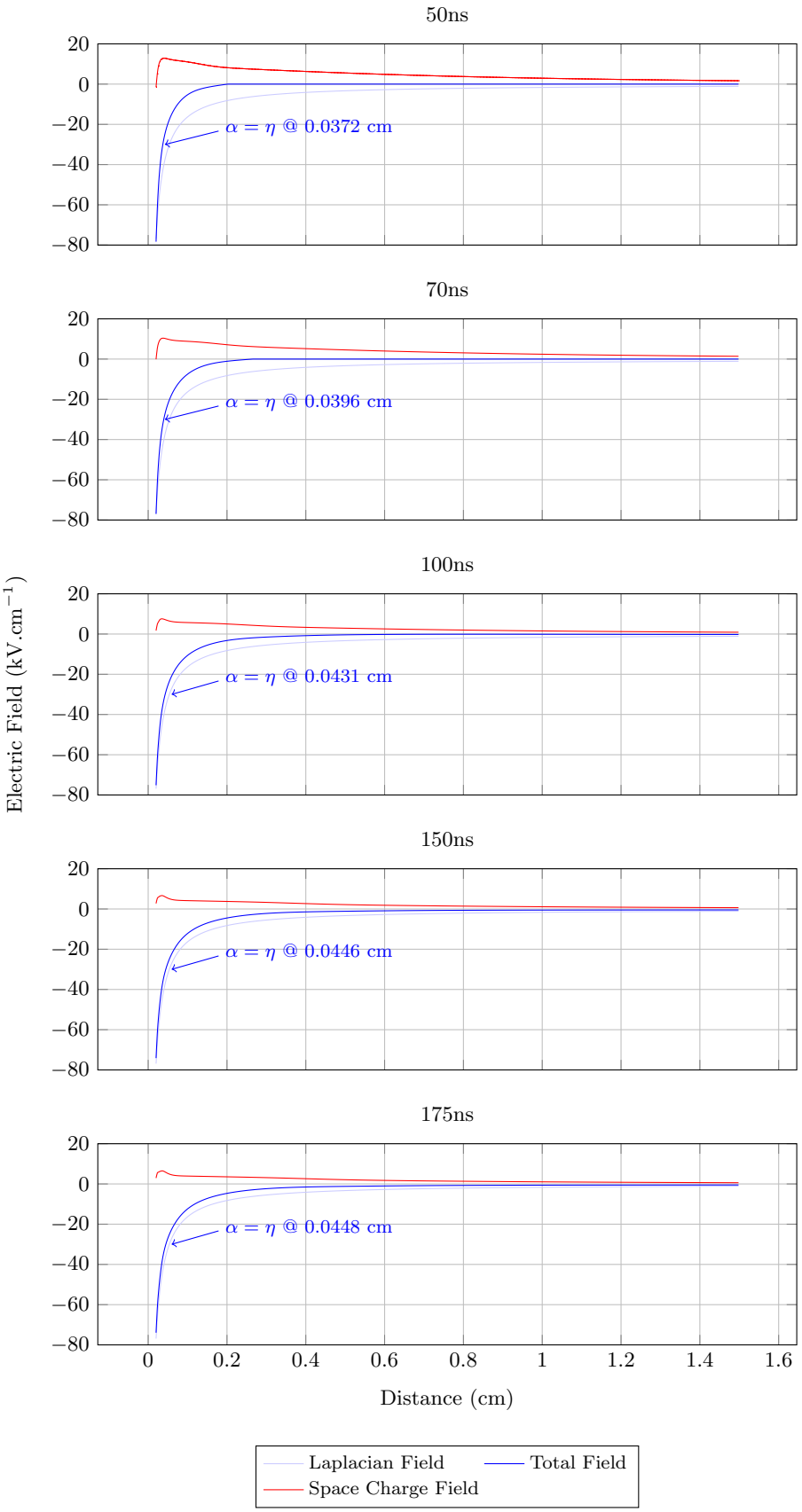

Figure 3.8: Development of Electric Field during Trichel pulse

After Initial Corona Pulse

External circuit current up to 2200 ns is illustrated in Figure 3.9 with the development of the space charge and the recovery of the electric field over this period illustrated in Figures 3.10 and 3.11. The critical electric field where ionisation is equal to attachment is additionally illustrated in Figure 3.11. The space charge up to 6200 ns is shown in Figure 3.12.

The positive ion current continues to decay from previously until a second Trichel pulse occurs at around 1588 ns, the pulse has a smaller peak at 2.6 μA than the original pulse but follows a similar pattern. The reason for the smaller pulse is due to the presence of positive and negative ion densities in the system, which cause the electric field to collapse at a smaller value.

It is shown that the positive ions maintain a peak near the cathode and the negative ions have moved away from the cathode. Again the complete stagnation of the ions due to the collapsed electric field is considered a limitation of the model.

The oscillations at A were initially thought to be a numerical instability related to the recombination of positive and negative ions, however over time these oscillations become smaller, until they reappear after the second Trichel pulse, as shown in Figures 3.10 and 3.12. It is thought that they are related the release of secondary electrons and or due to the the diffusion of the electrons.

It is clear that the electrons continue to diffuse across the gap, this is both of interest and a source of confusion, it is expected that electrons should attach and form negative ions closer to the cathode; however, considering the attachment cross-sections in Figure 2.6 and the coefficients in Figure 3.2, the electron energy range for attachment is small giving rise to a very small attachment coefficient at low electric fields. The diffusion movement does not account for collisions and is considered a limitation of the model.

The electron transport over the gap also leads to the production of singlet oxygen across the gap with densities close to 1×10^{10} cm^{-3} and a peak of close to 1.5×10^{12} cm^{-3}. The singlet oxygen will react with the negative ions to detach electrons, it can be stated that singlet oxygen can only be influential where there are relatively high densities of both singlet oxygen and negative ions. The reaction is shown below.

$$O_2^- + O_2(a^1\Delta_g) = 2O_2 + e$$

Figure 3.10 illustrates the peak negative ion densities, the electric field and the distance from the electrode. What is distinctly evident in negative corona is that negative ions are formed away from the cathode, and that after each Trichel pulse a negative ion cloud is formed (2200ns). The negative ions are shown to drift away from the cathode and the electric field is shown to be below the critical field level where attachment is greater than ionisation (Figure 3.2). This is crucial as an electron released by the reaction of singlet oxygen and the negative ions (as shown in the equation below) is likely not to influence the gas discharge process as it will become re-attached.

Figure 3.12 illustrates that the trend of negative ion clouds continues over time and illustrates that the high densities are formed outside of the critical field region.

The question remains what influence does the singlet oxygen have on the gas discharge when a negative polarity is applied and it can be inferred that in the negative process that the supply of secondary electrons from the cathode due to ion bombardment and photoionisation are the dominant mechanisms and lead to the repetitive nature of negative corona, which is consistent with the theory [14, 16], and that singlet oxygen has no influence.

Additionally with a neutral density of 2.5×10^{25} cm^{-3} and a quenching rate

of 2×10^{-18} cm^3.s^{-1}, the expected emission is 7.5×10^{10} photons per cm^3 per nanosecond. This will consist of the infrared emission at 1270 nm, which is known to be weak, and the red emission at 634 nm due to the singlet oxygen dimol. The emissions exist, but it may be difficult to isolate and measure, however based on the modelling and argument above the value in measuring the emission for negative corona would add no value.

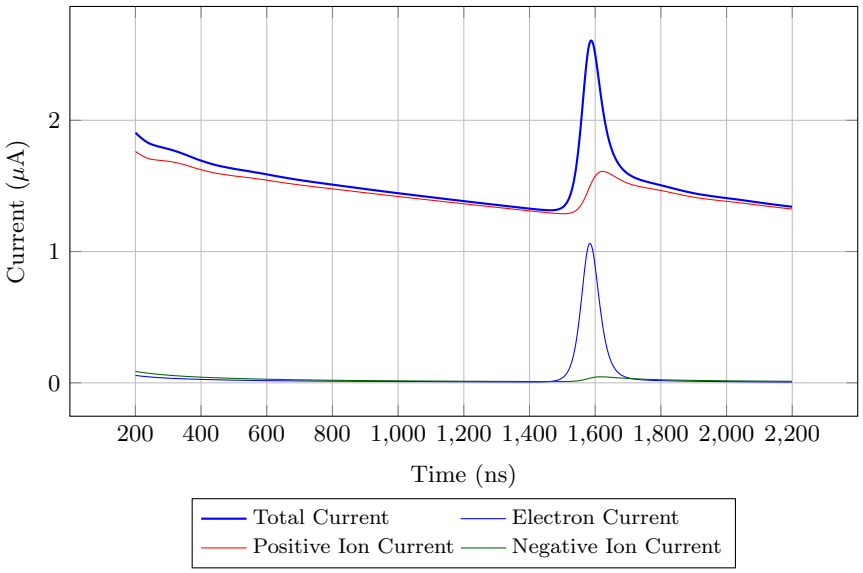

Figure 3.9: External Circuit Current up to 2200 ns

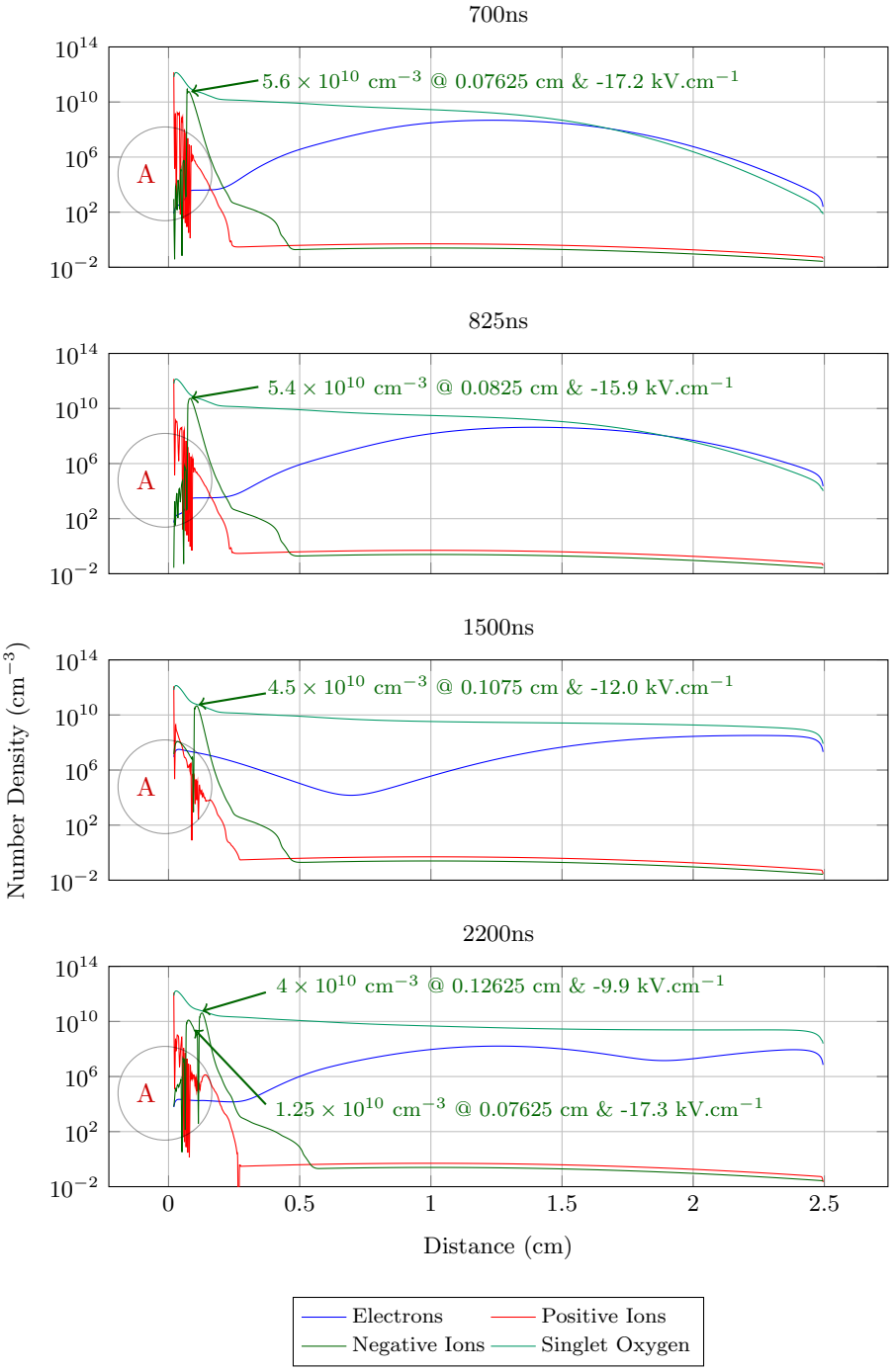

Figure 3.10: Development of Space Charge after Trichel pulse

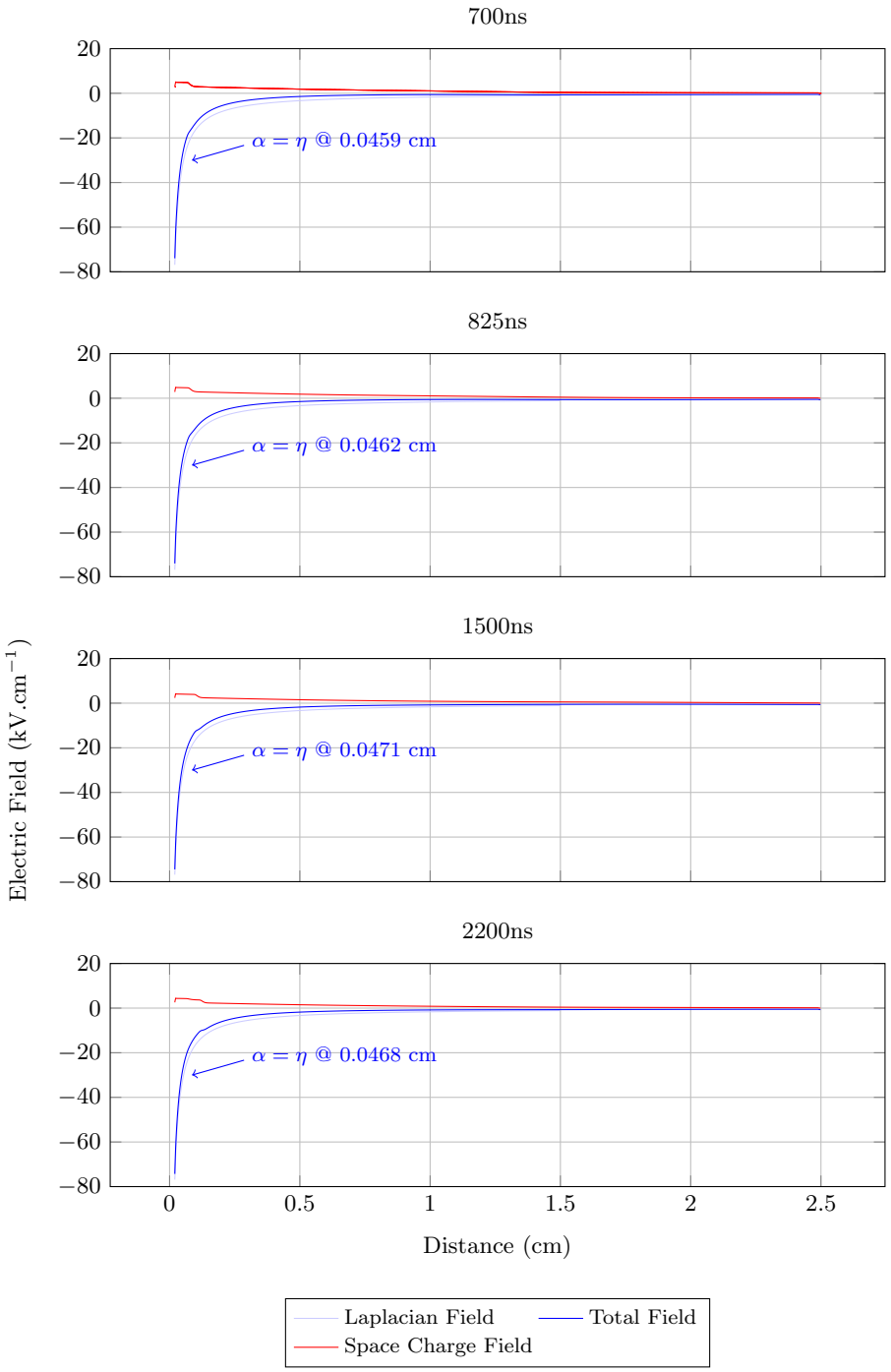

Figure 3.11: Development of Electric Field after Trichel pulse

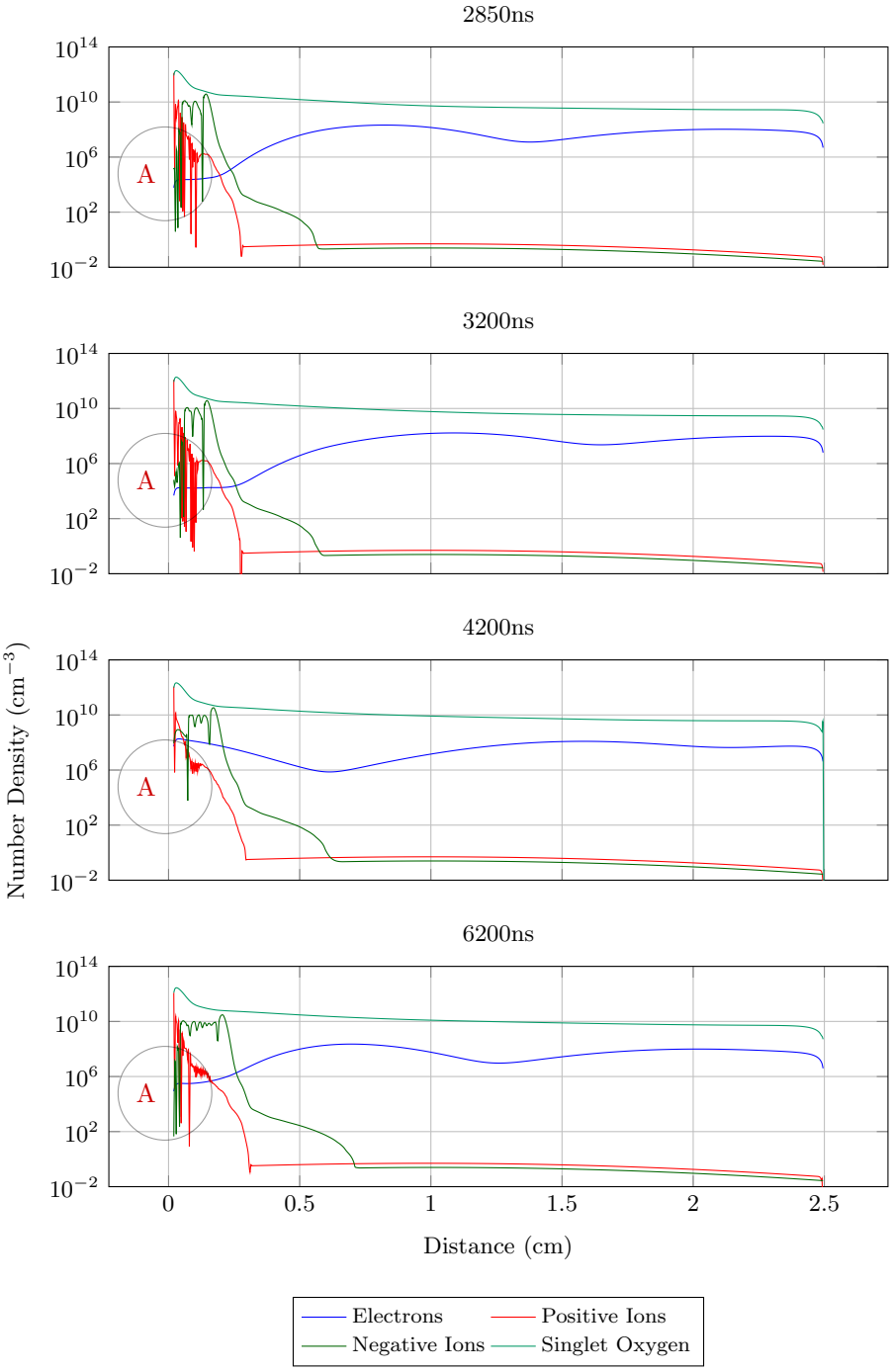

Figure 3.12: Development of Space Charge after Trichel pulse

Trichel Pulses

Trichel pulses are characterised by their shape and their repetition rate as discussed in Chapter 2. To ensure that the Trichel pulses produced by the model are repeatable under different conditions and consistent with theory, the model is adjusted for:

- Applied voltage ±1 kV to determine the change in repetition rate due to applied voltage
- Ion mobilities by a factor of 2 to determine the influence on the movement of space charge on the repetition rate
- Airflow (Implemented as an ion and molecules sink based on an airflow rate of 5 $cm^3.s^{-1}$) to determine the influence of a shift in space charge on the repetition rate
- No singlet oxygen to confirm that the singlet oxygen has no influence on the repetition rate of negative corona

According to Sato's equation the current is proportional to the sum of the movement of all the charged species, it is felt that the model doesn't reach a steady state and as such there is a dc offset caused by the flow of positive ions. As such the currents due to the electrons are felt to be a better measure of the model as illustrated in Figure 3.13 and Tables 3.3 and 3.4.

It is clear from the figures that the movement (drift dominated) of the space charge determines the period between pulses as the period:

- Decreases when the applied force (voltage) is increased and increases when the voltage is decreased
- Decreases when the mobility of the ions is increased
- Decreases when the airflow is applied to the system
- Remains almost the same when singlet oxygen is removed from the equation

A decrease in period would correspond to an increase in repetition rate. This is consistent with the theory of negative corona presented in Chapter 2, where an increasing voltage would increase the repetition rate. The higher voltage would provide a greater drift velocity for the space charge to clear at a higher rate. This is confirmed by altering the mobility of the ions, where the higher mobility would produce a higher drift velocity and clear the space charge at a higher rate. The application of airflow in the form of an ion and molecule sink produced a slightly lower period, and would result in a higher repetition rate.

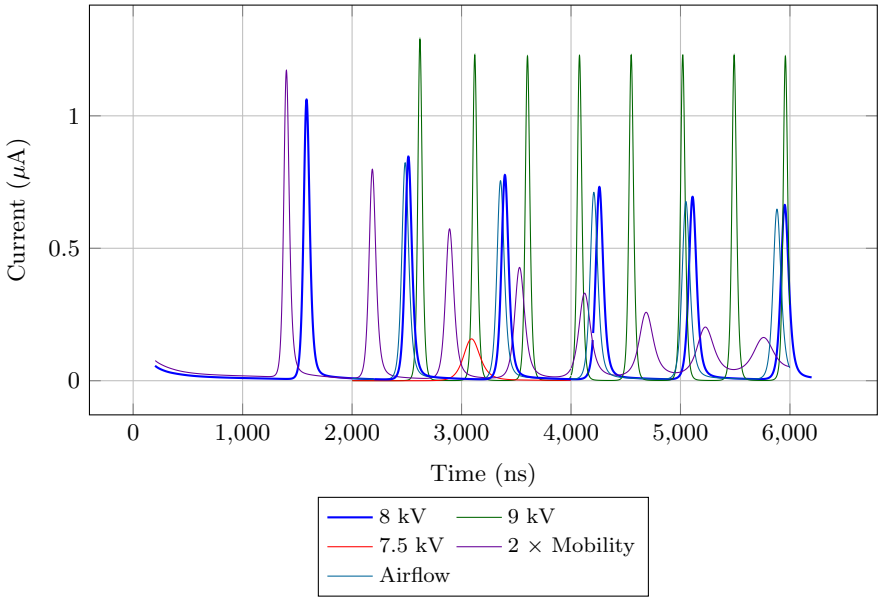

Figure 3.13: Trichel Pulses for Multiple Cases

It is evident that the initial peak of the corona differs for the different applied parameters. This is not considered false, as the high voltage for example will lead to a higher ionisation and faster movement. In the presence of space charge, the densities are high enough that the collapse of the field happens earlier causing more consistent and comparable results.

Table 3.3: Trichel Pulse Periods

	Period ns					
Period	8 kV	7.5 kV	9 kV	Mobility	Airflow	No $O_2(a^1\Delta_g)$
Pulse 1 to 2	1554	275	2614	1371	1537	1625
Pulse 2 to 3	931	2832	501	787	921	939
Pulse 3 to 4	882	2305	481	707	871	884
Pulse 4 to 5	863	-	475	641	852	863
Pulse 5 to 6	851	-	473	597	842	852
Pulse 6 to 7	843	-	471	564	832	-
Pulse 7 to 8	-	-	469	544	-	-
Pulse 8 to 9	-	-	468	532	-	-

Table 3.4: Trichel Pulse Peaks

	Peak Current μA					
Period	8 kV	7 kV	9 kV	Mobility	Airflow	No $O_2(a^1\Delta_g)$
Pulse 1	44.4	1.72	240	46.08	36.97	
Pulse 2	2.61	0.34	6.49	4.23	2.54	
Pulse 3	2.34	0.27	6.37	3.77	2.27	
Pulse 4	2.23	-	6.33	3.46	2.18	
Pulse 5	2.15	-	6.30	3.24	2.11	
Pulse 6	2.09	-	6.27	3.08	2.05	
Pulse 7	2.03	-	6.26	2.96	1.99	
Pulse 8	-	-	6.23	2.86	-	
Pulse 9	-	-	6.21	2.78	-	

3.3.2 Positive Corona

The parameters used in the model are listed in Table 3.5, where a uniform grid is used. The grid spacing has to be fine close to the electrode for the solution to be meaningful and this comes at the expense of a shorter time step. The major difference with the parameters used for the negative corona is the higher applied voltage.

Table 3.5: Input Parameters for Positive Corona Model

Parameter	Symbol	Value
Pressure	P	760 torr
Temperature	T	20 °C
Anode radius	r	0.02 cm
Electrode spacing	d	2.5 cm
Grid size	N_g	800
Grid spacing	dx	0.03 cm
Time step	dt	1×10^{-12}
Secondary ionisation coefficient	γ	0.01
Recombination coefficient	β	2×10^{-7}
Ion-singlet detachment coefficient	k_d	2×10^{-10}
Singlet quenching coefficient	k_q	2×10^{-18}
Mobility of positive ion	μ_p	2.34 $cm^2.V^{-1}.s^{-1}$
Mobility of negative ion	μ_n	2.7 $cm^2.V^{-1}.s^{-1}$
Diffusion of positive ion	D_p	$5{\times}10^{-2}$ $cm^2.s^{-1}$
Diffusion of negative ion	D_n	$5{\times}10^{-2}$ $cm^2.s^{-1}$
Applied voltage	V_a	9 kV

An initial plasma number density is applied to the system, which gives a peak electron and positive ion density of 0.9995 cm^{-3} at 0.02 cm.

$$N_i = \exp(-(x + dx)^2) \tag{3.22}$$

Initial Corona Pulse

The external circuit current is illustrated in Figure 3.14. It is clear that the magnitude of the pulse is greater than the Trichel pulse and that the movement of positive ions plays a much larger part in the process. This is due to the initial streamer mechanism and the difference in the alteration of the electric field due to space charge. This is also consistent with known theory and published information where the positive onset streamer has a far greater magnitude than the negative Trichel pulse.

The space charge development for 100 ns of the corona pulse is illustrated in Figures 3.15 and 3.17. The accompanying electric field development is illustrated in Figures 3.16 and 3.18, where the *Laplacian Field* refers to the electric field determined only by the voltage between the electrodes and the *Space Charge Field* refers to the electric field determined only by the space charge. It is clear that the process differs significantly from the negative corona pulse with the role played by the positive ions far greater than the negative ions. The positive ions are generated rapidly at the electrode reaching a peak density of 2.4×10^{13} cm^{-3} after 30 ns, with the fast moving electrons at less than half this density after 50ns. It is clear from Figure 3.16 that this distorts the field considerably causing a complete collapse near the electrode and a peak away from the electrode. This peak causes the streamer to propagate into the gap and the collapse prevents activity in the region close to the electrode. There will be no more ionisation activity until this space charge clears.

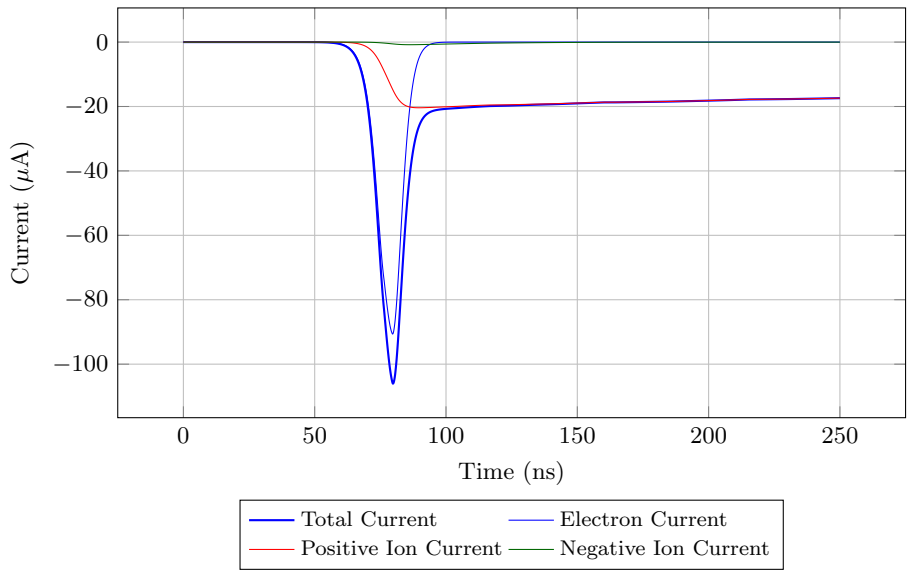

Figure 3.14: Positive Corona Pulse

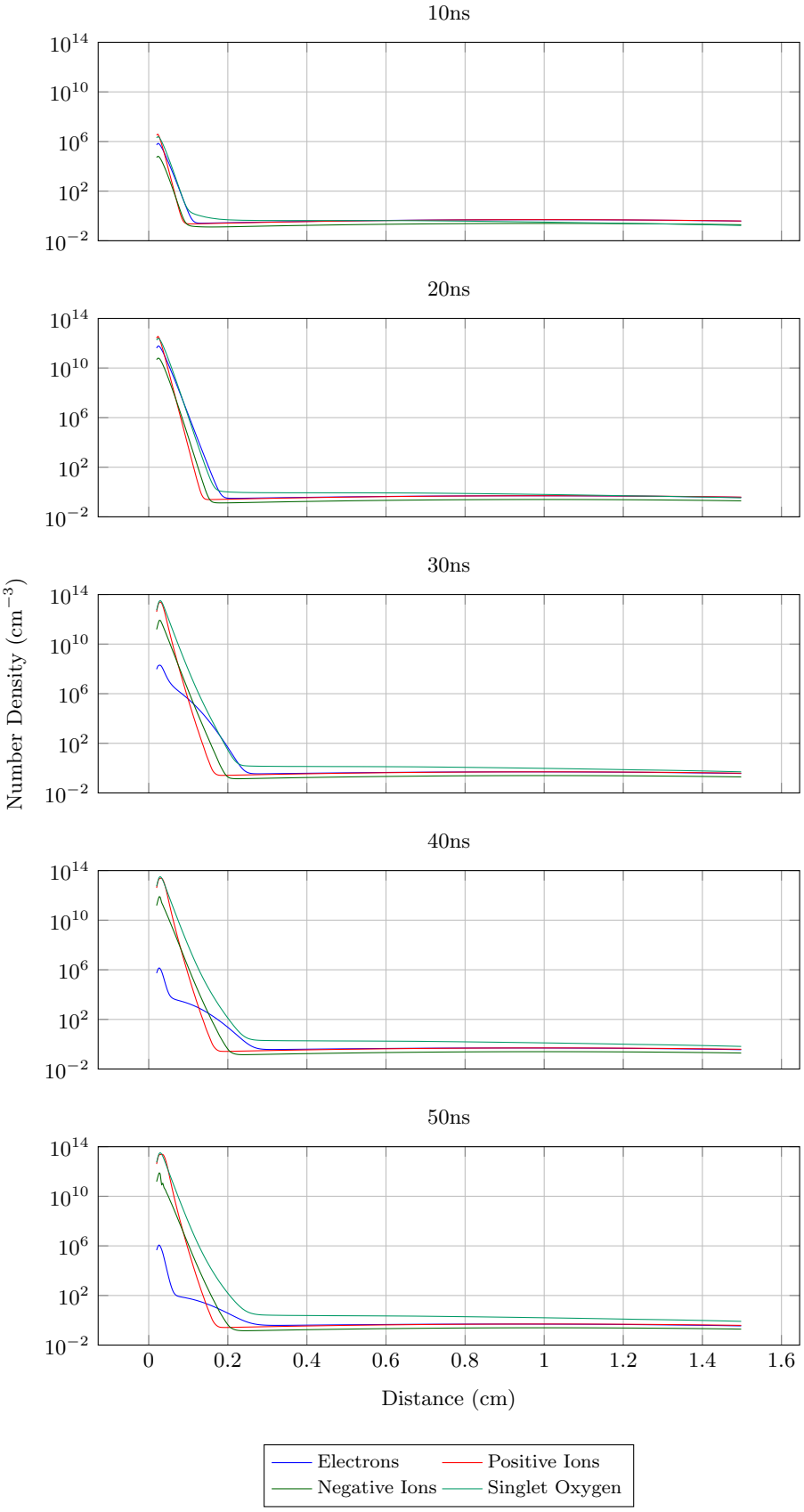

Figure 3.15: Development of Space Charge during Positive Corona Pulse

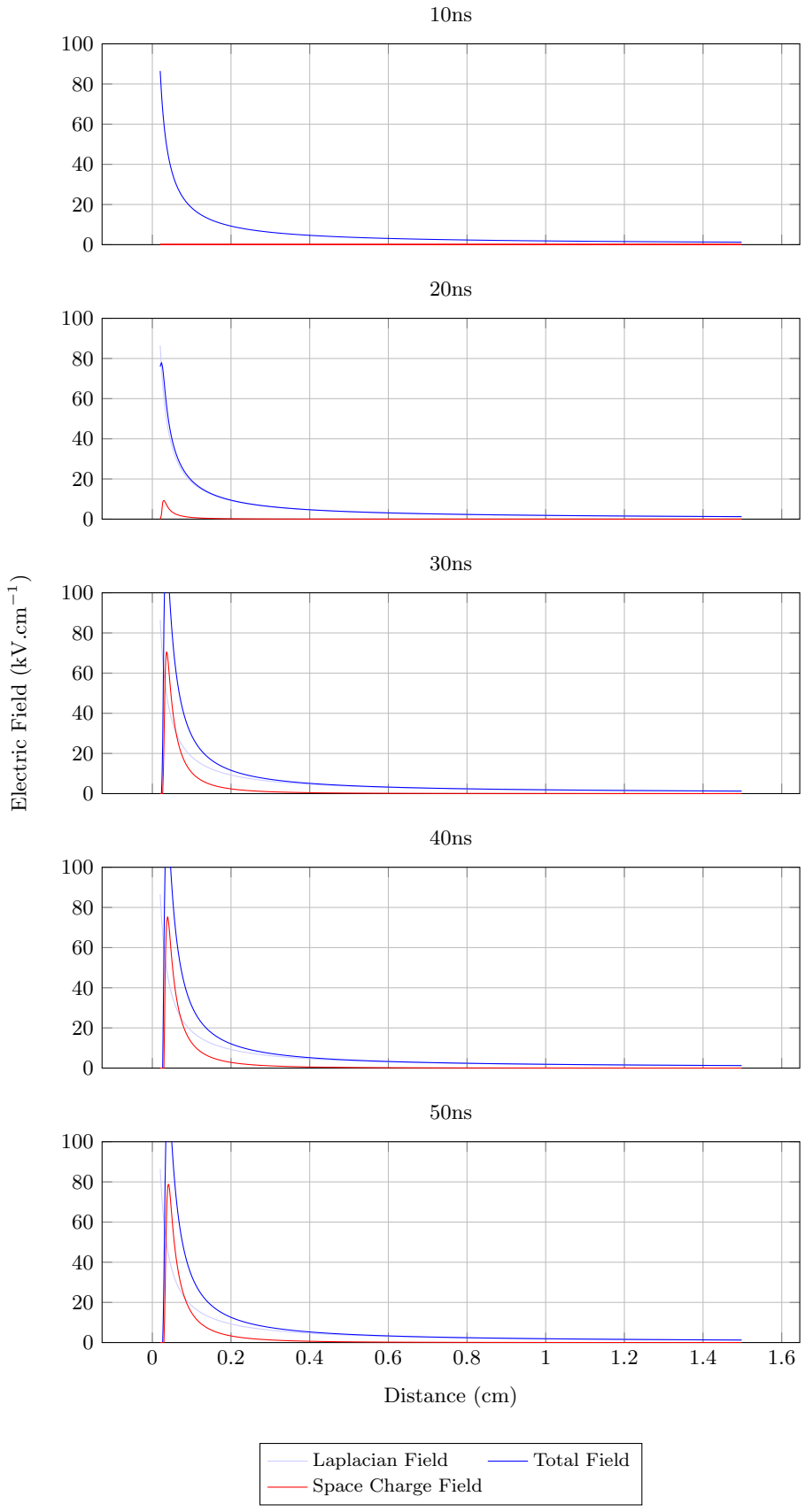

Figure 3.16: Development of Electric Field during Positive Corona Pulse

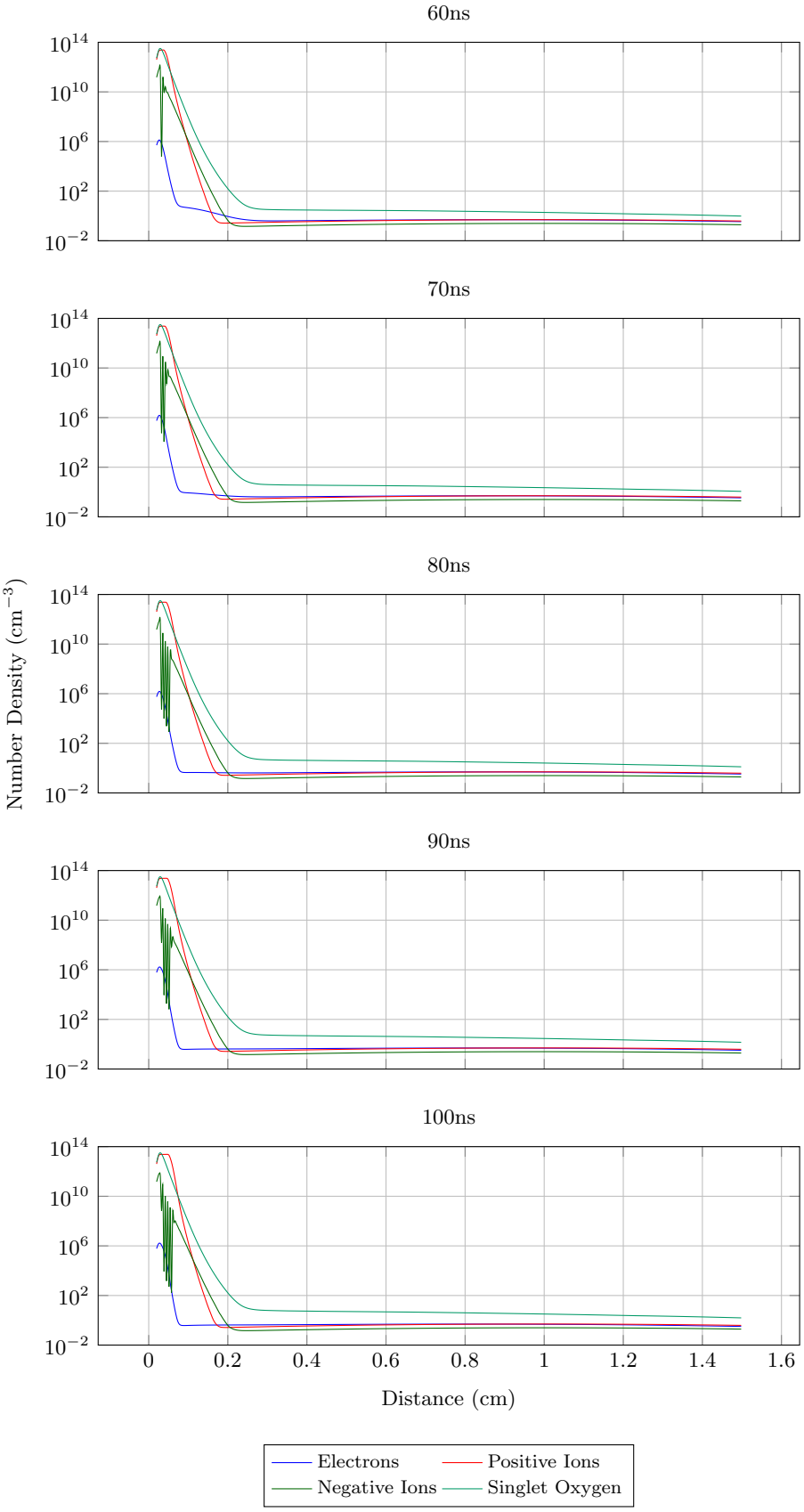

Figure 3.17: Development of Space Charge during Positive Corona Pulse

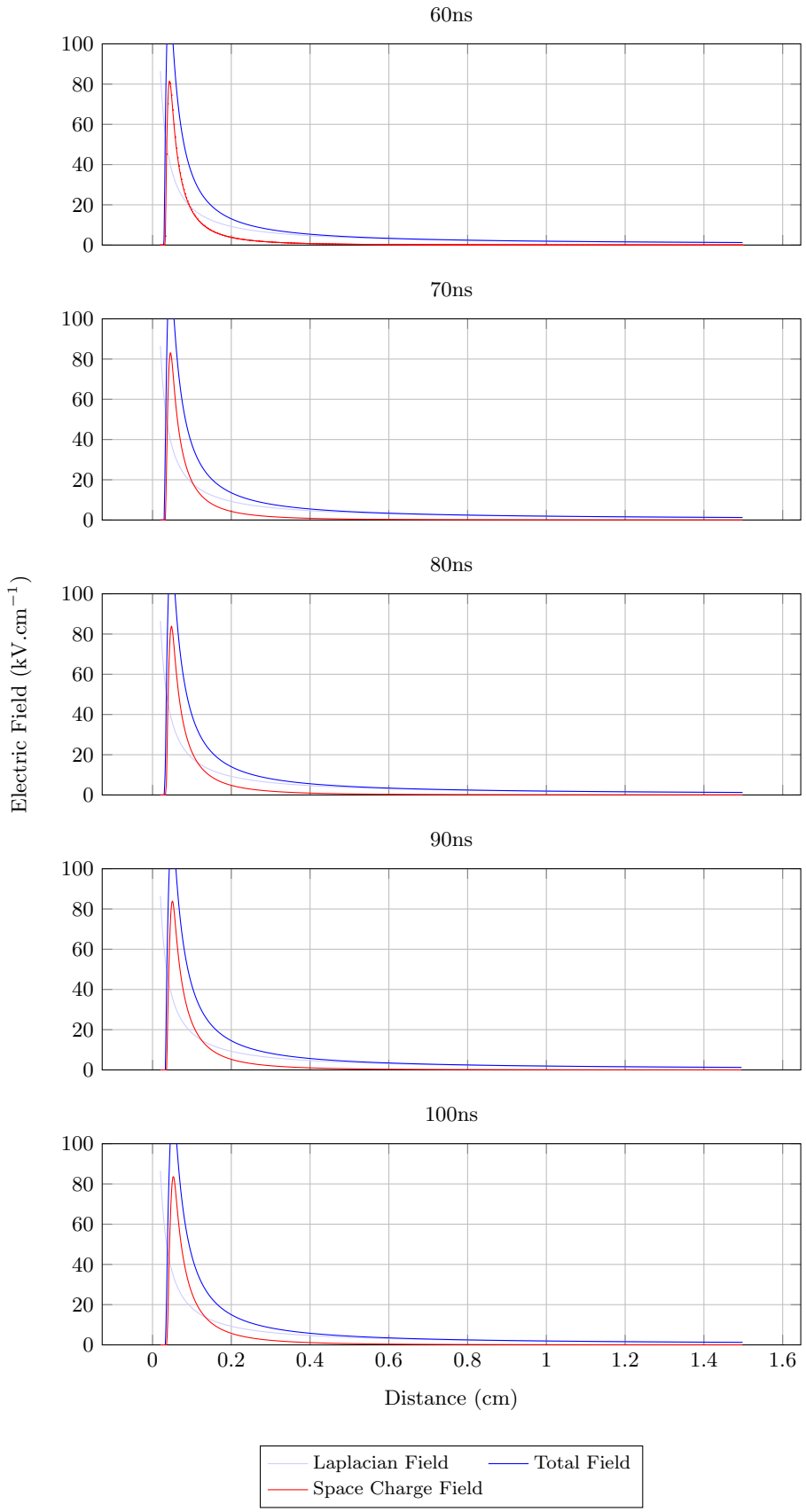

Figure 3.18: Development of Electric Field during Positive Corona Pulse

After Initial Corona Pulse

The space charge and electric field after the initial corona pulse are illustrated in Figures 3.19 and 3.20. The peak density and location of the peak are shown in Figure 3.19. Following the distortion of the field in the initial pulse, the field recovers slowly. Noting that the activities that occur where the field is collapsed include recombination of positive ions and electrons, recombination of negative ions, and detachment of electrons from the reaction of negative ions and singlet oxygen. There is no drift velocity as there is no electric field and as such the normal Townsend generation of species due to electron collision does not exist. While there is some value in the process, it is thought that the 1.5D model is limited in this respect.

The oscillations seen at B occur only for the negative ions for the positive corona. These are thought to be numerical errors due to the recombination of positive and negative ions and to the reaction of negative ions and singlet oxygen.

Singlet oxygen is generated within the region close to the cathode. After 4000 ns there is a peak singlet oxygen density of 8.5×10^{12} cm^3s^{-1} and a peak negative ion density of 3.92×10^{10} cm^3s^{-1}. With a neutral density of 2.5×10^{25} cm^{-3} and a quenching rate of 2×10^{-18} $cm^3.s^{-1}$, the expected emission is 4.25×10^{11} photons per cm^3 per nanosecond. The emission is slightly higher than that of negative corona it is however localised around the anode.

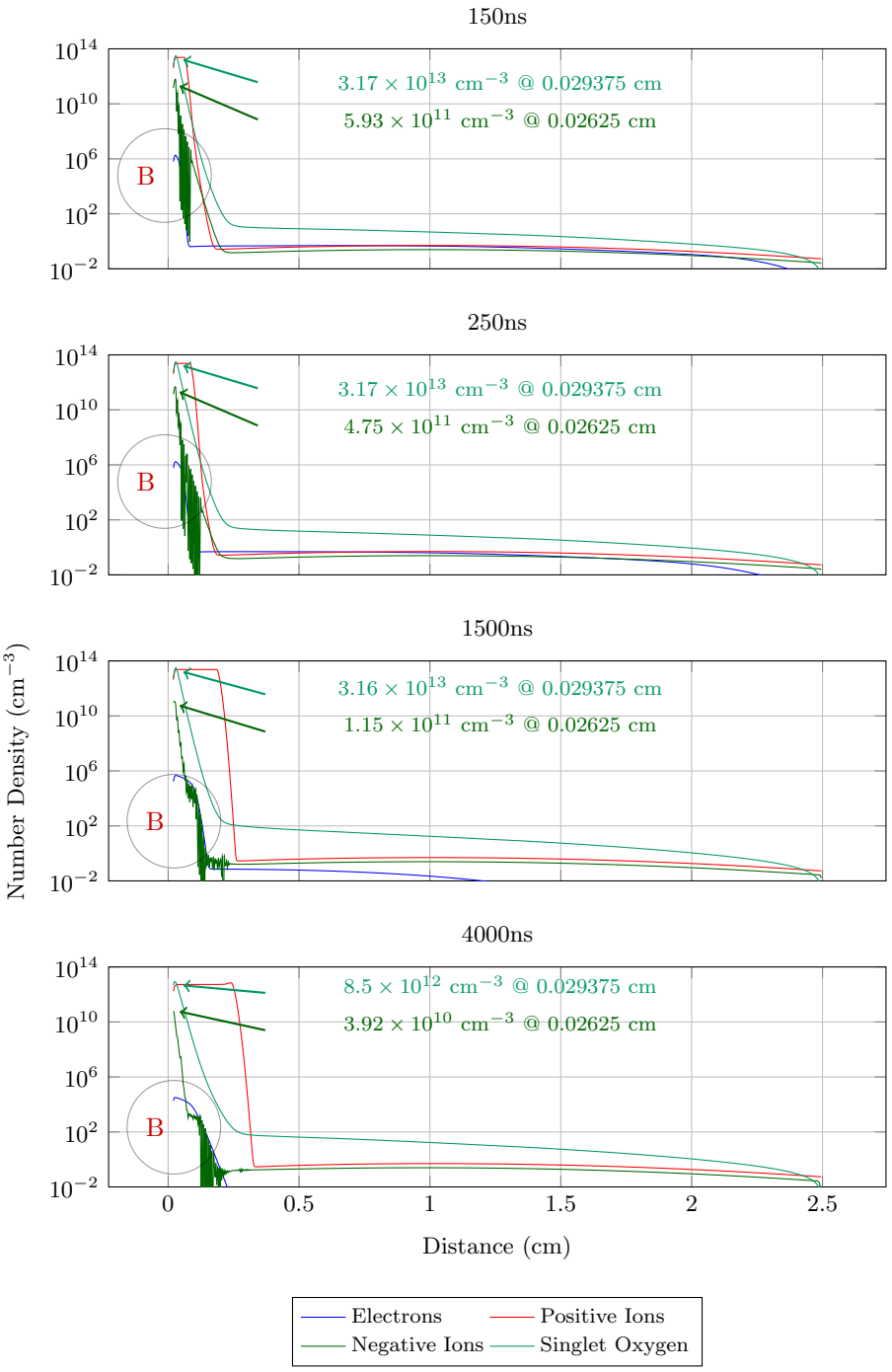

Figure 3.19: Development of Space Charge during Positive Corona Pulse

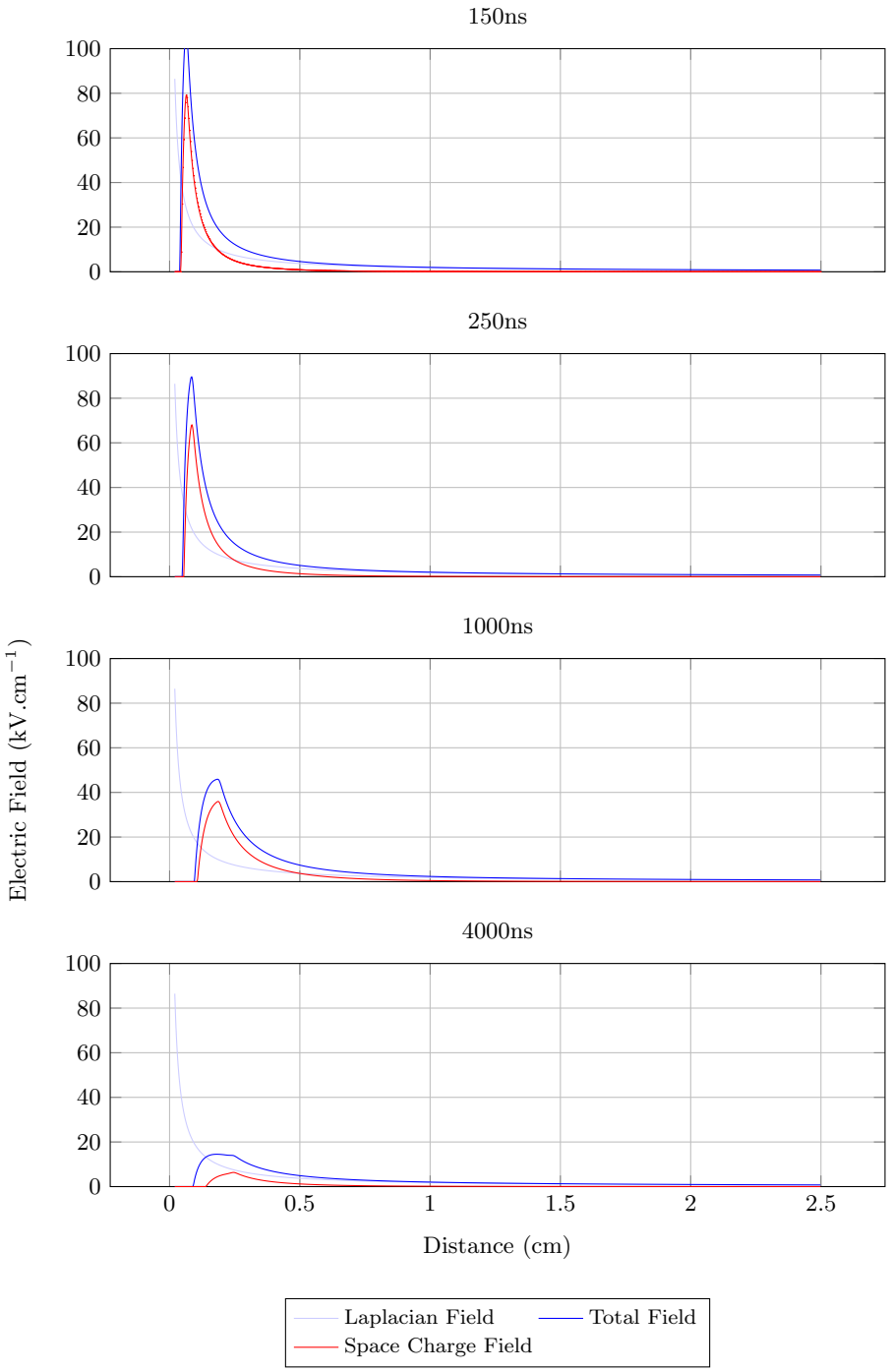

Figure 3.20: Development of Electric Field during Positive Corona Pulse

The preceding figures illustrate the high densities of negative and singlet oxygen and the corresponding collapse of electric field. As discussed in Chapter 2, positive corona is initiated by natural processes in the air, i.e. an electron needs to be freed by a natural processes. This electron then initiates the electron avalanche towards the anode and subsequent ion clouds are formed. These clouds cause a collapse in the electric field and another discharge can only occur when the electric field recovers and this leads to the different modes of corona. The slower recovery of the electric field in the model indicates why the repetition rate of positive corona is less that that of negative. The role of secondary electrons in positive corona becomes highly important as without an electron the discharge cannot occur. Referring to the reaction of negative ions and singlet oxygen below some of the roles that singlet oxygen may play can be extracted.

$$O_2^- + O_2(a^1\Delta_g) = 2O_2 + e$$

It illustrates that the reaction of O_2^- and $O_2(a^1\Delta_g)$ assist in the release secondary electrons and hence initiating the discharge. It could be that the reaction provides a constant source of secondary electrons.

To illustrate the argument Figure 3.21 overlays the negative ion and singlet oxygen densities at 4000 ns by the detached electrons considering a detachment rate of 2×10^{-7} cm^3.s^{-1} for the reaction shown above. This is slightly misleading as the negative ion and singlet oxygen densities are not constant over time and still decreasing, however, there is value in identifying that electrons are released. There is a peak rate of 2.55×10^7 cm^3.ns^{-1} at the anode and while this is a significant number, these electrons may be absorbed before impacting on the streamer. The rapid decline of detached electrons rate is clear in the plot and critical in extracting the influence of singlet oxygen. A higher density would be expected to initiate the streamer process, however the rate of 2.23 cm^{-3}.ns^{-1} where $\alpha = \eta$ for the initial electric field illustrates that there may be a small correlation between the positive streamer and the singlet oxygen density should the field recover to its initial state *as the initial*

streamer is started. This would have to be validated in through appropriate experimentation.

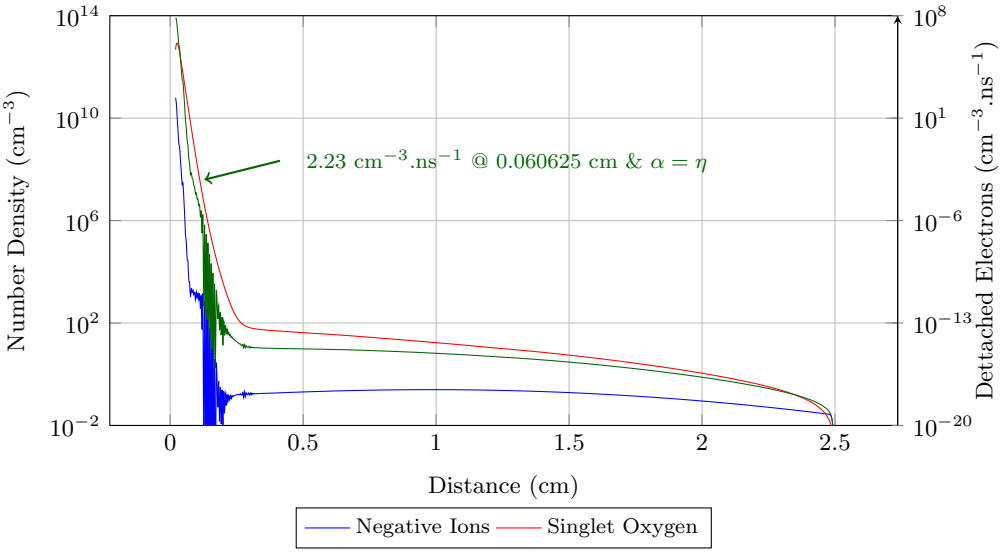

Figure 3.21: Negative Ion and Singlet Oxygen Densities overlaid by Detached Electrons

3.4 Discussion

The model has produced some interesting and applicable results, where it is evident that the space charge plays the dominant role in the corona process as it causes the electric field to collapse. The recovery of the electric field would allow the corona process to restart. The manner in which the field collapses and recovers is dependent on the polarity of the applied voltage.

Negative corona modelling has shown including Trichel pulses which alter under different applied conditions, this is critical as a basis to compare experimental work, particularly as the trends follow that of published measurements and modelling. The mechanism of corona is shown with the inclusion of singlet oxygen but it is the influence of space charge on the electric field and the rate at which it is removed that is critical to the repetition rate of Trichel pulses.

The positive corona modelling, or more appropriately modelling of a cathode directed streamer, has partially illustrated the mechanism of positive onset streamers and breakdown streamers, with the critical aspect being the collapse of the field close to the electrode (anode) due to the dominant positive space charge. The modification of the field is different to the negative corona, where the field is enhanced or remains high next to the electrode (cathode).

The presence of singlet oxygen is evident in both negative and positive corona, with fairly low emission rates. The results suggest that the recovery of the electric field due to space charge is the critical process in the corona discharge and is responsible for preventing the discharge from repeating. In negative corona the production of seed electrons would be in a region where they would not influence the discharge or the repetition rate. In positive corona there is evidence that suggest the reaction of negative ions and singlet oxygen could lead to that production of seed electrons, the rate would be very small and may be unimportant in the corona process.

The conclusions extracted from the modelling lead to the need to experimentally validate them

- Influence of altering the state or environment of positive and negative corona to confirm that it is consistent with the conclusions drawn from the modelling
- Measurement of singlet oxygen in a system in positive corona where there could be a relationship
- Directly influence the density of singlet oxygen in a system for positive corona where there could be a relationship

Chapter 4

Experiments

It is known that corona needs a source of electrons to initiate the discharge and cause it to repeat, in the case of negative corona the bombardment of the cathode by ions causes the repetition rate to be quite consistent. Any consistent repetition rate of positive corona would need a regular source of electrons and it is hypothesised that the reaction of negative ions and singlet oxygen may play a role in positive onset streamers. The initial experiment which led to the hypothesis and research direction is presented at the start of the chapter. This chapter presents the experiments used to validate the conclusions established and queries identified in Chapter 3 by manipulating the system with a specific focus on positive onset streamers and the reaction between negative ions and singlet oxygen.

4.1 Measurement System

Due to the complexity of the corona discharge it is useful to quantify and understand corona in terms of the corona pulse, amplitude, repetition rate, energy and power, which are all based on the current measurement. The measurement system was generic for all the tests and consisted of 1 $k\Omega$ resis-

tors to measure the change in surface charge on the base and side electrodes as shown in Figure 4.1. While it was understood that the supply and system itself will disturb the measurement through resonance or leakage, the system was deemed the most appropriate as illustrated in Appendix B. The details and dimensions of the the test vessel are found in Appendix H.

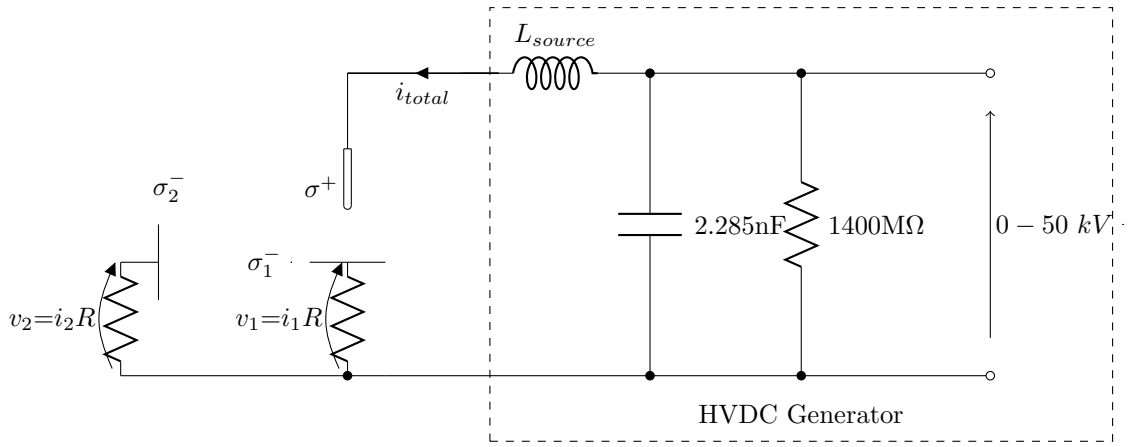

Figure 4.1: Measurement System

The total current consists of both a conduction current due to the electrons and ions moving across the gap and a displacement current ($J_d = \epsilon_0 \frac{\partial(E)}{\partial(t)}$) due to the changing electric field [60, 61]:

$$i_{total}(t) = \int \vec{J}_c dA + \int \vec{J}_d dA \tag{4.1}$$

As the applied field is direct current the displacement current may be excluded (noting that this is not entirely true as the field does fluctuate with the moving space charge) giving [60, 61]:

$$i_{total}(t) = \pi r^2 \frac{q}{V_A} \int_0^d (N_p v_p - N_n v_n - N_e v_e + \frac{\partial^2 D N_e}{\partial^2 x}) E_L dx \tag{4.2}$$

Considering Gauss' Law for the electrode system written as the circuit current is given by [29]:

$$\oint_S \vec{E}_s.ds = \int_V \frac{\rho}{\varepsilon} dV + \frac{A^+\sigma^+ + A_1^-\sigma_1^- + A_2^-\sigma_2^-}{\varepsilon} = 0 \tag{4.3}$$

Where:

$\vec{E}$ = Electric field [v.m^{-1}]
V = Volume [cm^3]
ρ = Space charge [C.cm^{-3}]
ε = Permittivity
σ^+ = Surface charge of point electrode [C.m^{-2}]
σ_1^- = Surface charge of plane electrode 1 [C.m^{-2}]
σ_2^- = Surface charge of plane electrode 2 [C.m^{-2}]
A^+ = Area of point electrode [m^2]
A_1^- = Area of plane electrode 1 [m^2]
A_2^- = Area of plane electrode 2 [m^2]

Gauss' law states that at any time the sum of the surface charge densities of the electrodes is equal to the space charge integral, essentially validating the method of measurement. The measurement of the repetition rate of corona and the peak corona pulse current are parameters of interest as they are related to the movement of space charge and behaviour of the electric field as shown by the above equations and modelled in Chapter 3.

4.2 Air Flow Experiment

Corona was to be tested under air flow conditions, where the air was particular slow with a maximum of 2.5 m.s^{-1} thus maintaining incompressible flow and as such would not effect density at the point. The purpose of the moving air was to act as a sink for space charge and for excited air molecules, such as singlet oxygen.

Nygaard investigated Trichel pulse under air flow conditions of 2 to 18 m.s^{-1} and noted a significant decrease in the repetition rate of the pulses stating that this was due to the removal of negative space charge [64]. Trichel pulses

are highly dependent on the electric field closer to the cathode; the negative ion space charge has the effect of sharply increasing the electric field near the electrode and increasing the Trichel pulse repetition rate; any influence on this as a sink would logically decrease the repetition rate.

Corona has been studied under air flow conditions by Jaworek and Krupa who tested corona in a multipoint electrode system with air flow up to 4 $m.s^{-1}$. It was shown that positive current increases in the range from 0 to 0.5 $m.s^{-1}$ and then decreases again. The experiments showed that the corona onset voltage and breakdown occur 25% higher than still air at an air flow of 4 $m.s^{-1}$ [65].

Abdel-Salam et al investigated the effect of traverse and axial winds on positive point-plane corona and found that wind would alter the repetition rate of the pulses depending on the direction of the wind. It was shown that a transverse wind would increase the breakdown voltage of the gap [66].

Due to the inconsistent nature of positive corona, it has not been explored to the same degree as negative corona.

4.2.1 Initial Experiment and Research Plan

The purpose of the initial air flow experiment was to investigate whether the space charge moved with low air flow rates, particularly for positive corona, which the author felt had not been explored as much [67]. The initial intention of the experiment was to measure the DC current which would be considered the ion current in the system [67]. The results proved interesting and led to the hypothesis of the influence of singlet oxygen on the discharge process.

The positive point plane experiment was set up as illustrated in Figure 4.2 where the gap length was 10 cm with a electrode tip radius of 2.5 mm. The reason for the larger tip was to ensure that the onset streamers were achievable in the system. A vacuum pump was applied to one end of the point

plane gap to move air out of the system at a rate of 2.5 m.s^{-1}. The tests were performed at an altitude of 1700 m at the High Voltage laboratory at the University of the Witwatersrand.

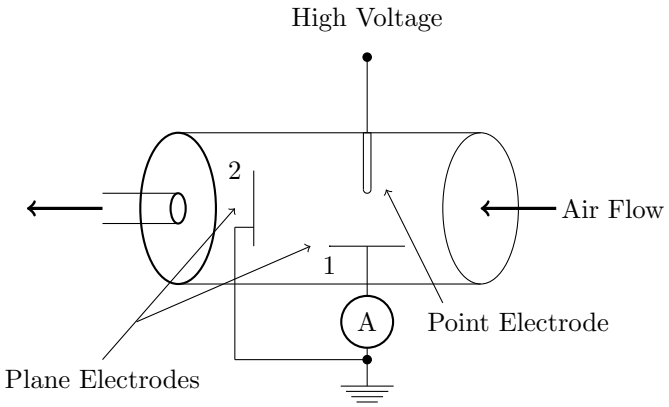

Figure 4.2: Positive Point Plane Experiment

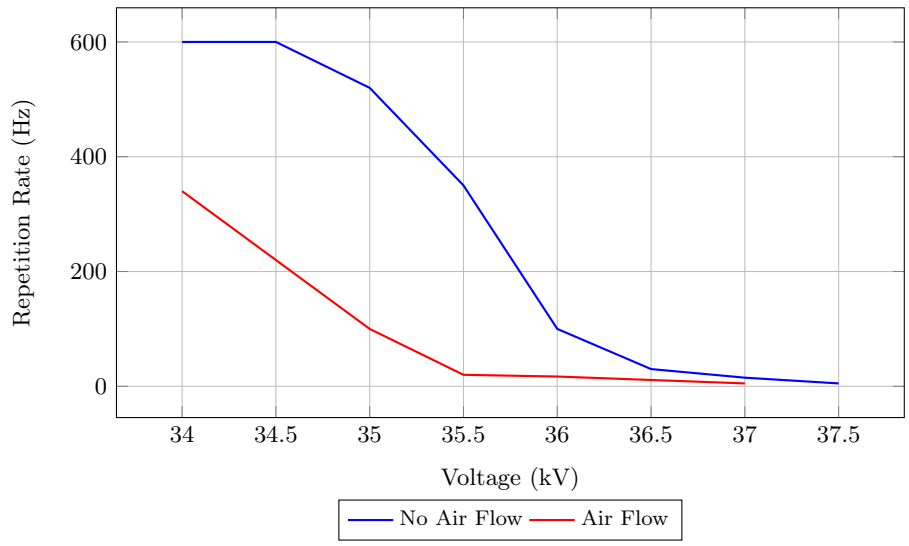

Figure 4.3: Repetition Rate of the Initial Positive Point Plane Experiment

For the experiment the following general characteristics are observed [67]:

- Burst corona occurs from 30 kV to 33 kV with intermittent corona pulses and no stable measurable repetition rate.

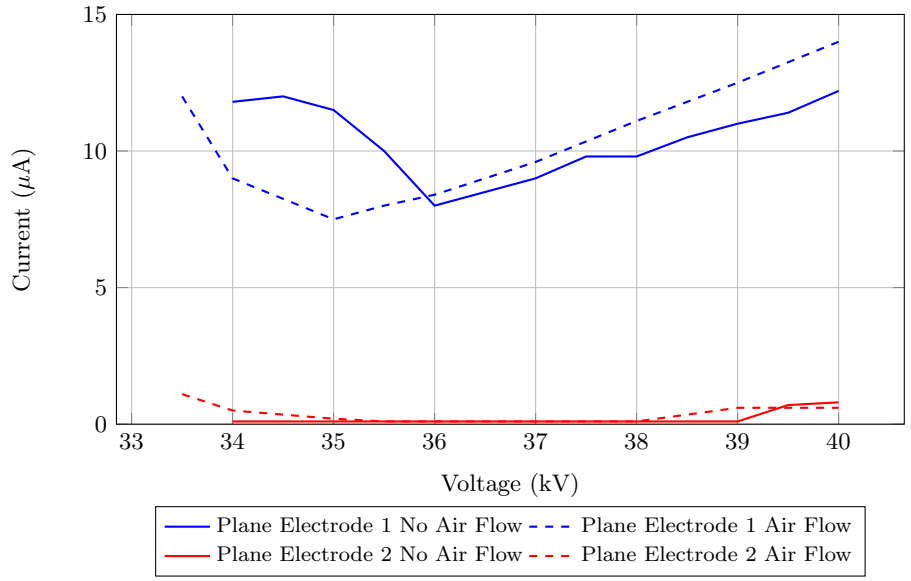

Figure 4.4: DC Current of the Initial Positive Point Plane Experiment

- Positive onset corona occurs from 34 kV to 37.5 kV with consistent corona pulses and a stable measurable repetition rate.
- From 37.5 kV to 40 kV the corona pulses are intermittent with no stable measurable repetition rate.

Figure 4.3 illustrates the repetition rate of positive onset streamers between 34 kV and 37.5 kV and Figure 4.4 illustrates the DC current between 33.5 kV and 40 kV. The DC current for the no airflow experiment illustrated that the space charge moved towards the plane electrode 1. It can be seen that the current follows the same shape as the repetition rate and reduces until it reaches 36 kV where it steadily increases. It can be seen that there is no current through plane electrode 2 as the space charge does not come close enough to affect the surface charge of electrode. This changes slightly under airflow conditions, where it can be seen that the DC current is higher than previously on plane electrode 2. Intuitively this makes sense as a small amount of space charge moves towards the side and alters the surface charge of the plane electrode. The DC current measurements again follow the shape of the repetition rate.

The large change in the repetition rate in Figure 4.3 was of more interest as it did not make complete sense that a small shift in space charge would cause such a large shift in repetition rate. Jaworek and Krupa found a 25% increase in corona onset while shown above is there same onset, but lower repetition rate, they did however have multiple electrodes [65]. With a mobility of 2.34 $cm^2/V/s$ the drift velocity in an applied electric field of 1 kV/cm is 2340 cm/s [13, 67]. The velocity of the air flow is 2500 cm/s, considering that the electric field is not uniform and will be higher than 1 kV/cm near the anode, the velocity of the charged positive ions should be higher than the velocity of the air and would drift to the electrode before being influenced. Meaning that there may have been some other influence on the change of repetition rate [67].

The reaction between negative ions and singlet oxygen could have been the important source of secondary electrons for positive onset streamers.

$$O_2^- + O_2(a^1\Delta_g) = 2O_2 + e$$

Morrow in his modelling experiments for positive glow illustrated that singlet oxygen needed to be included for the process [3], although the mode investigated here was different, the equation illustrated that the reaction of O_2^- and $O_2(a^1\Delta_g)$ produced secondary electrons and hence may initiate the discharge.

Re-considering the highest repetition rate of of 600 Hz, the flow of air would have a duration of 1.7 ms between pulses to remove the non-drifting singlet oxygen that could influence the production of seed electrons [67]. This duration is relatively long in gas discharge dynamics.

The initial experiment in conjunction with the conclusions drawn from the modelling informed the structure of the experimental approach that follows in the coming sections.

- Investigate the different modes of positive and negative corona under

air flow conditions to ensure that the modelling has not shown anything inconsistent with the experiments and if the positive onset streamer is the only seemingly inconsistent mode. The repetition rate and the peak current are the measurement parameters of interest as they are related to the movement of space charge and behaviour of the electric field.

- Would the singlet oxygen density be measurable and if so, what relationship could be drawn by the density of singlet oxygen and repetition rate of positive onset streamers.
- Would it possible to influence the density of singlet oxygen and determine if the positive onset streamers are influenced by the density. Confirming that singlet oxygen does have an influence.

4.2.2 Positive Corona

The modelling in Chapter 3 illustrated that in the mechanism of positive corona the electric field collapses which is the distinct difference to negative corona. Positive corona needs secondary electrons to sustain a repetitive discharge and there is no real means to determine where this electron comes from. It has been suggested in Chapter 3 and from the initial experiment that the reaction of singlet oxygen and negative ions could play a part in producing a secondary seed electron.

The positive point plane experiment was set up as illustrated in Figure 4.5 where the gap length was 10 cm with a electrode tip radius of 2.5 mm. The larger tip again ensured that the onset streamers and glow are achievable in the system. A vacuum pump was applied to one end of the point plane gap to move air out of the system at a rate of 0 to 2.5 $m.s^{-1}$. The tests were performed at an altitude of 1700 m at the High Voltage laboratory at the University of the Witwatersrand.

The repetition rate was an average of the minimum and maximum observed repetition rate in a set sample time and the average peak current was the

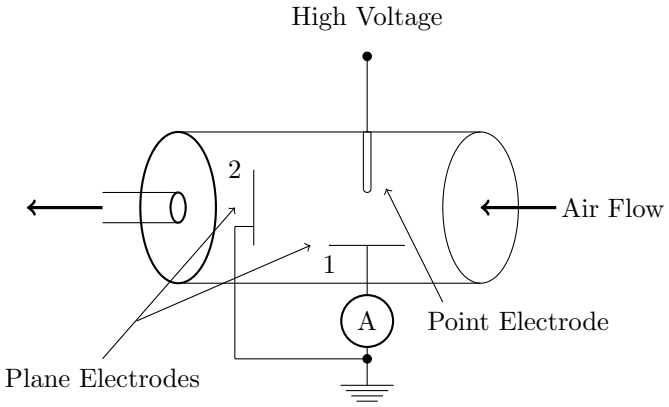

Figure 4.5: Positive Point Plane Experiment

peak current of an average of 256 samples.

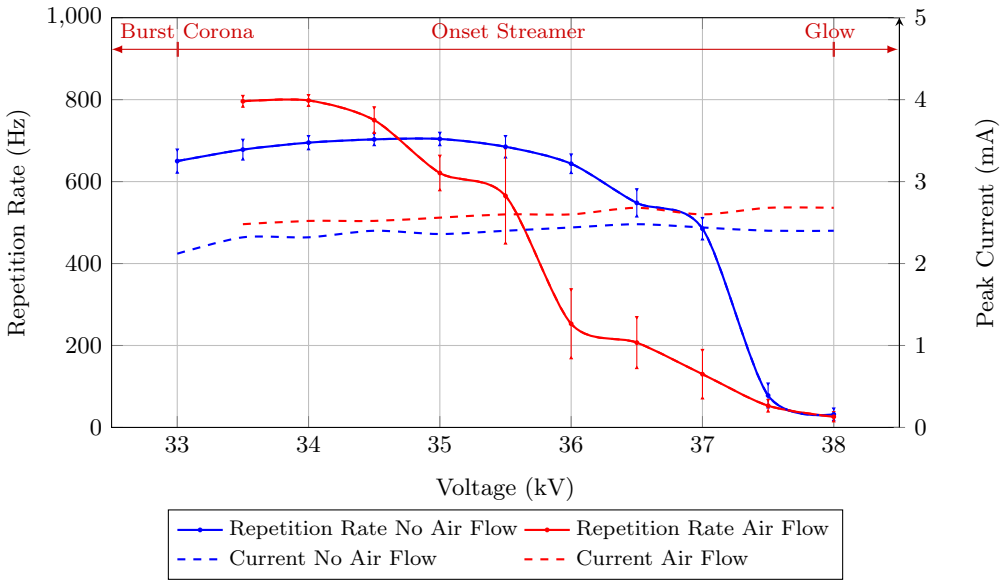

Figure 4.6: Repetition Rate and Average Peak Current

The results in Figure 4.6 illustrate the approximate regions of burst, onset streamer and glow corona for the point plane experiment. It is evident that the air flow had an influence on the nature (and mode) of the corona, where initially the onset streamers increased in repetition rate and then sharply de-

creased in repetition rate. The average peak current was consistently higher for the air flow condition for all the applied voltages. Referring to equation 4.2, the average peak current is dependent on the movement of the space charge and any small shift would cause the peak current to change slightly, which is evident in Figure 4.6.

The repetition rate of onset streamers are related to the collapse of the electric field at the conductor due to the positive space charge and the recovery due to the removal of the positive space charge [14], any influence on this space charge should theoretically result in an increase in the repetition rate as the field is restored faster. The results under air flow conditions were partially inconsistent with this theory.

The fact that the average peak current has a relatively small deviation and the repetition rate has a large deviation lends credibility to the hypothesis that singlet oxygen may be a source of seed electrons and be related to the repetition rate of the onset streamers. The detachment of electrons from negative ions would be dependent on both the density of negative ions and singlet oxygen and the slow moving air removes the singlet oxygen from the system and does not allow it to build up. Referring to the modelling of positive corona in Chapter 3, the densities of singlet oxygen and negative ions may not be large enough to react and produce sufficient seed electrons away from the anode.

To confirm whether this phenomena of a reduced repetition rate was repeatable for other configurations and under negative conditions a needle plane experiment was conducted.

The positive needle plane experiment was setup as shown in Figure 4.7 where the gap length was 9.5 cm with a needle tip radius of 0.1 mm. A vacuum pump was applied to one end of the point plane gap to move air out of the system at a rate of 2.5 m.s^{-1}. The results in the positive needle-plane experiment proved difficult to repeat due to the inconsistent nature of positive

corona. The tests were performed at an altitude of 1700 m at the High Voltage laboratory at the University of the Witwatersrand.

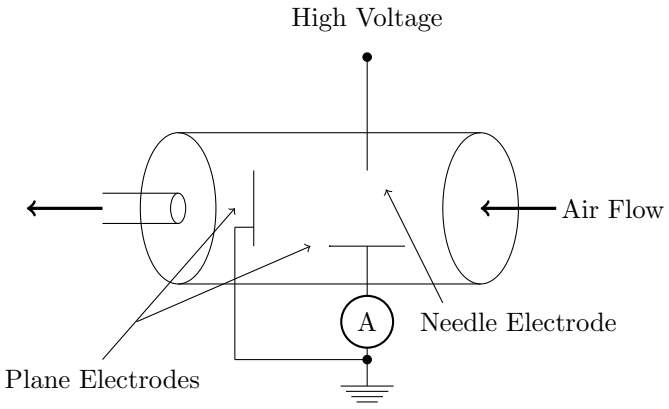

Figure 4.7: Positive Needle Plane Experiment

The results in Figure 4.8 illustrate the repetition rate and average peak current of breakdown streamers where the repetition rate was an average of the minimum and maximum observed repetition rate in a set sample time and the average peak current was the peak current of an average of 256 samples.

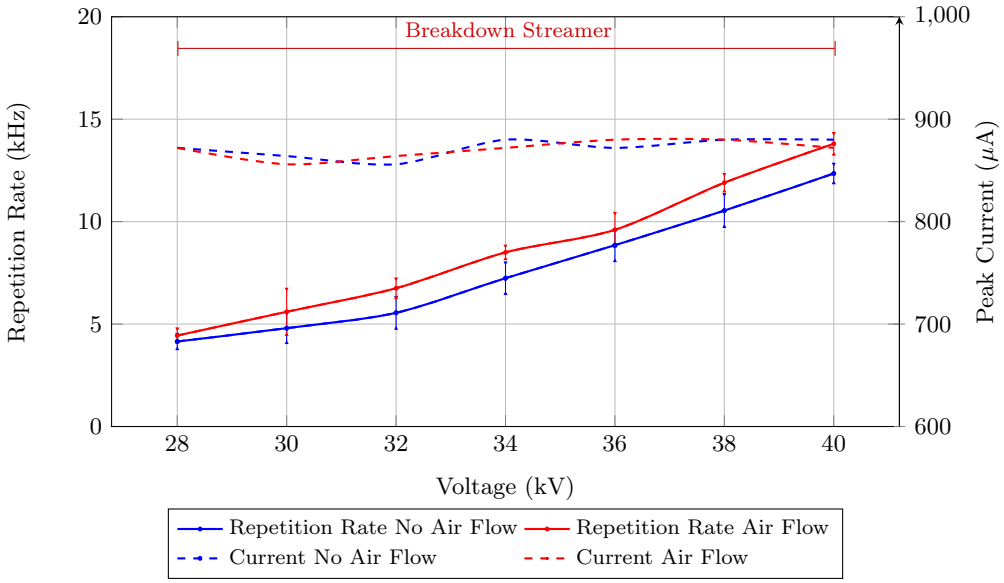

Figure 4.8: Repetition Rate and Average Peak Current

The repetition rate of the pulses were higher than that of the point plane experiment, both due to the higher electric field, smaller volume of interest and the different mode, breakdown streamers as opposed to onset streamers. The breakdown streamer extends further into the gap. The results were more consistent with the expected theory as the repetition rate increased under air flow conditions. The air flow altered the space charge and allowed a faster recovery of the electric field producing a higher repetition rate. The average peak current indicates that the discharge mechanism remains unchanged due to the similar values under both no airflow and airflow conditions. The slow airflow could only affect the movement of space charge and hence only the repetition rate.

This did not necessarily mean that the hypothesis was yet incorrect as the volume of interest was far smaller than the point plane experiment.

4.2.3 Negative Corona

The purpose of the negative corona experiment is to confirm some of the conclusions in Chapter 3 regarding negative corona including:

- An increase in voltage would cause an increase
- An change in airflow would change the repetition rate
- Singlet oxygen has no influence on the repetition rate

The negative needle plane experiment was set up as shown in Figure 4.9 where the gap length was 9.5 cm with a needle tip radius of 0.1 mm. A vacuum pump was applied to one end of the configuration to move air out of the system at a rate of 2.5 m.s^{-1}. As the negative corona is less inconsistent than positive corona, the tests were performed and repeated under various conditions. The tests were performed at an altitude of 1700 m at the High Voltage laboratory at the University of the Witwatersrand.

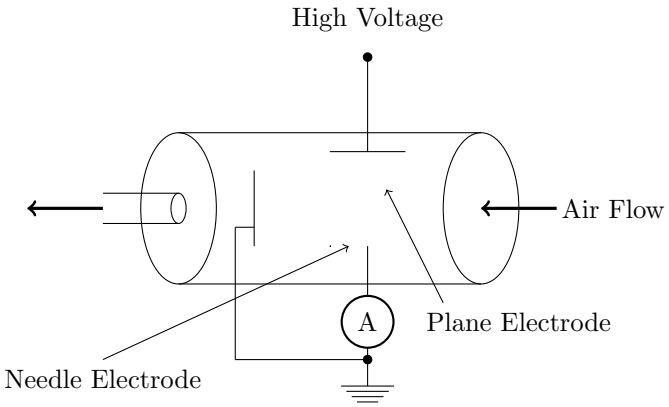

Figure 4.9: Negative Needle Plane Experiment

The repetition rate was an average of the minimum and maximum observed repetition rate in a set sample time and the average peak current was the peak current of an average of 256 samples.

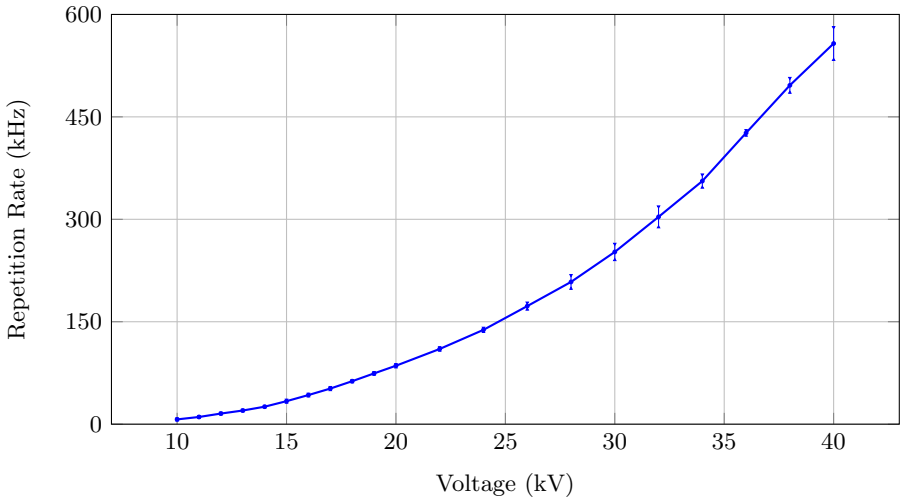

Figure 4.10: Trichel Pulse Repetition Rate

The results in Figure 4.10 illustrate that the repetition rate of the Trichel pulses increased with applied voltage. It was shown that the Trichel pulse consistently increased with applied voltage, due to the sharper electric field. Negative corona was dependent on secondary emissions from the cathode which replenished electrons into the system and as such was more consistent that positive corona. The negative space charge reduced the electric field at the conductor to below its initial value and the repetition rate of the Trichel pulse was determined by the rate of removal of the negative space charge produced during the pulse. It should be noted that the volume for the discharge was small and the space charge developed away from this volume would also influence the electric field and the Trichel pulse mechanism.

The trend of increasing repetition rate in Chapter 3 is confirmed, where it is evident that the movement of the ions is the most critical component of the repetition rate.

The influence of the negative space charge alters the electric field. The space charge is predominantly negative away from the cathode and positive closer to the cathode and has the effect of increasing the electric field sharply near

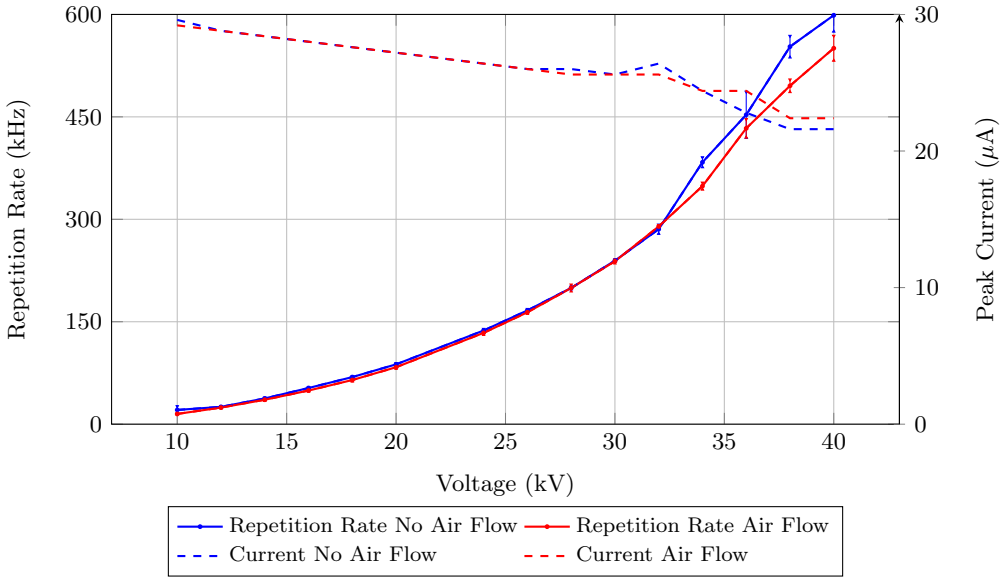

Figure 4.11: Repetition Rate and Peak Amplitudes of Trichel Pulses

the cathode and collapsing it further away. The air flow is a sink for these negative ions, it will lower the sharpness of the electric field closer to the conductor and decrease the repetition rate, but this is not expected to change the discharge mechanism itself and this is confirmed by the measurement of similar average peak currents for both no airflow and airflow conditions. The average peak current decreases with applied voltage and is consistent with the theory as the volume of interest changes depending on the sharpness of the electric field. This is consistent with the work done by Nygaard [64].

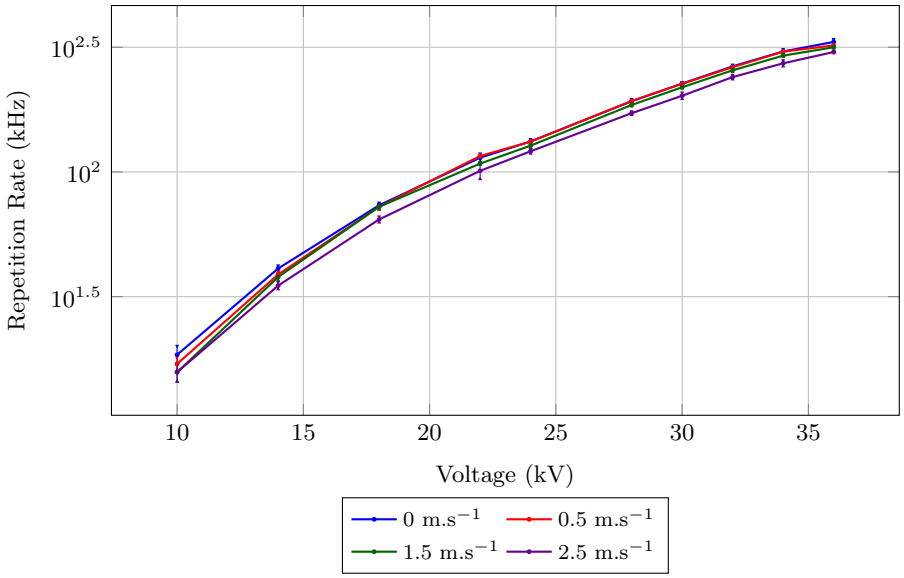

Figure 4.12: Repetition Rate against Applied Voltage for Different Air Flow Speeds

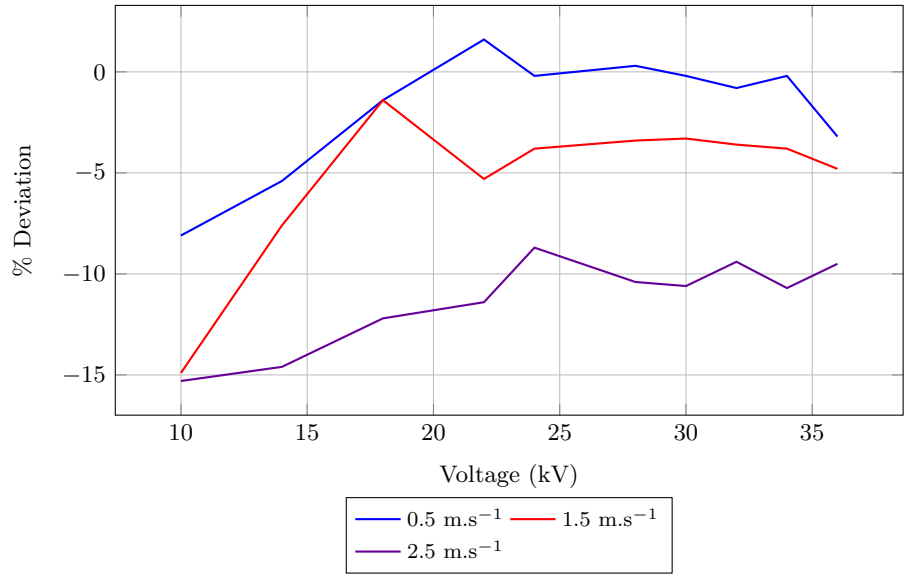

Figure 4.13: Percentage Deviation of Repetition Rate from the no Air Flow Repetition Rate

Figures 4.12 and 4.13 illustrate that the experiment was repeatable for different air flow speeds and that the percentage deviation increases with increasing air flow speeds as expected. Chapter 3 illustrated that the flow rate would alter the space charge and the repetition rate of Trichel streamers.

4.2.4 Energy and Power

As the characteristics of positive and negative corona differ significantly, relating the energy to the peak and repetition rate and determining an average power is the proposed method to compare positive and negative corona. The rate of loss of electrical energy at any point in the electrode space is given by [68]:

$$W = \vec{E}.\vec{J} \tag{4.4}$$

As the circuit solution accounts for the space charge in determining the circuit current, the energy lost can be calculated from the measured current by determining the area under the square of the current or integrating the square of the current.

$$W_{loss} = \int_{t_1}^{t_2} v(t)i(t)dt \tag{4.5}$$

$$= \int_{t_1}^{t_2} i(t)^2 R dt \tag{4.6}$$

Figure 4.14 illustrates the measured corona pulses for the needle plane experiment and states the double exponential functions given earlier. It is evident that the energy of the positive breakdown streamer pulse is far larger than the Trichel pulse as the positive breakdown streamer extends spatially further into the gap than the Trichel pulse.

For energy for a single positive onset or breakdown streamer corona pulse is given by:

$$\begin{aligned} W_{loss} &= \int_0^{250} (2.335 i_p (e^{-0.01t} - e^{-0.0345t}))^2 \times 1 k dt \\ &= 5452 i_p^2 [-50 e^{-0.02t} + 44.94 e^{-0.0445t} - 14.49 e^{-0.069t}]|_0^{250} + K \\ &= 105 \times 10^3 i_p^2 + K \end{aligned} \tag{4.7}$$

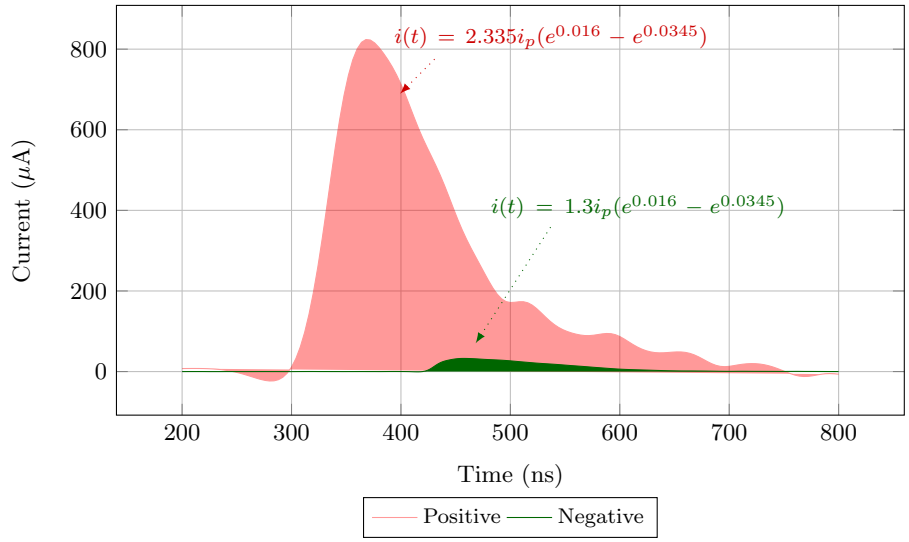

Figure 4.14: Negative and Positive Corona Pulses

Similarly for negative corona, the energy of a single Trichel pulse is given by:

$$\begin{aligned} W_{loss} &= \int_0^{100} (1.3i_p(e^{-0.019t} - e^{-0.285t}))^2 \times 1kdt \\ &= 1690i_p^2[-26.32e^{-0.038t} + 6.58e^{-0.304t} - 1.75e^{-0.57t}]|_0^{100} \\ &= 35 \times 10^3 i_p^2 + K \end{aligned} \tag{4.8}$$

In both cases the constant K in the integral reveals a misleading perception of energy. This value of K would be applicable in the case of a dc current such as positive or negative glow.

Noting that the breakdown streamers and Trichel pulses are periodic with a period T related to the repetition rate f, it may be more useful to look at the average signal power given by:

$$P_{ave} = \frac{1}{T}\int_0^T i(t)^2 R dt \tag{4.9}$$

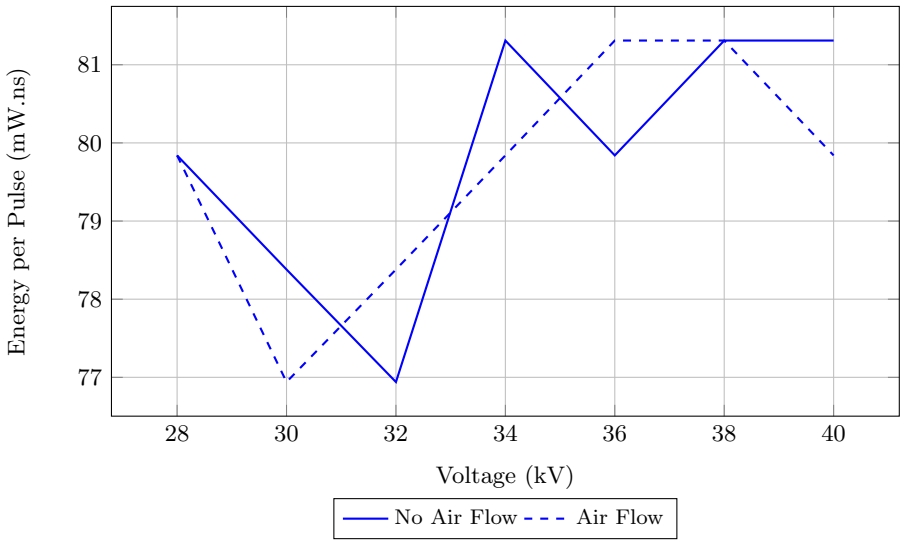

Figure 4.15: Energy per Pulse for Positive Needle Plane Corona

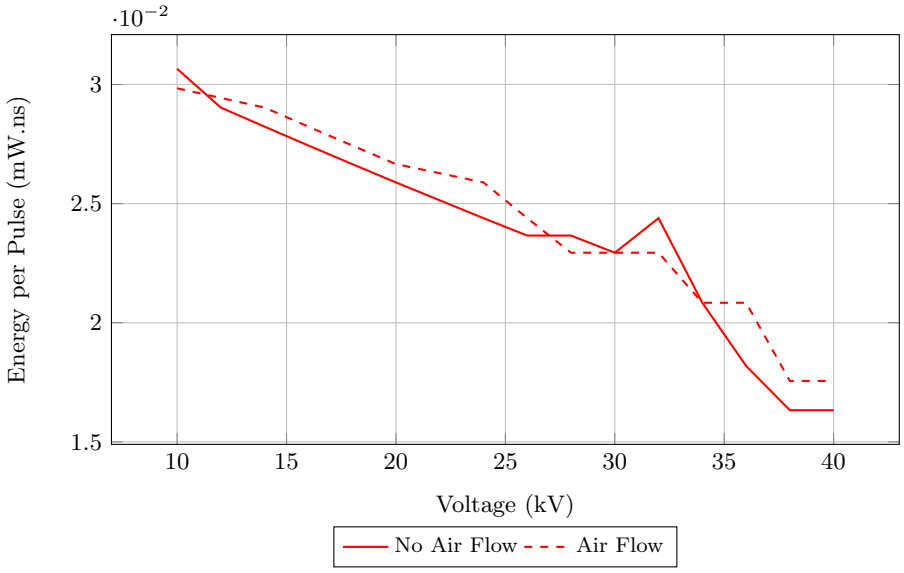

Figure 4.16: Energy per Pulse for Negative Needle Plane Corona

Figures 4.15 and 4.16 illustrate the energy per corona pulse. It is seen that the negative pulse has far less energy than the positive pulse. The positive corona pulse is highly inconsistent, this is due to the nature of positive corona, while the negative pulse is consistent and decreases in energy with an increasing voltage. This is again consistent with the theory of negative corona. The differences between no air flow and air flow per pulse are negligible.

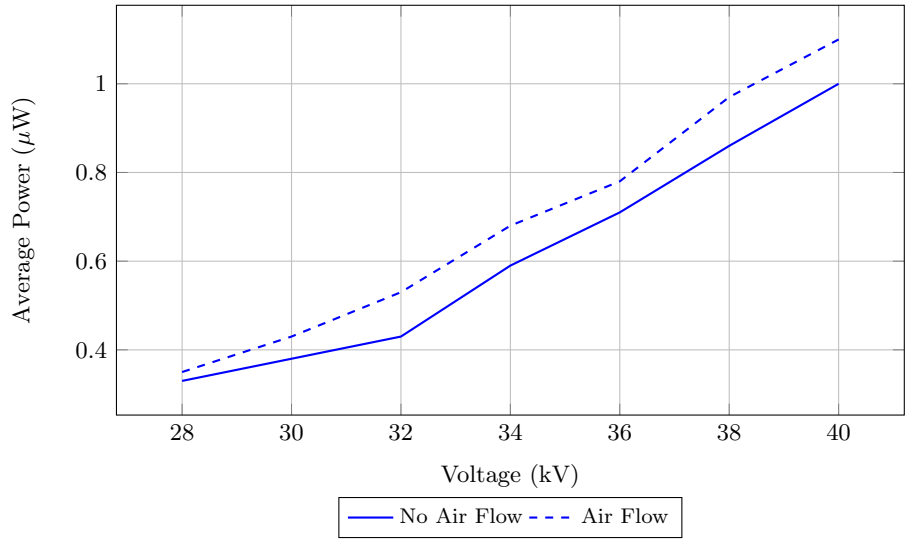

Figure 4.17: Average Power for Positive Needle Plane Corona

Figures 4.17 and 4.18 illustrate the average power of positive and negative corona for the needle plane gap respectively, which is a more appropriate measure than the energy per pulse. It can be seen that an increasing voltage leads to an increasing power loss which is expected. The difference between the positive and negative is substantial and is related to the streamer process in each mechanism. Negative corona is limited to close to the electrode, while positive corona extends further into the gap allowing a larger amount of ionisation to occur. There is only a minor difference between the air flow and no air flow states for negative corona, again this is due to the limitation of the ionisation activity close to the electrode, while the positive corona displays

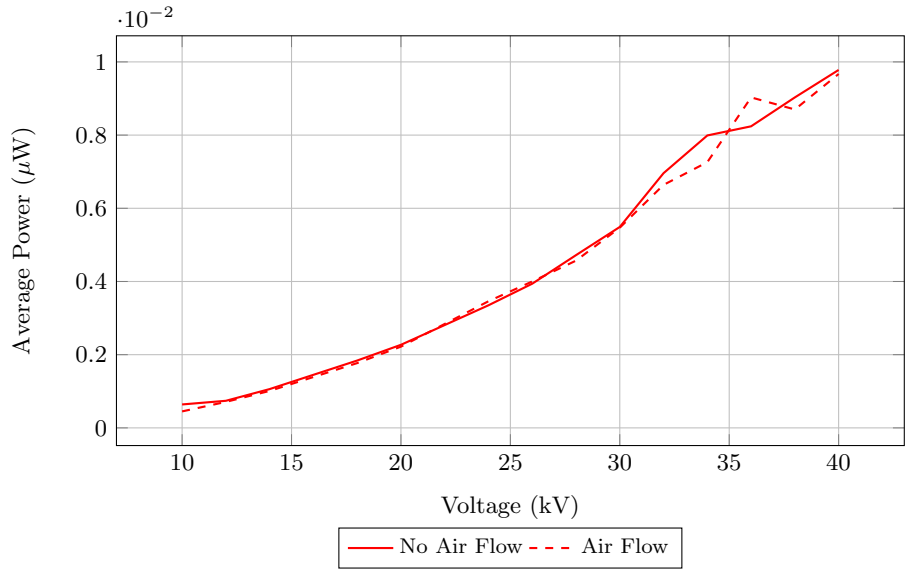

Figure 4.18: Average Power for Negative Needle Plane Corona

consistently higher power loss under air flow condition, which is consistent with the theory that the field recovers faster under air flow conditions.

4.3 Detection of Singlet Oxygen

The airflow experiment illustrated a significant change in the repetition rate of positive onset streamers due to air flow and the model presented in Chapter 3 indicated that singlet oxygen exists with densities of up to 8.5×10^{12} $\text{cm}^{-3}.\text{s}^{-1}$ in the small gap presented. Although the density would differ in the configuration used for the experiments, it was critical to be aware that it exists and was possibly detectable. The detection of singlet oxygen would mean that a relationship between singlet oxygen and the repetition rate of positive onset streamers could be drawn. Should an increase in repetition rate be related to the level of singlet oxygen, the hypothesis would be validated.

The emission of photons due to singlet oxygen collisions occur due to the transition from singlet state to ground state or due to the dimol emission given by [18]:

$$O_2 + O_2(a^1\Delta_g) = 2O_2 + h\nu_{(1270nm)}$$

$$O_2(a^1\Delta_g) + O_2(a^1\Delta_g) = 2O_2 + h\nu_{(634nm)}$$

Grum and Costa investigated the spectral emission of corona by producing a continuous arc and measuring the emissions with an absolute spectrofluorimeter [69]. The emission results were produced three different emission plots [69]:

- 200-500 nm, which is the dominant region of emission with peaks occur at 337 nm and 358 nm due to transitions of nitrogen. This region of emissions have since been used as a basis for investigating high voltage equipment [70].
- 400-600 nm, where the peaks around 400 nm are around 12.5% of the peaks in the UV region.
- 600-900 nm, where the emissions are the lowest. There is activity around the 630-650 nm region, however there is no distinct peak in the

region and this informed the decision to measure 1270 nm.

The 1270 nm emission in the corona process was investigated with the use of a G8376 series InGaAs pin photodiode from Hamamatsu as a detector. The photodiode has a low dark current, low noise, fast response and high cut off frequency [71]. Importantly the photosensitivity of the photodiode lies in the range of 900 nm to 1700 nm, with a peak at 1 550 nm, making it the optimal diode to detect the photo luminescence of 1270 nm of singlet oxygen. As the only expected emission from corona in this region is from singlet oxygen (Table 2.2), the use of a filter is deemed unnecessary. The use of the photodiode over a photomultiplier tube was due to the saturation of the latter in the presence of an electric field.

The emission from singlet oxygen was expected to be very low as illustrated by the modelling and the C4195-03 pre-amplifier is used to boost the signal [72]. The pre-amplifier has a bandwidth of 15 kHz [72]. Due to the slow reaction rate between singlet oxygen and the neutral this was deemed to be sufficient, as the expected response was a low frequency.

The experiment was setup as illustrated in Figure 4.19 where a lens was used to focus the scattered emissions onto the photodiode. The measurement system was calibrated as shown in Appendix F. As the measurement system was trying to measure the emissions in relation to a corona pulse, the electrical and optical measurement systems were coupled to the same reference point as the collapsing electric field would couple to the system. The detector was shielded with twin axial cable and a Faraday cage around the amplifier.

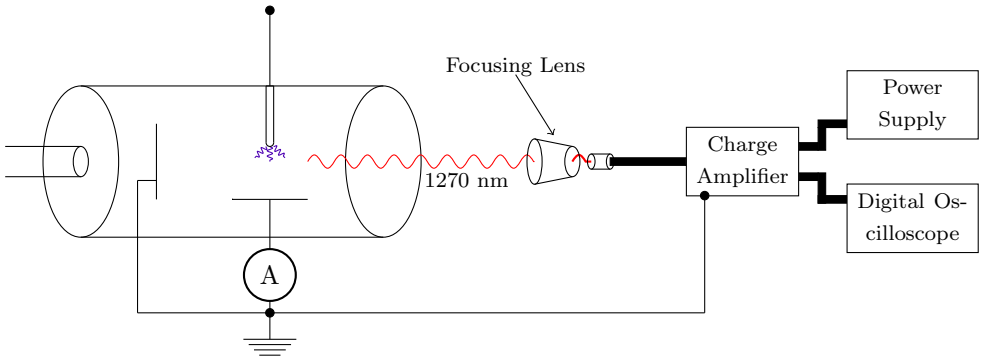

Figure 4.19: Infrared Detection Experiment

Figure 4.20 illustrates the optical emissions of the point plane gap in the visible region, where the extension of the onset streamers was approximately 1 cm from the anode surface. The infrared measurement system produced no detectable emissions from singlet oxygen, which could have been due to the weak emissions or due to detector sensitivity. The long lifetime of singlet oxygen does not assist with detection even if the densities are high. It has been noted that detection of singlet oxygen has been a difficult measurement to make in numerous fields including chemical and medical fields where photomultiplier tubes have been used to detect it [73, 74].

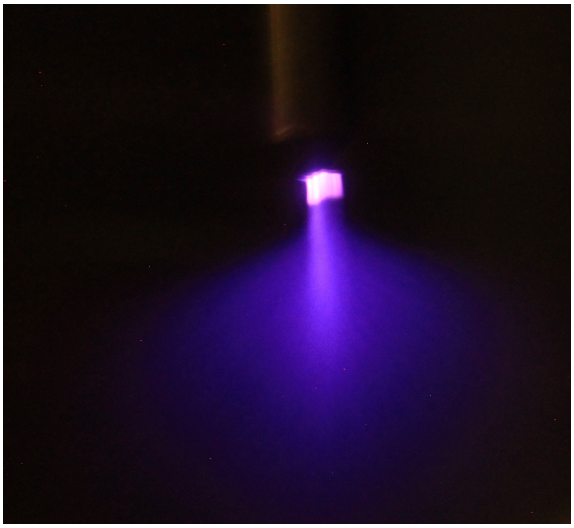

Figure 4.20: Onset Streamer

To further investigate whether there was a detectable presence of singlet oxygen, six needle electrodes were arranged in a circle of radius 2.5 cm and with a gap of 2.5 cm between the tip of the needles and the cathode was used to produce a large amount of positive corona and singlet oxygen. Figure 4.21 illustrates that the visible corona produced by the experiment was greater than that for the single point. Considering the configuration and the results from Chapter 3, there should be sufficient singlet oxygen generated and there should have be emissions at 1270 nm. Again, however, the optical measurement system did not detect any emissions from the singlet oxygen.

Figure 4.21: Breakdown Streamer

4.4 Chemical Production of Singlet Oxygen

The airflow experiment illustrated a significant change in the repetition rate of positive onset streamers due to airflow. If this was due to the removal of singlet oxygen, saturating the test vessel with singlet oxygen would have indicated a similar change repetition rate. To achieve this a simple experiment was conducted, but there were a number of issues.

Kearns stated that decomposition reaction of H_2O_2 with $NaOCl$ is a good source of singlet oxygen [18]. This is achieved through the reaction of common household bleach and hydrogen peroxide resulting in singlet oxygen, salt and water. The chemical reaction is given by:

$$H_2O_2 + NaClO \rightarrow O_2(a^1\Delta_g) + NaCl + H_2O \tag{4.10}$$

An experiment was setup with a sealed container made of perspex with an outer diameter of 10 cm and an infeed of 5 cm in length from the mixing vessel for the emitted gas as shown in Figure 4.22. The gap between the point electrode of radius 2.5 mm and the plane electrode was 10 cm. The quantities used in the experiment were 100 ml 3.5% $NaClO$ and 20 ml 20% H_2O_2 which results in a total of 0.047 mol of $O_2(a^1\Delta_g)$ for a complete reaction. Using the ideal gas law the number of oxygen mols in the container was 0.00579 mol[1] and as such the experiment would alter the amount of singlet oxygen and ultimately the ratio of nitrogen to oxygen in the container.

The expected result was a temporary increase in corona pulse repetition rate, however there would also be a slight increase in partial pressure of oxygen in the system. The production of electrons depends upon the reaction of negative ions and singlet oxygen. The experiment showed no influence on the repetition rate due to the low levels of singlet oxygen produced (the reaction was slow). The largest issues of this experiment were that there was no way to determine the level of singlet oxygen reaching the electrode as well

[1] A pressure of 83 kPa for high altitude, a temperate of 25°C and a volume of 785 cm^3 for the container were used

as the change in the percentage of oxygen, as such a more direct approach in the next section was proposed and undertaken.

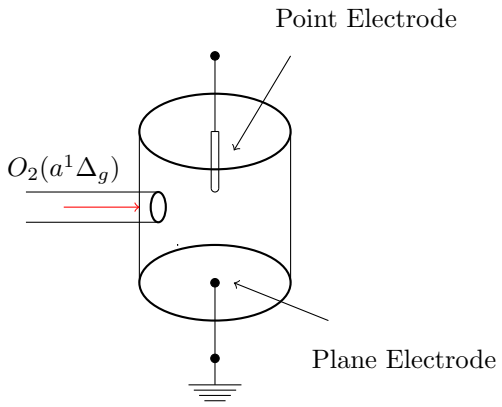

Figure 4.22: Production of Singlet Oxygen

4.5 Laser Production of Singlet Oxygen

The airflow experiment illustrated a significant change in repetition rate of positive onset streamers due to airflow. This change of repetition rate could have been due to a small shift in the space charge or due to the removal of singlet oxygen. The aim of the experiment was to determine if the excitation of oxygen through a laser of a wavelength 1064 nm, which was used to isolate the excitation of singlet oxygen, would influence the repetition rate of positive onset streamers. The experiment was considered a more appropriate experiment than the chemical production as it was more controllable. The experiment would indicate the influence of singlet oxygen only as there should be no effect on the space charge due to the wavelength of laser. Observing the changes in waveform and repetition rate of the positive onset streamers would indicate that the higher density of singlet oxygen has an influence on the production of seed electrons.

The Beer-Lambert law is a useful concept to explain laser induced excitation as it relates the absorption capabilities of the material to the light and is given by [75]:

$$I = I_0 \exp\left(-\sigma N x\right) \tag{4.11}$$

Where:

I = Incident intensity of emission
I_0 = Transmitted intensity of emission
σ = Absorption cross-section of material
N = Number density of the neutral
x = Thickness of material

Applying the Beer-Lambert law for absorption at 1.27 μm and 1.06 μm with peak cross sections of 2.52 $\times 10^{-26}$ and 0.717 $\times 10^{-26}$ cm^2.molecule^{-1} for a mixture of 21% O_2 and 79% N_2 at 20 $^\circ$ and at an altitude of 1400 m; the intensity after 1 cm is $0.59I_0$ and $0.86I_0$ for 1.27 μm and 1.06 μm respectively [76].

Jockusch et al have shown that oxygen is directly excitable through the use of an Nd:YAG laser with a wavelength of 1064 nm [73]. The photo absorption of liquid oxygen is illustrated in Figure 4.23 with the expected excitation and emission processes listed below.

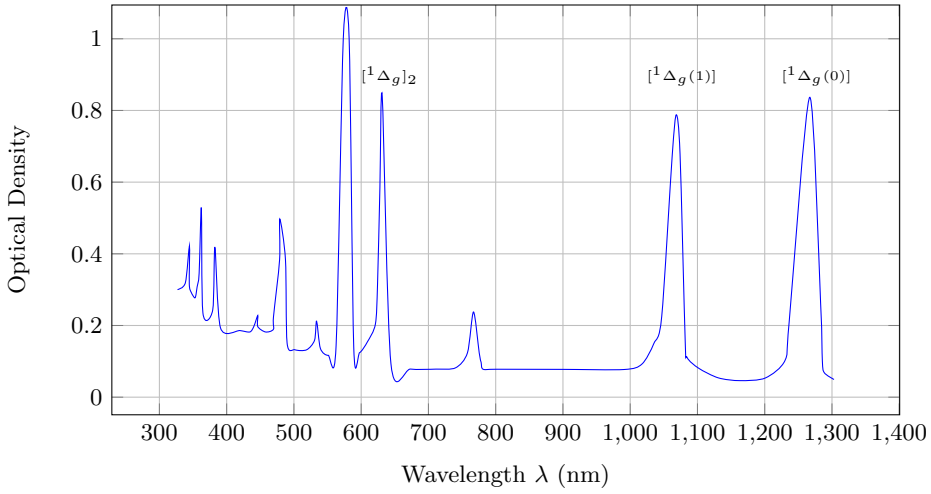

Figure 4.23: Absorption of Oxygen

The expected photo physical states due to excitation are listed [73]:

$$\left[^3\Sigma_g^-(\nu=0)\right] + h\nu_{1064nm} \quad \rightarrow \quad [^1\Delta_g(\nu=1)]$$

The expected emission processes related to singlet oxygen includes [73]:

$$\begin{aligned}
[^1\Delta_g(\nu=1)] &\rightarrow [^1\Delta_g(\nu=0)] + \text{heat} \\
[^1\Delta_g(\nu=0)] &\rightarrow \left[^3\Sigma_g^-(\nu=0)\right] + h\nu_{1270nm} \\
[^1\Delta_g(\nu=0)] &\rightarrow \left[^3\Sigma_g^-(\nu=0)\right] + \text{heat} \\
[^1\Delta_g(\nu=0)] + [^1\Delta_g(\nu=0)] &\rightarrow [^1\Delta_g(\nu=0)]_2 \\
[^1\Delta_g(\nu=0)]_2 &\rightarrow 2\left[^3\Sigma_g^-(\nu=0)\right] + h\nu_{635nm} \\
[^1\Delta_g(\nu=0)]_2 &\rightarrow \left[^3\Sigma_g^-(\nu=0)\right] + \left[^3\Sigma_g^-(\nu=1)\right] + h\nu_{704nm}
\end{aligned}$$

The difference between this experiment and that by Jockusch was that the air in the experiment is at a much higher temperature 293 K (or 20 °C) compared to 77 K and at a much lower pressure. Referring to the Beer-Lambert law the higher the number density N the more photons are absorbed; as such the excitation of singlet oxygen in this experiment would be far less, however the high energy and the constant firing of the laser into a large system was expected to excite the oxygen to a sufficient number density to influence the repetition rate.

The experiment was setup as shown in the Figures 4.24 and 4.25 and involves a point plane setup with the laser passing through the air at a distance of 2 cm from the anode.

The Nd:YAG laser with a wavelength of 1064 nm was used and had the following characteristics for the experiment:

- 10 Hz pulse frequency
- 10-20 ns pulse width
- Unfocused beam diameter 1 cm
- Pulse energy 118 mJ or 800 mJ

The tests were performed at an altitude of 1400 m at the CSIR National Laser Centre in Pretoria.

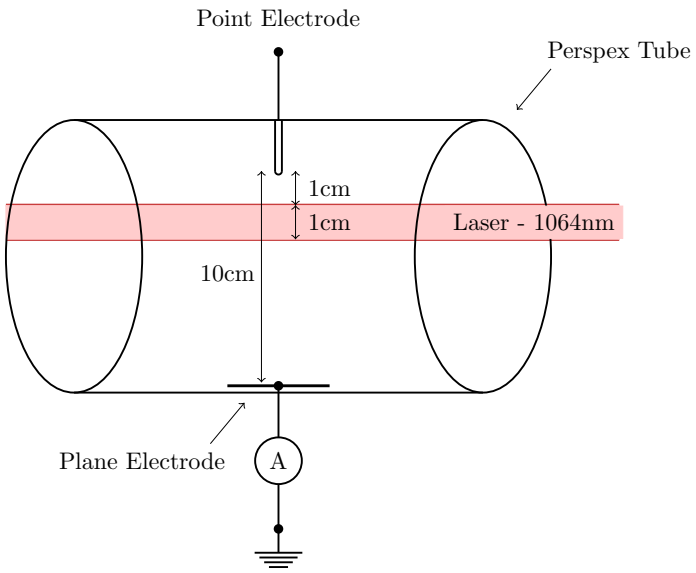

Figure 4.24: Experiment - Side View

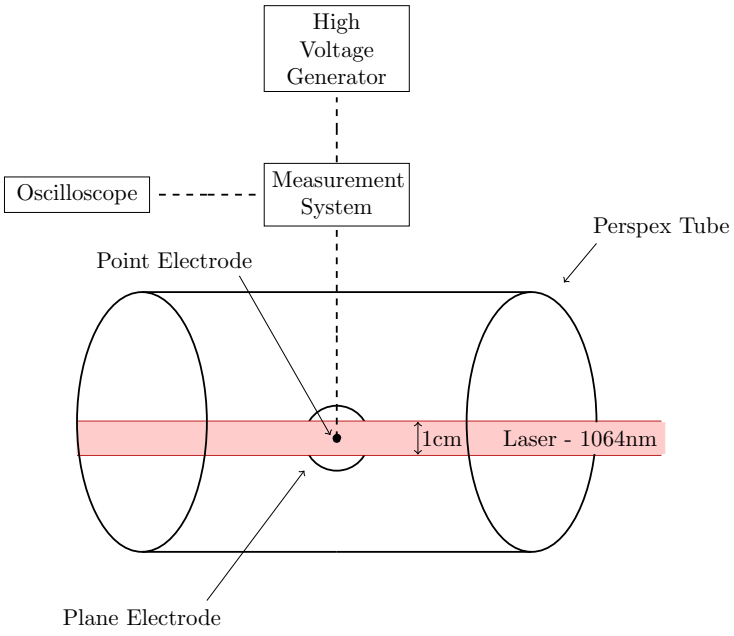

Figure 4.25: Experiment - Top View

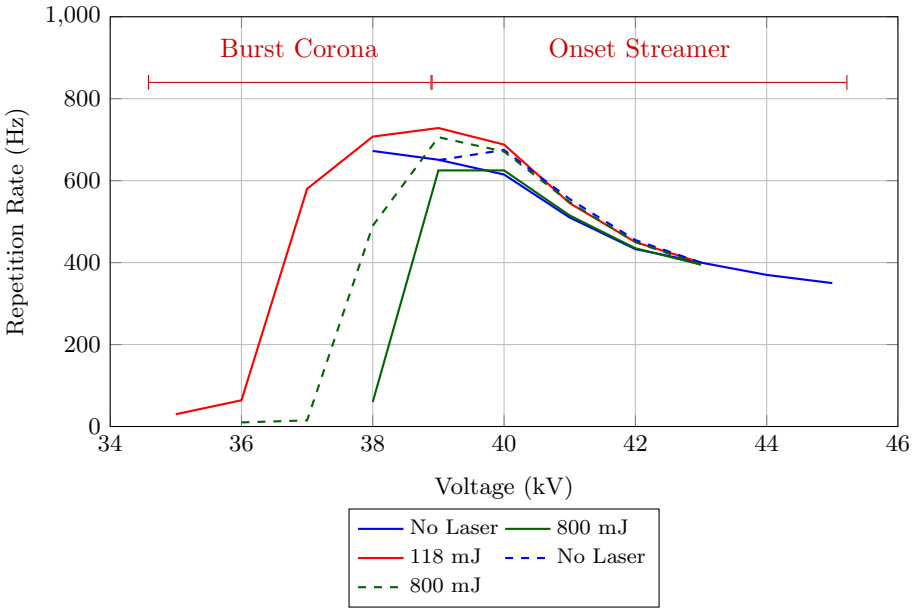

Figure 4.26: Positive Onset Streamer for Direct Excited Oxygen

The repetition rate for positive onset streamers under normal conditions and for when the laser was fired in at 118 mJ and 800 mJ are illustrated in Figure 4.26. There are some differences at lower applied voltages, but tend to converge from 40 kV. Below 40 kV it was difficult to define the corona as onset streamers as it was inconsistent and it has been defined as burst corona. It is not evident that any singlet oxygen produced had an influence on the repetition rate of corona. The modelling illustrated that the singlet oxygen and negative ions produce high densities close to the anode, but are not produced further away where the reaction between negative ions and singlet oxygen does occur but is significantly less (Figure 3.21). It is felt by the author that the lack of negative ions in the region as shown by the modelling is critical, it is also evident that in the region where there are high densities of both negative ions and singlet oxygen, the ionisation, attachment and photoionisation mechanisms would be dominant.

4.6 Discussion

The mechanism of the corona is influenced by the movement of positive and negative space charge and the behaviour of the electric field due to this space charge. For the corona to be sustainable and repetitive over time there needs to be a source of electrons to initiate the subsequent discharges. Together this gives corona its different modes under positive and negative applied voltages.

The initial experiment was done to investigate the movement of space charge under airflow conditions but the positive corona experiment showed an interesting result for positive onset streamers, where the repetition rate changed significantly when there was airflow, it was hypothesised that the slow moving air removed singlet oxygen, which may have been a source of secondary electrons due to the reaction of negative ions and singlet oxygen. Chapter 3 illustrated that the negative ion and singlet oxygen do exist in a region where there could be some influence. The airflow experiment was repeated for different modes of positive and negative corona with the emphasis on the repetition rate and average peak currents. The currents would indicate if the airflow was influence the discharge mechanism and the repetition rate would indicate whether the airflow was influencing the secondary mechanisms.

Positive corona illustrated an inconsistency with theory when airflow was applied where the peak currents are similar and the repetition rate deviates for positive onset streamers, which lent credibility to the hypothesis. Chapter 3 indicated that both negative ions and singlet oxygen exist in the region. The extent to which this was influential is the question.

Negative corona illustrated consistency with theory, published data and the conclusions drawn in Chapter 3 where the there was a general increase in repetition rate of negative Trichel pulses under airflow conditions. This was due to the small shift in space charge, and not the singlet oxygen that was hypothesised for positive onset streamers, as the change was relatively small in comparison. Chapter 3 illustrated that the region where the reaction be-

tween negative ions and singlet oxygen is outside of the critical field region and the production of secondary electrons would be dominated by the ion bombardment of the cathode.

Singlet oxygen emits at 1270 nm due to the transition from the singlet state to ground state and at 634 nm due to the dimol emission. In order to isolate the presence of singlet oxygen, a detection system using an InGaAs photodiode to measure the 1270 nm was developed. The detection of singlet oxygen through the use of a InGaAs photodiode did not detect any emission due to the low emissions at 1270 nm and the sensitivity of the photodiode.

The reaction between negative ions and singlet oxygen may be responsible for the production of seed electrons following the recovery of the electric field in the discharge process and by directly changing one of the densities the electron production rate would change. The direct production of singlet oxygen through Nd:YAG laser with a wavelength of 1064 nm was the most appropriate method of identifying if there was any influence, as it influenced only the singlet oxygen without affecting any other discharge or environmental aspects. The experiment illustrated that the repetition rate and peak of the positive onset streamers were not affected by laser excitation and it can be inferred that the singlet oxygen does not affect the onset streamers.

Chapter 5

Conclusions and Recommendations

The theory behind gas discharges and corona in air indicates that there are multiple excited states of its constituents. These excited states do play a role in the process, particularly where the energy of photons emitted from the excited molecules is high. The role of singlet oxygen was less well understood due to its low energy level and its secondary role of contributing to the production of seed electrons.

The modelling of corona indicated that the role of the movement of ions in the collapse and recovery of the field for both positive and negative corona is the critical component of the pulse formation and duration. The modelling of Trichel pulses indicated that the period between pulses is influenced by the clearing of space charge. The model illustrated that there is a presence of singlet oxygen in both negative and positive discharges, however the role it plays may be insignificant to that of the space charge as the production of secondary electrons is dependent on the reaction of negative ions and singlet oxygen. In the case of negative corona, electrons would be produced in a region where they would not be influential and in positive corona the procession is low in the region where they would be influential.

The experiments investigated the role of singlet oxygen in the environment of the corona and illustrated that it is not a contributing factor to the corona discharge. This is inferred from the fact that:

- The airflow influenced the removal of space charge and altered the repetition rate as expected, with the exception of positive onset streamers. however the mode is pushed towards that of positive glow.
- The emission from singlet oxygen at 1270 nm was not detectable, both due to the low emission from singlet oxygen and sensitivity of the photodiode.
- The repetition rate does not change when oxygen is directly excited in the system through the use of a laser.

It is concluded that singlet oxygen plays no distinguishable role in the repetition rate of positive corona in this thesis and the hypothesis that singlet oxygen is the major factor responsible for the production of seed electrons in positive corona is invalid.

5.0.1 Recommendations

The following recommendations are made

- A full three dimensional model of corona be applied to fully understand the collapse of the electric field, the 1.5 dimensional is useful, however a number of assumptions are made.
- The metastable state of singlet oxygen has a relatively long lifetime and as such has significantly low emissions and InGaAs photodiodes are not sensitive enough for detection. A photomultiplier tube would be more suitable for measurement, should the issues of saturation due to the high electric fields be overcome.

References

[1] J. Lowke. "Theory of electrical breakdown in air - the role of metastable oxygen molecules." *Journal of Physics D: Applied Physics*, vol. 25, 1992.

[2] J. Lowke and R. Morrow. "Theory of electric corona including the role of plasma chemistry." *Pure and Applied Chemistry*, vol. 66, no. 6, 1994.

[3] R. Morrow. "The theory of positive glow corona." *Journal of Physics D: Applied Physics*, vol. 30, 1997.

[4] E. Kuffel, W. Zaengl, and J. Kuffel. *High Voltage Engineering: Fundamentals*. Newnes, second ed., 2000.

[5] J. Kraus. *Electromagnetics*. McGraw-Hill, Inc, fourth ed., 1991.

[6] Y. Itikawa, M. Hayashi, A. Ichimura, K. Onda, K. Sakimoto, and K. Takayanagi. "Cross Sections for Collisions of Electrons and Photons with Nitrogen Molecules." *Journal of Physical Chemistry*, vol. 15, no. 3, 1986.

[7] Y. Itikawa. "Cross Sections for Electron Collisions with Nitrogen Molecules." *Journal of Physical Chemistry*, vol. 35, no. 1, 2006.

[8] A. Phelps and L. Pitchford. "Anisotropic scattering of electrons by N_2 and its effect on electron transport." *Phys. Rev. A*, vol. 31, no. 5, 1985.

[9] Plasma Data Exchange Project. "LXcat." *http://fr.lxcat.net/home/, last accessed June 29, 2015*.

[10] Y. Itikawa, A. Ichimura, K. Onda, K. Sakimoto, and K. Takayanagi. "Cross Sections for Collisions of Electrons and Photons with Oxygen Molecules." *Journal of Physical Chemistry*, vol. 18, no. 1, 1989.

[11] Y. Itikawa. "Cross Sections for Electron Collisions with Oxygen Molecules." *Journal of Physical Chemistry*, vol. 38, no. 1, 2009.

[12] G. Hagelaar and L. Pitchford. "Solving the Boltzmann equation to obtain electron transport coefficients and rate coefficients for fluid models." *Plasma Sources Science and Technology*, vol. 14, 2005.

[13] R. Morrow and J. Lowke. "Streamer propagation in air." *Journal of Physics D: Applied Physics*, vol. 30, 1997.

[14] P. Sarma Maruvada. *Corona Performance of High Voltage Transmission Lines*. Taylor and Francis Group, 2000.

[15] T. Giao and J. Jordan. "Modes of Corona Discharges in Air." *IEEE Transactions on Power Apparatus and Systems*, vol. 87, no. 5, 1968.

[16] G. Trichel. "The Mechanism of the Negative Point to Plane Corona Near Onset." *Phys. Rev. A*, vol. 27, 1938.

[17] W. Lama and C. Gallo. "Systematic study of the electrical characteristics of the Trichel current pulses from negative needle to plane coronas." *Journal of Applied Physics*, vol. 45, 1974.

[18] D. Kearns. "Physical and Chemical Properties of Singlet Oxygen." *Chemical Reviews*, vol. 71, no. 4, 1971.

[19] P. Krupenie. "The Spectrum of Molecular Oxygen." *Journal of Physical Chemistry*, vol. 1, no. 2, 1972.

[20] F. Fehsenfeld, D. Albritton, J. Burt, and H. Schiff. "Associative-detachment reactions of O^- and O_2^- by $O_2(^1\Delta_g)$." *Canadian Journal of Chemistry*, vol. 47, 1969.

[21] A. Phelps. "Laboratory studies of electron attachment and detachment processes of aeronomic interest." *Canadian Journal of Chemistry*, 1969.

[22] S. Belostotsky, D. Economou, D. Lopaev, and T. Rakhimova. "Negative ion destruction by O(^{3}P) atoms and $O_2(a^1\Delta_g)$ molecules in an oxygen plasma." *Plasma Sources Science and Technology*, vol. 14, 2005.

[23] J. Gudmundsson. "Recombination and detachment in oxygen discharges: the role of metastable oxygen molecules." *Journal of Physics D: Applied Physics*, vol. 37, 2004.

[24] R. Franklin. "The role of $O_2(a^1\Delta_g)$ metastables and associative detachment in discharges in oxygen." *Journal of Physics D: Applied Physics*, vol. 34, 2001.

[25] J. Gudmundsson. *Technical report RH-17-2004 - A critical review of the reaction set for a low pressure oxygen processing discharge*. Science Institute, University of Iceland, 2004.

[26] R. McNeal and G. Cook. "Photoionization of O_2 in the metastable $a^1\Delta_g$ State." *Journal of Chemical Physics*, vol. 45, 1966.

[27] I. Clark and R. Wayne. "The absolute cross section for photoionization of $O_2(^1\Delta_g)$." *Molecular Physics*, vol. 18, no. 4, 1970.

[28] S. Ogawa and M. Ogawa. "Absorption Cross Section of $O_2(a^1\Delta_g)$ and $O_2(X^3\Sigma_g^-)$." *Canadian Journal of Physics*, vol. 53, 1975.

[29] C. Birdsall. "Particle-in-Cell Charged Particle Simulations, Plus Monte Carlo Collisions with Neutral Atoms, PIC-MCC." *IEEE Transactions on Plasma Science*, vol. 19, no. 2, 1991.

[30] A. Swanson, M. Grant, and I. Jandrell. "HVDC Corona - Analysis of Corona through Modelling Techniques." *International Symposium on High Voltage Engineering, Seoul, South Korea*, 2013.

[31] C. Soria, F. Pontiga, and A. Castellanos. "Particle-in-Cell Simulation of Electrical Gas Discharges." *Journal of Computational Physics*, vol. 171, 2001.

[32] G. Lapenta, F. Iinoya, and J. Brackbill. "Particle-in-Cell Simulation of Glow Discharges in Complex Geometries." *IEEE Transactions on Plasma Science*, vol. 23, no. 4, 1995.

[33] C. Li and C. Wu. "Three Fluid Transport Models by Particle-in-Cell Method for RF Glow Discharges." *IEEE Transactions on Plasma Science*, vol. 20, no. 6, 1992.

[34] B. Qin, J. Sheng, Z. Yan, and G. Gela. "Accurate Calculation of Ion Flow Field Under HVDC Bipolar Transmission Lines." *IEEE Transactions on Power Delivery*, vol. 3, no. 1, 1988.

[35] M. Surendra and D. Graves. "Particle Simulations of Radio-Frequency Glow Discharges." *IEEE Transactions on Plasma Science*, vol. 19, no. 2, 1991.

[36] V. Vahedi and M. Surendra. "A Monte Carlo collision model for the particle-in-cell method: applications to argon and oxygen discharges." *Computer Physics Communications*, vol. 87, 1995.

[37] R. Morrow. "Numerical Solution of Hyperbolic Equations for Electron Drift in Strongly Non-uniform Electric Fields." *Journal of Computational Physics*, 1981.

[38] R. Morrow and L. Crem. "Flux-Corrected Transport and Diffusion on a Non-uniform Mesh." *Journal of Computational Physics*, 1985.

[39] J. Boris and D. Book. "Flux-corrected transport. I. SHASTA, a fluid transport algorithm that works." *Journal of Computational Physics*, 1973.

[40] R. Morrow. "Theory of negative corona in oxygen." *Phys. Rev. A*, 1985.

[41] J. Shim, S. Choi, H. Hwang, H. Ha, K. Ko, and H. Kang. "2-D Simulation on the corona discharge of negative needle-to-plane electrodes." *IEEE Transactions on Magnetics*, vol. 38, no. 2, 2002.

[42] G. Georghiou, R. Morrow, and A. Metaxas. "An Improved Finite-Element Flux-Corrected Transport Algorithm." *Journal of Computational Physics*, vol. 148, 1999.

[43] G. Georghiou, R. Morrow, and A. Metaxas. "A two-dimensional, finite-element, flux-corrected transport algorithm for the solution of gas discharge problems." *Journal of Physics D: Applied Physics*, vol. 33, 2000.

[44] A. Hallac, G. Georghiou, and A. Metaxas. "Secondary emission effects on streamer branching in transient non-uniform short-gap discharges." *Journal of Physics D: Applied Physics*, vol. 36, 2003.

[45] P. Sattari, C. Gallo, S. Castle, and K. Adamaniak. "Trichel pulse characteristics—negative corona discharge in air." *Journal of Physics D: Applied Physics*, vol. 44, 2011.

[46] F. Deng, L. Ye, and K. Song. "Numerical studies of Trichel pulses in airflows." *Journal of Physics D: Applied Physics*, 2013.

[47] N. Kim, S. Lee, G. Georghiou, D. Kim, and D. Kim. "Accurate Prediction Method of Breakdown Voltage in Air at Atmospheric Pressure." *Journal of Electrical Engineering and Technology*, vol. 7, 2012.

[48] T. Tran, I. Golosnoy, P. Lewin, and G. Georghiou. "Numerical modelling of negative discharges in air with experimental validation." *Journal of Physics D: Applied Physics*, vol. 44, 2011.

[49] Zhuang and Zeng. "A local discontinuous Galerkin method for 1.5-dimensional streamer discharge simulations." *Applied Mathematics and Computation*, vol. 219, 2013.

[50] N. Liu and V. Pasko. "Effects of photoionization on propagation and branching of positive and negative streamers in sprites." *Journal of Geophysical Research*, vol. 109, 2004.

[51] G. Penney and G. Hummert. "Photoionization Measurements in Air, Oxygen and Nitrogen." *Journal of Applied Physics*, vol. 41, no. 2, 1970.

[52] M. Zheleznyak, B. Mnatskanian, and S. Sizykh. "Photoionization of nitrogen and oxygen mixtures by radiation from gas discharge." *High Temperature*, 1982.

[53] A. Kulikovsky. "The role of photoionization in positive streamer dynamics." *Journal of Physics D: Applied Physics*, vol. 33, 2000.

[54] S. Pancheshnyi, S. Starikovskaia, and A. Y. Starikovskii". "Role of photoionization process in propagation of cathode-directed streamer." *Journal of Physics D: Applied Physics*, vol. 34s, 2001.

[55] U. Inan and A. Inan. *Engineering Electromagnetics*. Addison Wesley Longman, Inc, 1999.

[56] Tera Analysis Ltd. *Quickfield User's Guide Version 5.6*. Tera Analysis Ltd, 2009.

[57] A. Davies, C. Evans, and F Llewellyn Jones. "Electrical Breakdown of Gases: The Spatio-Temporal Growth of Ionization in Fields Distorted by Space Charge." *Proceedings of the Royal Society of London - Series A: Mathematical and Physical Sciences*, vol. 281, no. 1385, 1964.

[58] A. Davies. "Discharge Simulation." *IEE Proceedings A*, vol. 133, no. 4, 1986.

[59] J. Cobine. *Gaseous Conductors*. Dover Publications, Inc, 1958.

[60] N. Sato. "Discharge current induced by the motion of charged particles." *Journal of Physics D: Applied Physics*, vol. 13, 1980.

[61] R. Morrow and N. Sato. "The discharge current induced by the motion of charged particles in time-dependent electric fields; Sato's equation extended." *Journal of Physics D: Applied Physics*, vol. 32, 1999.

[62] J. Verboncoeur, M. Alves, V. Vahedi, and C. Birdsall. "Simultaneous Potential and Circuit Solution for 1D Bounded Plasma Particle Simulation Codes." *Journal of Computational Physics*, vol. 104, 1993.

[63] C. Birdsall and A. Langdon. *Plasma Physics via Computer Simulation*. Taylor and Francis Group, 1991.

[64] K. Nygaard. "Frequency of Corona Discharge Trichel Pulses in Air Flows." *Journal of Applied Physics*, vol. 37, no. 7, 1966.

[65] A. Jaworek and A. Krupa. "Corona discharge from a multipoint electrode in flowing air." *Journal of Electrostatics*, vol. 38, 1996.

[66] M. Abdel-Salam, H. Abdallah, S. Abdel-Sattar, and M. Farghally. "Positive Corona in Point-Plane Gaps as Influenced by Wind." *IEEE Transactions on Electrical Insulation*, vol. EI-22, no. 6, 1987.

[67] A. Swanson, M. Grant, I. Hofsajer, and I. Jandrell. "HVDC Corona - Experimental Setup and Measurements." *International Symposium on High Voltage Engineering, Seoul, South Korea*, 2013.

[68] J. Jones. "On corona-induced gas motion and heating I: Field equations, modelling and vortex formation." *Journal of Electrostatics*, vol. 66, 2008.

[69] F. Grum and L. F. Costa. "Spectral emission of corona discharges." *Appl. Opt.*, vol. 15, no. 1, pp. 76–79, Jan 1976. URL `http://ao.osa.org/abstract.cfm?URI=ao-15-1-76`.

[70] W. Vosloo, R. Stolper, and P. Baker. "Daylight Co- rona Discharge Observation and Recording System." *International Symposium on High Voltage Engineering, Quebec, Canada*, 1997.

[71] Hamamatsu. "InGaAs PIN Photodiodes - G8376 Series." *http://www.hamamatsu.com*, last accessed 2013.

[72] Hamamatsu. "Charge Amplifier - C4195-03." *http://www.hamamatsu.com*, last accessed 2013.

[73] S. Jockusch, N. Turro, E. Thompson, M. Gouterman, J. Callis, and G. Khalil. "Singlet molecular oxygen by direct excitation." *The Royal Society of Chemistry: Photochemical and Photobiological Sciences*, 2008.

[74] M. Niedre, M. Patterson, and B. Wilson. "Direct Near-Infrared Luminescence Detection of Singlet Oxygen Generated by Photodynamic Therapy in Cells In Vitro and Tissue In Vitro." *Photochemistry and Photobiology*, vol. 75, 2002.

[75] R. Serway and R. Beichner. *Physics for Scientists and Engineers with Modern Physics*. Saunders College Publishing, fifth ed., 2000.

[76] K. Smith and D. Newham. "Near-infrared absorption cross-sections and integrated absorption intensities of molecular oxygen (O_2, $O_2 - O_2$ and $O_2 - N_2$)." *Journal of Geophysical Research*, vol. 105, no. D6, 2000.

Appendix A

Electric Field Solver

Direct current electric fields are different from alternating current electric fields in that ac fields are changing with respect to time and have the ability to couple voltages and currents in surrounding objects capacitively and inductively, whereas the dc fields are static and have the ability to affect the trajectory of ions and deposition of charged particles on surfaces [1].

A.1 Definition

The magnitude and direction of the force exerted on a stationary electrical charge define an electric field. If an electric charge of one coulomb is in an electric field of one volt per metre, it will be subjected to a force of one newton in the direction of the electric field [1, 2].

A.2 Coulomb's Law and Electric Potential

Coulomb's law is given by [1, 2].

$$\vec{E} = \frac{Q}{4\pi\epsilon R^2}\vec{r} \tag{A.1}$$

Where:
$\vec{E}$ = Electric Field [V.cm^{-1}]
Q = Charge [C]
ϵ_0 = permittivity of free space
R = distance from the charge [cm]

For a line charge where $\rho = Q/l$, Coulomb's law is rewritten as [2]:

$$\vec{E} = \frac{\rho}{4\pi\epsilon R^2}\vec{r} \tag{A.2}$$

The electrostatic potential difference between point a and point b is given by [3]:

$$V_{ab} = -\int_a^b \vec{E}.d\vec{l} = V_a - V_b \tag{A.3}$$

A.3 Poisson's Equation

Gauss' law at a point is given by [3]:

$$\nabla.\vec{D} = \rho \tag{A.4}$$

or

$$\nabla.\vec{E} = \frac{\rho}{\epsilon_0} \tag{A.5}$$

Where:
$\vec{E}$ = Electric field [V.cm^{-1}]
ρ = Space charge [C.cm^{-3}]
ϵ_0 = permittivity of free space

and the electric field is the gradient of the electrostatic potential [3]:

$$\vec{E} = -\nabla\phi \tag{A.6}$$

Poisson's Equation is given by [4, 3, 5]:

$$\nabla^2\phi = -\frac{\rho}{\epsilon_0} \tag{A.7}$$

In cartesian / planar coordinates it is written as:

$$\frac{\partial^2\phi}{\partial x^2} + \frac{\partial^2\phi}{\partial y^2} + \frac{\partial^2\phi}{\partial z^2} = -\frac{\rho}{\epsilon_0} \tag{A.8}$$

In cylindrical coordinates it is written as:

$$\frac{\partial^2\phi}{\partial r^2} + \frac{\partial\phi}{r\partial r} + \frac{\partial^2\phi}{r^2\partial\theta^2} + \frac{\partial^2\phi}{\partial z^2} = -\frac{\rho}{\epsilon_0} \tag{A.9}$$

For charge free space it becomes Laplace's Equation given by [4, 3]

$$\nabla^2\phi = 0 \tag{A.10}$$

A.4 Finite Difference Method

The finite difference method is used to solve elliptic, hyperbolic and parabolic partial differential equations and begins with the expansion of the Taylor series [6, 7]:

$$f(x+h) = f(x) + f'(x)h + \frac{f''(x)}{2!}h^2 \tag{A.11}$$

Retaining the first two terms the forward difference approximation is written as [7]:

$$f'(x) = \frac{f(x+h) - f(x)}{h} \tag{A.12}$$

Considering $-h$ the backward difference approximation is written as [7]:

$$f'(x) = \frac{f(x) - f(x-h)}{h} \tag{A.13}$$

Combining the forward and backward difference approximations, the central

difference approximation of a first order derivative is written as [7]:

$$f'(x) = \frac{1}{2h}[f(x+h) - f(x-h)] \tag{A.14}$$

Similarly retaining the first three terms of the Taylor series, the central difference approximation of a second order derivative [7]:

$$f''(x) = \frac{1}{h^2}[f(x+h) - 2f(x) + f(x-h)] \tag{A.15}$$

A.4.1 Planar Co-ordinates

Applied to cartesian co-ordinates Poisson's equation in one dimension may be written as:

$$\phi(x_{i+1}) - 2\phi(x_i) + \phi(x_{i-1}) = -\Delta x^2 \frac{\rho_i}{\epsilon_0} \tag{A.16}$$

And in two dimensions:

$$\phi(x_{i+1}, y_j) + \phi(x_i, y_{j+1}) - 4\phi(x_i, y_j) + \phi(x_{i-1}, y_j) + \phi(x_i, y_{j-1}) = -\Delta x^2 \frac{\rho_i}{\epsilon_0} \tag{A.17}$$

A.4.2 Cylindrical Co-ordinates

Applied to cylindrical co-ordinates Poisson's equation in one dimension may be rewritten as:

$$\left(1 + \tfrac{\Delta r}{2r_i}\right)\phi(r_{i+1}) - 2\phi(r_i) + \left(1 - \tfrac{\Delta r}{2r_i}\right)\phi(r_{i-1}) = -\Delta r^2 \frac{\rho_i}{\epsilon_0} \tag{A.18}$$

And in two dimensions:

$$\begin{aligned} \left(1 + \tfrac{\Delta r}{2r_i}\right)\phi(r_{i+1}, z_i) + \phi(r_i, z_{j+1}) \;&-\; 4\phi(r_i, z_j) + \left(1 - \tfrac{\Delta r}{2r_i}\right)\phi(r_{i-1}, z_j) + \phi(r_i, z_{j+1}) \\ &= -\Delta r^2 \frac{\rho_{i,j}}{\epsilon_0} \end{aligned} \tag{A.19}$$

A.4.3 Algorithm

An algorithm using the finite difference method to solve for Poisson's equation by dividing the area into n smaller discrete areas, can be used to solve the $(n-1)$ unknowns [8]:

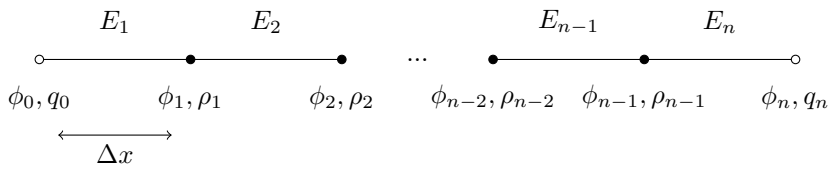

Figure A.1: Finite Difference Method

For nodes 1 to $(n-1)$, an equation is derived leading to $(n-1)$ linear equations

$$\begin{aligned} 1\phi_0 - 2\phi_1 + 1\phi_2 &= -\Delta x^2 \frac{\rho_1}{\varepsilon_0} \\ 1\phi_1 - 2\phi_2 + 1\phi_3 &= -\Delta x^2 \frac{\rho_2}{\varepsilon_0} \\ &\vdots \\ 1\phi_{n-2} - 2\phi_{n-1} + 1\phi_n &= -\Delta x^2 \frac{\rho_2}{\varepsilon_{n-1}} \end{aligned}$$

The nodes at the end are boundary nodes and conditions can be applied here, a Dirichlet boundary condition for a boundary with a set voltage and a Neumann boundary condition for a boundary with a set electric field [7]:

$$\phi_n = v_n \tag{A.20}$$

$$\phi_0 - \phi_1 = \Delta x E_s \tag{A.21}$$

These are written in matrix form and solved simultaneously for voltages, where

$$\begin{bmatrix} 1 & -1 & 0 & \dots & 0 & 0 \\ 1 & -2 & 1 & \dots & 0 & 0 \\ 0 & 1 & -2 & \dots & 0 & 0 \\ \vdots & \vdots & \vdots & \ddots & \vdots & \vdots \\ 0 & 0 & 0 & \dots & -2 & 1 \\ 0 & 0 & 0 & \dots & 0 & 1 \end{bmatrix} \begin{bmatrix} \phi_0 \\ \phi_1 \\ \phi_2 \\ \vdots \\ \phi_{n-1} \\ \phi_n \end{bmatrix} = \begin{bmatrix} \Delta x E_s \\ -\Delta x^2 \frac{\rho_1}{\varepsilon_0} \\ -\Delta x^2 \frac{\rho_2}{\varepsilon_0} \\ \vdots \\ -\Delta x^2 \frac{\rho_n}{\varepsilon_0} \\ v_n \end{bmatrix} \tag{A.22}$$

$$\mathbf{x} = \mathbf{A^{-1}}.\mathbf{b} \tag{A.23}$$

And finally solving for the electric field:

$$E_{i-1/2} = \frac{\phi_n - \phi_{n-1}}{\Delta x} \tag{A.24}$$

References

[1] P. Sarma Maruvada. *Corona Performance of High Voltage Transmission Lines*. Taylor and Francis Group, 2000.

[2] R. Serway and R. Beichner. *Physics for Scientists and Engineers with Modern Physics*. Saunders College Publishing, fifth ed., 2000.

[3] U. Inan and A. Inan. *Engineering Electromagnetics*. Addison Wesley Longman, Inc, 1999.

[4] J. Kraus. *Electromagnetics*. McGraw-Hill, Inc, fourth ed., 1991.

[5] Tera Analysis Ltd. *Quickfield User's Guide Version 5.6*. Tera Analysis Ltd, 2009.

[6] G. James. *Advanced Modern Engineering Mathematics*. Prentice Hall, second ed., 1999.

[7] S. Farlow. *Partial Differential Equations for Scientists and Engineers*. Dover Publications, Inc, first ed., 1993.

[8] J. Nagel. "Solving the Generalized Poisson Equation Using the Finite-Difference Method (FDM)." *Article for IEEE Antennas and Propagation Society, http://www.ieeeaps.org*, 2011.

Appendix B

Coupled Circuit Solution

B.1 Coupling Capacitor Measurement Circuit

The circuit in Figure B.1 is used for measurement as it contains a coupling capacitor apart from the impedance of the source and includes inductance, as the physical measurement system has a large inductive loop [1]. To compare measurement to the numerical model, the circuit is solved as follows.

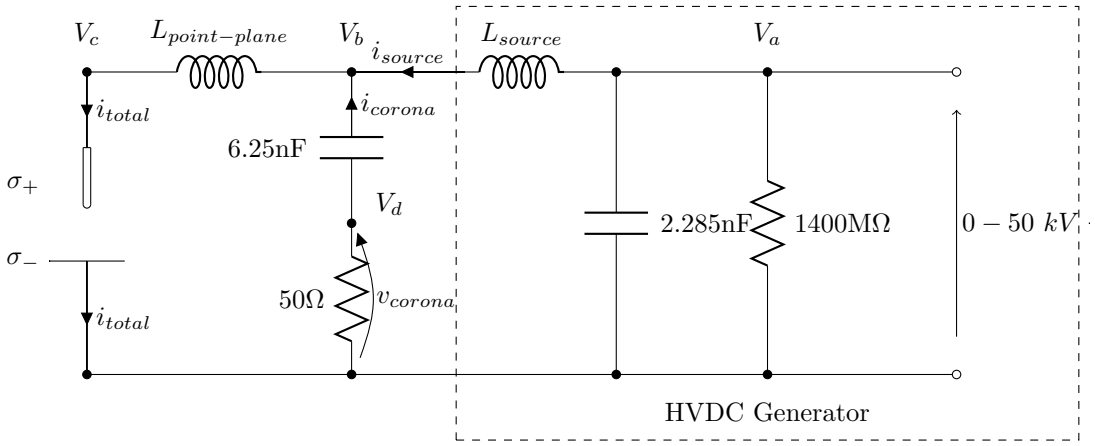

Figure B.1: Circuit with Coupling Capacitor Measurement

The circuit is solved through nodal analysis for voltages at node A and B respectively:

$$\frac{V_a}{R_1} + C_1\frac{dV_a}{dt} + \frac{1}{L_1}\int (V_a - V_b)dt = 0 \tag{B.1}$$

$$\frac{1}{L_1}\int (V_b - V_a)dt + \frac{1}{L_2}\int (V_b - V_c)dt + C_2\frac{d(V_b - V_d)}{dt} = 0 \tag{B.2}$$

In this instance it is assumed that the corona pulse is a current source.

$$\frac{1}{L_2}\int (V_c - V_b)dt = i \tag{B.3}$$

$$C_2\frac{d(V_d - V_b)}{dt} + \frac{V_d}{R_2} = 0 \tag{B.4}$$

Differentiating the above equations to remove the integrals. Followed by the use backward finite difference method, the equations are written as [2, 3]:

$$\tfrac{1}{R_1\Delta t}(V_a^t - V_a^{t-1}) + \tfrac{C}{\Delta t^2}(V_a^t - 2V_a^{t-1} + V_a^{t-2}) + \tfrac{1}{L_1}(V_a^t - V_b^t) = 0 \tag{B.5}$$

$$\tfrac{1}{L_1}(V_b - V_a) + \tfrac{C}{\Delta t^2}\left[(V_b^t - 2V_b^{t-1} + V_b^{t-2}) - (V_d^t - 2V_d^{t-1} + V_d^{t-2})\right] = \frac{i^t - i^{t-1}}{\Delta t} \tag{B.6}$$

$$\tfrac{C_2}{\Delta t}\left[(V_d^t - V_b^t) - (V_d^{t-1} - V_b^{t-1})\right] + \tfrac{1}{R_2}V_d^t = 0 \tag{B.7}$$

The equations can be solved for the unknowns V_a^t, V_b^t and V_d^t:

The resonance caused by the inductance and capacitance in the circuit is evident as shown in Figure B.2.

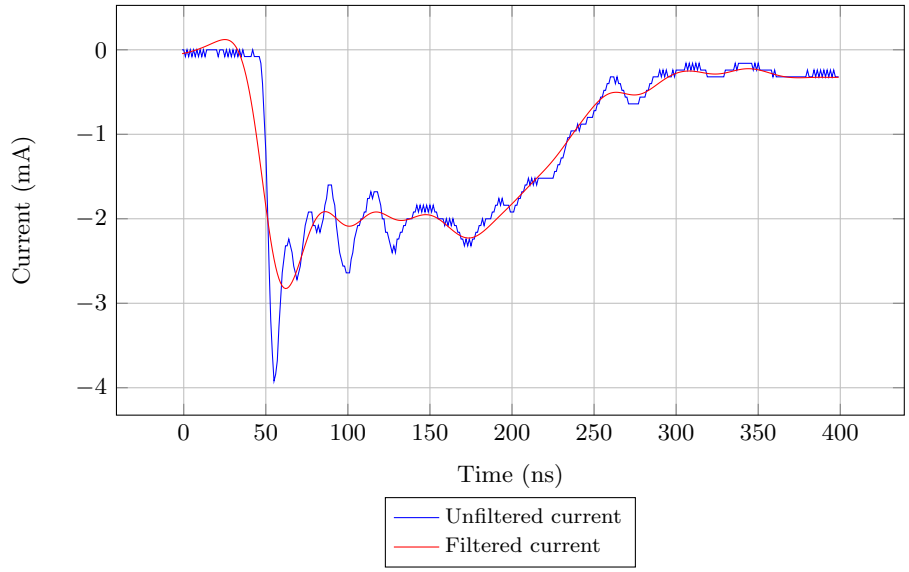

Figure B.2: Pulse Measured with Coupled Capacitor Circuit

B.2 Series Resistance Measurement Circuit

The series resistance measurement circuit is illustrated in Figure B.3.

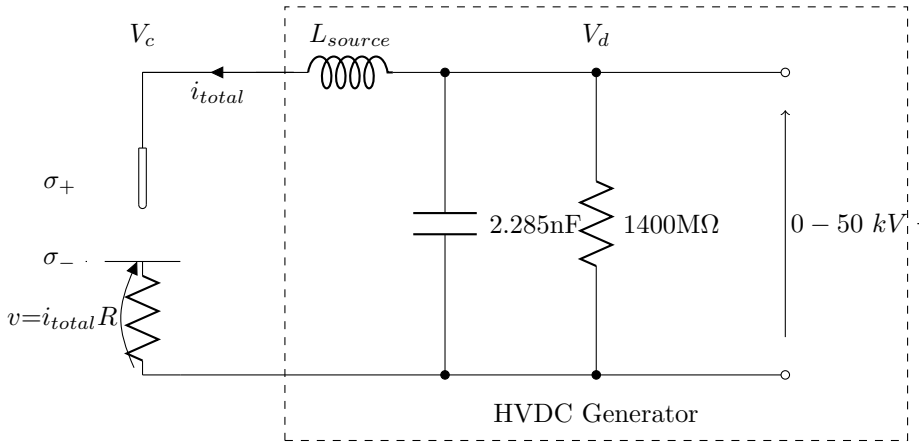

Figure B.3: Circuit with Series Resistance

Considering the series resistance measurement circuit, the inductance is ig-

nored as the resistance is dominant. The equation given by KVL is:

$$C\frac{dV_c}{dt} + \frac{V_c - V_d}{R} = 0 \tag{B.8}$$

Converting to a discrete form and solving gives:

$$V_d = iR + V_c - \frac{i\Delta t}{C} \tag{B.9}$$

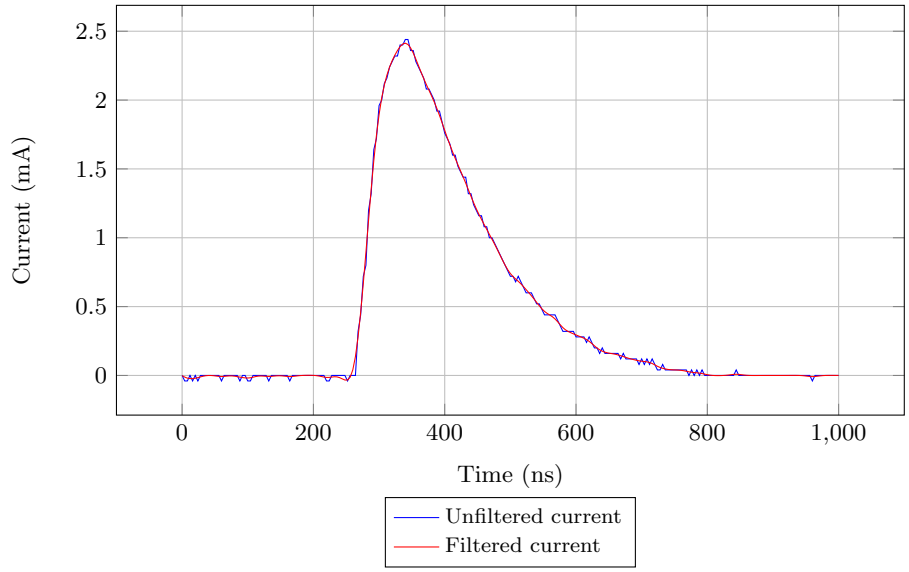

Figure B.4: Pulse Measured with Series Resistance Circuit

The resonance created by the addition of the coupling capacitor is removed by using the series resistance measurement circuit.

References

[1] A. Swanson, M. Grant, I. Hofsajer, and I. Jandrell. "HVDC Corona - Experimental Setup and Measurements." *International Symposium on High Voltage Engineering, Seoul, South Korea*, 2013.

[2] G. James. *Advanced Modern Engineering Mathematics*. Prentice Hall, second ed., 1999.

[3] S. Farlow. *Partial Differential Equations for Scientists and Engineers*. Dover Publications, Inc, first ed., 1993.

Appendix C

Kinetic Theory of Gases

Air is made up of gaseous components and water vapour, where the predominant gaseous elements include Nitrogen 78.1%, Oxygen 21% and Argon 0.9% [1]. The Bohr model of the atom is a simple yet useful model to understand the processes involved with the excitation and ionisation of the gas. The kinetic theory of gases is outlined in support of Chapter 2 and the studies on corona.

C.1 Bohr Model of an Atom

Bohr combined a number of theories including Planck's quantum theory, Einstein's photon theory of light, early models of the atom and Newtonian mechanics to provide a model for the atom [2].

Some of the basic principles of the model include [2]:

- the electron moves in circular orbits around the proton under the influence of the Coulomb force of attraction,
- certain orbits are stable and do not emit radiation energy,
- radiation is emitted when the electron jumps from a higher to a lower energy state given by $\Delta\varepsilon = h\nu$ (Figure C.1), and

- the size of the allowed electron orbit is determined by the condition imposed on the electron's orbital angular momentum, where the orbit is an integral multiple of $h' = h/2\pi$ given by $m_e vr = nh'$ (where $n = 1, 2, 3...$).

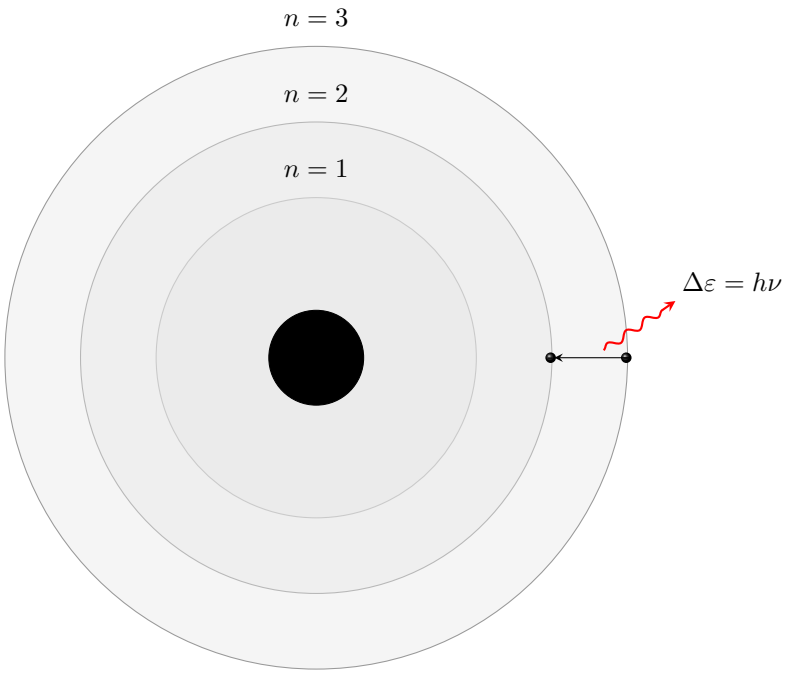

Figure C.1: Bohr Atomic Model

C.2 Macroscopic Model of an Ideal Gas (Classical Gas Laws)

Two important observations relating temperature, pressure and volume for an ideal gas include [2]:

- Boyle's Law - which states that when the gas is kept at a constant temperature, its pressure is proportional to its volume.
- Charles and Gay-Lussac Law - which states that when the pressure

of the gas is kept constant, its volume is directly proportional to its temperature.

These laws lead to the equation of state for an ideal gas, given by [2]:

$$PV = Nk_BT \tag{C.1}$$

Where:

P = Pressure [Pa]

V = Volume [m^3]

N = Total number of molecules

T = Temperature [K]

In general if more than gas is combined with initial volumes V_n, the total volume and total pressure are given by [3]:

$$V = \frac{n_1RT}{P} + \frac{n_2RT}{P} + ... + \frac{n_nRT}{P} \tag{C.2}$$

$$P = \frac{n_1RT}{V} + \frac{n_2RT}{V} + ... + \frac{n_nRT}{V} \tag{C.3}$$

C.3 Microscopic Model of an Ideal Gas

The kinetic theory of gases is a microscopic model of a gas and illustrates the relationship between the kinetic energy of molecular motion and the internal energy of a gas system. The model is simple as it is based on each model being a hard sphere, which assumes that each of the molecules does not interact with another except during collision and that they are not deformed by the collision. [2, 3].

A number of assumptions are made in developing the model including [2, 3]:

1. The gas consists of identical spherical molecules.

2. The number of molecules is large and the average distance between the molecules is greater than their diameter (i.e. the volume of the molecules is small compared to the volume of the container).

3. The molecules are in continuous random motion and obey Newton's Laws of Motion.

4. The collisions between molecules are elastic (i.e. both kinetic energy and momentum are constant).

5. The forces between the molecules are negligible.

Consider a gas with N molecules in a container with volume V and edges of length d. A single molecule will have a velocity $\vec{v}$ with components v_x, v_y and v_z. In an elastic collision with the wall of the container the v_x is reversed, while v_y and v_z remain unaltered; the change of momentum is described by [2, 3]:

$$\Delta p_x = -mv_x - (mv_x) = -2mv_x s \tag{C.4}$$

Where:
Δp_x = change in momentum [g.m/s]
m = mass of the molecule [g]
V_x = x-component of the velocity [m/s]

Application of the impulse momentum theory gives [2]:

$$F_1 \Delta t = \delta p_x = -2mv_x \tag{C.5}$$

Where:
F_1 = average of the force exerted by the wall on the molecule
Δt = change in time

The average force exerted by the wall on the molecule for each collision is given by [2]:

$$F_1 = \frac{-2mv_x}{\delta t} = \frac{-2mv_x}{2d/v_x} = \frac{-mv_x^2}{d} \tag{C.6}$$

By Newton's third law, the force exerted by the wall on the molecule is equal and opposite to the force exerted by the molecule on the wall; thus[2].

$$F_{1,onwall} = \frac{mv_x^2}{d} \tag{C.7}$$

Each of the N molecules in the container will have a velocity v_x, resulting in an average velocity of $\bar{v}_x^2$, thus the total force exerted on the wall is given by [2]:

$$F = \frac{Nm}{d}\bar{v}_x^2 \tag{C.8}$$

The average speed of all the molecules in the container is related to the averages of each of the components by the equation [2]:

$$\bar{v}^2 = \bar{v}_x^2 + \bar{v}_y^2 + \bar{v}_z^2 \tag{C.9}$$

The averages for each direction are equal, thus [2]:

$$\bar{v}^2 = 3\bar{v}_x^2 \tag{C.10}$$

Giving the total force exerted on the wall [2]:

$$F = \frac{N}{3}\left(\frac{m\bar{v}^2}{d}\right) \tag{C.11}$$

The pressure is proportional to the number of molecules per unit volume and to the average translational kinetic energy of the molecules and is given by

the expression [2]:

$$P = \frac{F}{A} = \frac{F}{d^2} = \frac{1}{3}\left(\frac{N}{d^3}m\bar{v}^2\right) = \frac{1}{3}\left(\frac{N}{V}\right)m\bar{v}^2 = \frac{2}{3}\left(\frac{N}{V}\right)\left(\frac{1}{2}m\bar{v}^2\right) \quad \text{(C.12)}$$

C.3.1 Temperature

Comparing the previous equation with the equation of state for an ideal gas, it can be seen that [2]:

$$PV = \frac{2}{3}N\left(\frac{1}{2}m\bar{v}^2\right) Nk_BT \quad \text{(C.13)}$$

By rearranging the equation, it becomes clear that the temperature is proportional to the average kinetic energy [2]:

$$T = \frac{2}{3k_B}\left(\frac{1}{2}m\bar{v}^2\right) \quad \text{(C.14)}$$

and the average kinetic energy per molecule is given by [2]:

$$\frac{1}{2}m\bar{v}^2 = \frac{3}{2}k_BT \quad \text{(C.15)}$$

The total translational kinetic energy of N molecules is N times the average energy per molecule [2]:

$$E_{trans} = N\left(\frac{1}{2}m\bar{v}^2\right) = N\frac{3}{2}k_BT = \frac{3}{2}nRT \quad \text{(C.16)}$$

C.4 Maxwell-Boltzmann Distribution

The distribution of molecular velocities is dependent on temperature and molecular weight of the gas, where the velocity u of the gas is based on a statistical distribution given by the Boltzmann-Maxwell distribution [3]:

$$f(u)du = \frac{dN_u}{N} = \frac{4}{\sqrt{\pi}}\left(\frac{u}{u_p}\right)^2\left[e^{-(u/u_p)^2}\right]\frac{du}{u_p} \quad \text{(C.17)}$$

Where u_p is the most probable velocity and dN_u/N is the relative number of particles with velocities in the range of u/u_p and $(u + du)/u_p$.

Where $f\left(\frac{u}{u_p}\right) = \frac{dN_u}{N}/\frac{du}{u_p}$ and the relative velocity is $u_r = u/u_p$, the velocity distribution is given by [3]:

$$f(u_r) = \frac{4}{\sqrt{\pi}} u_r^2 e^{-u_r^2} \tag{C.18}$$

$$\frac{dN_u}{N} = f(u_r)du_r \tag{C.19}$$

The average velocity is obtained by integrating from $0 \rightarrow \infty$ and is given by [3]:

$$\bar{u}_r = \int_{u_r=0}^{\infty} u_r f(u_r)du_r = \frac{4}{\sqrt{\pi}} \int_0^{\infty} u_r^3 e^{-u_r^2} du_r = \frac{2}{\sqrt{\pi}} \tag{C.20}$$

$$\bar{u} = \bar{u}_r u_p = 1.128 u_p \tag{C.21}$$

The rms or effective velocity is given by [3]:

$$(u_r)_{eff}^2 = \int_{u_r=0}^{\infty} u_r^2 f(u_r)du_r = \frac{4}{\sqrt{\pi}} \int_0^{\infty} u_r^4 e^{-u_r^2} du_r = \frac{3}{2} \tag{C.22}$$

$$\bar{u}_{eff} = \bar{u}_{reff} u_p = \sqrt{\frac{3}{2}} u_p = 1.224 u_p \tag{C.23}$$

The mean kinetic energy of a particle relates velocity to temperature, where there is no external influence, as follows [3]:

$$u_{eff} = \sqrt{\frac{3k_B T}{m}}; \bar{u} = \sqrt{\frac{8k_B T}{\pi m}}; u_p = \sqrt{\frac{2k_B T}{m}} \tag{C.24}$$

and

$$\frac{1}{2}mu_{eff}^2 = \frac{1}{2}m_e u_{eeff}^2 = \frac{1}{2}m_i u_{ieff}^2 = ... = \frac{3}{2}kT \tag{C.25}$$

Where m, m_e, m_i, u_{eff}, u_{eeff} and u_{ieff} are the masses and velocities of the gas molecules, ions and electrons respectively.

Table C.1: Mean molecular velocities at $20°C$ and 760 Torr

Gas	**Velocity $\bar{u}$ (m.s^{-1})**
Electron	100 x 10^3
Air	465

C.4.1 Free Paths of Molecules and Electrons

The free path is defined as the distance molecules or particles travel between collisions. The free path is a random value where the mean value is dependent on the density of the gas [3].

As illustrated in Figure C.2, considering a number of stationary particles of radius r_1 and a moving layer of particles of radius r_2, as the smaller particles move, the density will decrease due to scattering caused by collisions. The area for collision is given as $\pi(r_1 + r_2)^2$ and the unit volume or effective area is given as $N\pi(r_1 + r_2)^2$ [3].

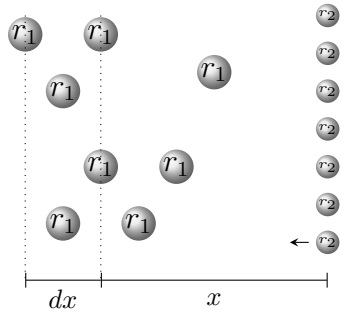

Figure C.2: Model for determining Mean Free Path

Considering a layer of thickness dx, a distance x from the origin and $n(x)$ particles, the decrease in moving particles due to scattering in layer dx is given by [3]:

$$dn = -n(x)N\pi(r_1 + r_2)^2 dx \tag{C.26}$$

Integration, with the number of particles having an initial value of n_0, gives [3]:

$$n(x) = N_0 e^{-N\pi(r_1+r_2)^2 x} \tag{C.27}$$

The mean free path [3]

$$\bar{x} = \bar{\lambda} = \int_{x=0}^{\infty} x f(x) dx = N\pi(r_1 + r_2)^2 \int_{x=0}^{\infty} x e^{-N\pi(r_1+r_2)^2} \tag{C.28}$$

and

$$\bar{\lambda} = \frac{1}{N\pi(r_1 + r_2)^2} = \frac{1}{N\sigma} = \frac{1}{Q} \tag{C.29}$$

Where $\sigma = \pi(r_1 + r_2)^2$, and is known as the cross-section for interception, and $Q = N\sigma$, and is the effective cross-section presented by molecules or particles for density of N molecules per volume [3].

Considering the various process and probabilities in a gas [3]:

$$Q = Q_{elastic} + Q_i + Q_e + Q_a + ... \tag{C.30}$$

Where:

$Q_{elastic}$ = cross-section for elastic collisions
Q_i = cross-section for ionization
Q_e = cross-section for excitation
Q_a = cross-section for attachment

For a gas where the particles are not stationary, the cross-section becomes

equal to the sum of all collisional cross-sections of the other particles in the gas, thus the mean free path of the particles [3]:

$$\bar{\lambda}_1 = \frac{1}{\pi \Sigma_{i=1}^{n} N_i (r_1 + r_i)^2 \sqrt{1 + \frac{m_1}{m_i}}} \tag{C.31}$$

For an atom in its own gas with $r = r_1 = r_2$ and $u_1 = u_2$ [3]:

$$\bar{\lambda}_a = \frac{1}{4\sqrt{2}\pi r^2 N} \tag{C.32}$$

and for an electron $r_1 << r_2$ and $m_1 << m_2$ [3]:

$$\bar{\lambda}_e = \frac{1}{\pi r_2^2 N} \tag{C.33}$$

Mean free path is related to pressure and temperature [3]:

$$\lambda(p, T) = \lambda_0 \frac{P_0}{P} \frac{T}{T_0} \tag{C.34}$$

Table C.2: Mean free paths at $15°C$ and 760 Torr

Gas	λ	**Molecular weight**
O_2	6.79	32.00
N_2	6.28	28.02

C.5 Distribution of Free Paths

The mean free path is given by [3]:

$$\bar{\lambda} = \frac{1}{N\pi(r_1 + r_2)^2} \tag{C.35}$$

The distribution function of the free paths is given by [3]:

$$\int_{n_0}^{n} dn = -\int_{x_0}^{x} \ln \frac{dx}{\bar{\lambda}} \tag{C.36}$$

and/or

$$n(x) = n_0 e^{-x/\bar{\lambda}} \tag{C.37}$$

Taking into consideration the collision cross-sections defined previously, the above equation can be rewritten [3]:

$$n = n_0 e^{-N\sigma x} \tag{C.38}$$

Where σ takes account of absorption and attachment.

C.6 Collision-energy Transfer

C.6.1 Elastic Collision

Collisions between particles are elastic where only kinetic energy is exchanged or inelastic where kinetic is partially converted into potential energy of the struck or striking particle [3].

Consider an elastic collision between two particles. The fractional energy loss is given by [3]:

$$\Delta(\theta) = \left(\frac{u_0^2 - u_1^2}{u_0^2} \right) \tag{C.39}$$

Where:

u_0 = initial velocity of striking particle

u_1 = velocity of striking particle after collision

θ = collision angle

From the equations for conservation of momentum and energy it can be

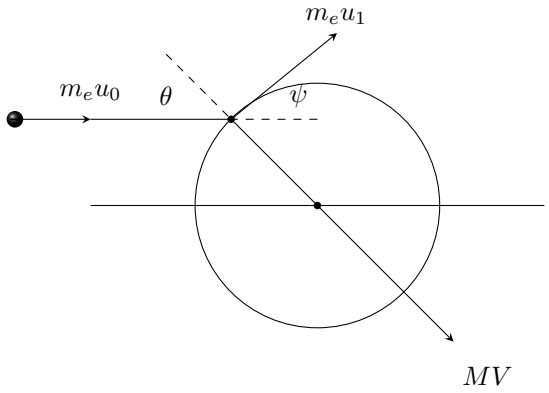

Figure C.3: Transfer of Energy in an Elastic Collision

shown that [3]:

$$mu_0 - mu_1 \cos\psi = MV\cos\theta \tag{C.40}$$

$$mu_1 \sin\psi = MV\sin\theta \tag{C.41}$$

$$\frac{1}{2}mu_0^2 - \frac{1}{2}mu_1^2 = \frac{1}{2}MV^2 \tag{C.42}$$

Where:

m = mass of striking particle

M = mass of struck particle

V = velocity of struck particle after collision

Rearranging the equations, it can be shown that [3]:

$$V = \frac{2mu_0\cos\theta}{m+M} \tag{C.43}$$

and [3]:

$$\Delta\theta = \frac{MV^2}{mu_0^2} = \frac{4mM\cos^2\theta}{(m+M)^2} \tag{C.44}$$

Considering the probability of collision at the angle of incidence of between

θ and $\theta + d\theta$, the mean fractional loss can be shown as [3]:

$$\overline{\Delta\theta} = \frac{2mM}{(m+M)^2} \tag{C.45}$$

C.6.2 Inelastic Collision

Following a similar approach to the energy transfer for an elastic collision and from the equations for conservation of momentum and energy for an inelastic collision it can be shown that [3]:

$$\frac{1}{2}mu_0^2 = \frac{1}{2}mu_1^2 + \frac{1}{2}MV^2 + W_p \tag{C.46}$$

$$mu_0 = mu_1 + MV \tag{C.47}$$

Where W_p is the Potential energy of the struck particle, transferred from the kinetic energy of the incoming particle [3]:

$$W_p = \left[m(u_0^2 - u_1^2) - \frac{m^2}{M}(u_0 - u_1)^2\right] \tag{C.48}$$

The maximum energy transfer is given when [3]:

$$\frac{dW_{pmax}}{du} = 0 \tag{C.49}$$

or

$$\frac{u_1}{u_0} = \frac{m}{m+M} \tag{C.50}$$

Where the ratio of the final to initial velocity of the incident particle equals the ratio of its mass to the sum of masses of the individual particles.

For an electron, where $m << M$, the maximum energy transferred is approximately equal to all of its kinetic energy and is given by [3]:

$$W_{pmax} \cong \frac{1}{2} \tag{C.51}$$

To cause ionisation the particle must have a kinetic energy of $\frac{1}{2}m_0^2 \geq eV_i$, where V_i is the ionisation potential of the atom or molecule [3].

C.6.3 Electric Fields

Coulomb's law states that the force between two charges q_1 and q_2 separated by a distance r is given by [2, 4]:

$$\vec{F_e} = k_e \frac{|q_1||q_2|}{r^2} \tag{C.52}$$

Where:

k_e = Coulomb's constant [8.9875×10^9 N.m^2/C^2]

The electric field E at a point in space is defined as the electric force F on a positive test charge q_0, and is shown by [2]:

$$\vec{E} = \frac{\vec{F_e}}{q_0} \tag{C.53}$$

At a point the total electric field of a group of charges is the sum of the electric fields of the individual charges, given by [2]:

$$\vec{E} = k_e \Sigma_i \frac{q_i}{r_i^2} \vec{r} \tag{C.54}$$

C.6.4 Motion of a Charged Particle in an Electric Field

Relating Newton's second law to a particle of charge q and mass m in an electric field gives the equation [2]:

$$\vec{F_e} = q\vec{E} = m\vec{a} \tag{C.55}$$

Giving the acceleration of the particle as [2]:

$$\vec{a} = \frac{q\vec{E}}{m} \tag{C.56}$$

References

[1] P. Sarma Maruvada. *Corona Performance of High Voltage Transmission Lines*. Taylor and Francis Group, 2000.

[2] R. Serway and R. Beichner. *Physics for Scientists and Engineers with Modern Physics*. Saunders College Publishing, fifth ed., 2000.

[3] E. Kuffel, W. Zaengl, and J. Kuffel. *High Voltage Engineering: Fundamentals*. Newnes, second ed., 2000.

[4] U. Inan and A. Inan. *Engineering Electromagnetics*. Addison Wesley Longman, Inc, 1999.

Appendix D

Plasma Physics

The definition of a plasma according to Chen is [1]:

"*A plasma is a quasineutral gas of charged and neutral particles which exhibits collective behaviour*".

Quasineutral means that while there are microscopically different species of charged particles within a plasma (electrons, positive ions and negative ions), macroscopically the plasma is electrically neutral. Due to the nature of the plasma and the local concentrations of charged particles within it, the plasma can exhibit collective behaviour, where the local concentrations create Coulombic forces which affect each of the other concentrations over a large region. A plasma is considered "collisionless" where the long-range electromagnetic forces on the particles are much greater than the forces due to the local collisions (as in the kinetic theory of gases), such that the local collisions can be neglected. Due to the range of temperatures within a plasma, it can be energetically considered to be fourth state of matter [1].

Plasmas are characterised by the charged particle density and the electron temperature. Gas discharges typically have a density range of $10^{14} < n < 10^{18}$ m^{-3} and an electron temperature of 2 eV [1].

D.1 Debye Length

Debye shielding is a phenomena in a plasma where the charged species (in particular electrons) will rearrange themselves into a sheath around other charged particles so as to shield out the electric fields. The Debye length is a measure of the sheath thickness and is given by [1, 2, 3]:

$$\lambda_D = \sqrt{\frac{\epsilon_0 k_B T}{n q_e^2}} \tag{D.1}$$

Where:

ϵ_0 = Permittivity of free space
k_B = Boltzmann's constant
n = Electron density
q_e = Electron charge

It has been shown that a grid structure Δx is related to the Debye length for stability of a simulation [3]:

$$\Delta x < \pi \lambda_D \tag{D.2}$$

D.2 Plasma Oscillations

Particle oscillations, plasma frequency or Langmuir waves are the oscillations of the charged particles [1, 2, 3]:

$$w_p = \sqrt{\frac{n q_e^2}{\epsilon_0 m_e}} \tag{D.3}$$

Where:

m_e = Electron mass

The time step in a discrete simulation should fulfil the criteria for stability [3]:

$$\Delta t \leq 0.1 \omega_p^{-1} \tag{D.4}$$

References

[1] F. Chen. *Introduction to Plasma Physics and Controlled Fusion Volume1: Plasma Physics*. Plenum Press, second ed., 1984.

[2] R. D. Blandford and K. S. Thorne. *Applications of Classical Physics*. California Institute of Technology, 2005.

[3] C. Birdsall and A. Langdon. *Plasma Physics via Computer Simulation*. Taylor and Francis Group, 1991.

Appendix E

Modelling

The drift-diffusion equation in one dimension for the electrons in a gas discharge is given by:

$$\frac{\partial N_e}{\partial t} = S + N_e\alpha|\vec{v}_e| - N_e\eta|\vec{v}_e| - N_eN_p\beta - \frac{\partial(N_e\vec{v}_e)}{\partial z} + \frac{\partial}{\partial z}\left(D\frac{\partial^2 N_e}{\partial^2 z}\right) \quad \text{(E.1)}$$

Where the equation consists of the source terms, drift and diffusion terms on the right hand side of the equation. A suitable algorithm is required to advance the equation in time and space.

Morrow et al in their work for drift diffusion equations derived methods to use the Shasta algorithm as defined by Boris and Book, together with non-uniform grids and implicit finite difference solvers [1, 2, 3, 4]. Their work proved the basis for modelling of gas discharges. The work is considered 1.5 dimensional (1.5D) due to the methods of solving the drift diffusion equations in 1 dimension and the electric field as a channel in a 2 dimensional system. The basics of the solver are described with the differences in the solver highlighted.

E.1 Drift-Diffusion Equation Solver

The flux corrected transport algorithm according to Zalesak is found to be more appropriate, extendable to more than one dimension and implementable [5, 6]. Consider the form of the transport equation for a fluid given by [5]:

$$w_t + f_x = 0 \tag{E.2}$$

In its general form the finite difference form in flux is written as [5]:

$$w_j^{t+1} = w_j^t - \tfrac{1}{\Delta x}\Delta t[F_{j+\frac{1}{2}} - F_{j-\frac{1}{2}}] \tag{E.3}$$

Where j and t represent space and time respectively, $\Delta x = \frac{1}{2}(x_{j+1} - x_{j-1})$ and $F_{j+\frac{1}{2}}$ are known as the transportive fluxes. As first order solutions tend to diffuse numerically and second order solutions tend to ring, the proposed method effectively combines the two to counter the numerical diffusion and remove the ringing. The algorithm follows the basic order.

1. Compute the low order transportive flux using the first order Lax Friedrich method

2. Compute the high order transportive flux using the Lax Wendroff method

3. Define the anti diffusive flux

$$A_{j+\frac{1}{2}} = F^H_{j+\frac{1}{2}} - F^L_{j+\frac{1}{2}} \tag{E.4}$$

4. Compute low order solution

$$w_j^{td} = w_j^t - \tfrac{1}{\Delta x}\Delta t[F^L_{j+\frac{1}{2}} - F^L_{j-\frac{1}{2}}] \tag{E.5}$$

5. Limit the anti-diffusive fluxes to avoid extremes

$$A^C_{j+\frac{1}{2}} = C_{j+\frac{1}{2}} A_{j+\frac{1}{2}} \tag{E.6}$$

6. Apply the limited anti-diffusive fluxes

$$w_j^{t+1} = w_j^{td} - \tfrac{1}{\Delta x}\Delta t[A^C_{j+\frac{1}{2}} - A^C_{j-\frac{1}{2}}] \tag{E.7}$$

E.1.1 First Order - Lax Friedrich

The Lax Friedrich method is a first order differential solution and is written in the general flux form as:

$$F_{j+\frac{1}{2}} = \frac{a}{2}[U_j^n + U_{j+1}^n] - \frac{\Delta x}{2\Delta t}[U_{j+1}^n - U_j^n] \tag{E.8}$$

E.1.2 Second Order - Lax Wendroff

The Lax Wendroff method is a second order differential solution of the drift diffusion equations and is written in the general flux form as:

$$F_{j+1/2} = \frac{1}{2}[f(U_j^n) + f(U_{j+1}^n)] - a^2\frac{\Delta t}{2\Delta x}[U_{j+1}^n - U_j^n] \tag{E.9}$$

The method is second order accurate in time and space.

E.1.3 Flux Correction

The anti-diffusive flux is to be limited to fulfil the criteria to avoid/dampen the extrema [5]:

$$A^C_{j+\frac{1}{2}} = C_{j+\frac{1}{2}} A_{j+\frac{1}{2}} \qquad 0 \leq Cj + \tfrac{1}{2} \leq 1 \tag{E.10}$$

In order to achieve this, a number of quantities are defined to prevent overshoot:

$$\begin{aligned} P_j^+ &= max(0, A_{j-\frac{1}{2}}) - min(0, A_{j+\frac{1}{2}}) && (E.11)\\ Q_j^+ &= (w_j^{max} - w_j^{td})\Delta x && (E.12)\\ R_j^+ &= min(1, Q_j^+/P_j^+) \quad \text{if} \quad P_j^+ > 0 && (E.13)\\ &= 0 \qquad\qquad\qquad\quad \text{if} \quad P_j^+ = 0 \end{aligned}$$

And similarly to prevent undershoot:

$$P_j^- = max(0, A_{j+\frac{1}{2}}) - min(0, A_{j-\frac{1}{2}}) \quad \text{(E.14)}$$

$$Q_j^- = (w_j^{td} - w_j^{min})\Delta x \quad \text{(E.15)}$$

$$R_j^- = min(1, Q_j^-/P_j^-) \quad \text{if} \quad P_j^- > 0 \quad \text{(E.16)}$$

$$= 0 \quad \text{if} \quad P_j^- = 0 \quad \text{(E.17)}$$

E.1.4 Diffusion

Diffusion is represented by the partial differential equation [7]:

$$\frac{\partial U}{\partial t} = \frac{\partial}{\partial x}\left(D\frac{\partial^2 U}{\partial^2 x}\right) \quad \text{(E.18)}$$

and can be numerically written as [7]:

$$\frac{U_j^{t+1} - U_j^t}{\Delta t} = D\frac{1}{\Delta x^2}(U_{j+1} - 2U_j + U_{j-1}) \quad \text{(E.19)}$$

E.1.5 Verification

Applying the individual methods and algorithms to the drift equation:

$$\frac{\partial N}{\partial t} = -W\frac{\partial N}{\partial x} \quad \text{(E.20)}$$

with a domain of $x = 0$ to 1 cm, speed of $W = -3 \times 10^8$ cm.s^{-1} and an applied distribution of $N = 1$ between 0.3 and 0.7 cm, the results indicate the following:

- The Lax Friedrich method produces the expected numerical diffusion and block nature.
- The Lax Wendroff method produces numerical ringing.
- The Flux Corrected method counters the numerical diffusion and removes the numerical ringing.

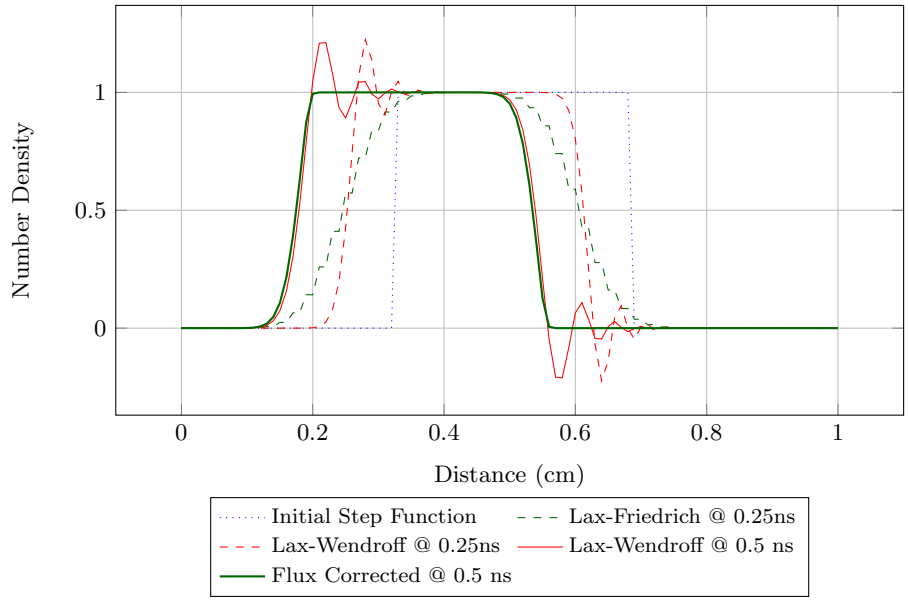

Figure E.1: Transport Method Test

E.1.6 Source Terms

The source terms for ionisation, attachment, and recombination are critical for the gas discharge and are included through a Runge-Kutta method similar to that of Morrow [1], where the difference is the source terms included.

The first step involves the convective term ΔN_c for a full time step and the introduction of an auxiliary step at half the time step [1]:

$$\Delta N_j^{t+\frac{1}{2}} = \frac{\Delta t}{2} S_j^t + \frac{1}{2} \Delta N_c \tag{E.21}$$

$$\Delta N_j^{t+1} = \Delta S_j^{j+\frac{1}{2}} + \Delta N_c \tag{E.22}$$

References

[1] R. Morrow. "Numerical Solution of Hyperbolic Equations for Electron Drift in Strongly Non-uniform Electric Fields." *Journal of Computational Physics*, 1981.

[2] R. Morrow and L. Crem. "Flux-Corrected Transport and Diffusion on a Non-uniform Mesh." *Journal of Computational Physics*, 1985.

[3] R. Morrow and J. Lowke. "Streamer propagation in air." *Journal of Physics D: Applied Physics*, vol. 30, 1997.

[4] J. Boris and D. Book. "Flux-corrected transport. I. SHASTA, a fluid transport algorithm that works." *Journal of Computational Physics*, 1973.

[5] S. Zalesak. "Fully Multidimensional Flux-Corrected Transport Algorithms for Fluids." *Journal of Computational Physics*, vol. 31, 1979.

[6] J. Shim, S. Choi, H. Hwang, H. Ha, K. Ko, and H. Kang. "2-D Simulation on the corona discharge of negative needle-to-plane electrodes." *IEEE Transactions on Magnetics*, vol. 38, no. 2, 2002.

[7] S. Farlow. *Partial Differential Equations for Scientists and Engineers*. Dover Publications, Inc, first ed., 1993.

Appendix F

Detector Calibration

In general, any optical detector is required to be calibrated, however, as the purpose of the experiment was to detect infrared at 1270 nm, the exact intensity was not required as the measurement would be relative. The tungsten lightbulb with clear glass has been shown to be an inexpensive source for calibration because of its wide emission range and known data [1]. Considering the emissivity (ε_t) of tungsten and the temperature of the filament, the spectral emittance (measured in photons.s^{-1}.cm^{-2}.cm^{-1}) of a blackbody filament is given by [1].

$$SE(\lambda, T) = \varepsilon_t(\lambda, T)\frac{2\pi c}{\lambda^4}\frac{1}{e^{hc/\lambda k_B T} - 1} \tag{F.1}$$

Where:

ϵ_0 = Permittivity of free space
k_B = Boltzmann's constant
h = Planks constant
c = Speed of light
ε_t = Emissivity of tungsten
T = Temperature

The spectral emittance of the tungsten element at 2800 K is plotted against wavelength, while the photosensitivity of the InGaAs photodiode detector is

superimposed. The output of the detector would be the integral of the light impacting on the photosensitive range of the detector (900 to 1700 nm).

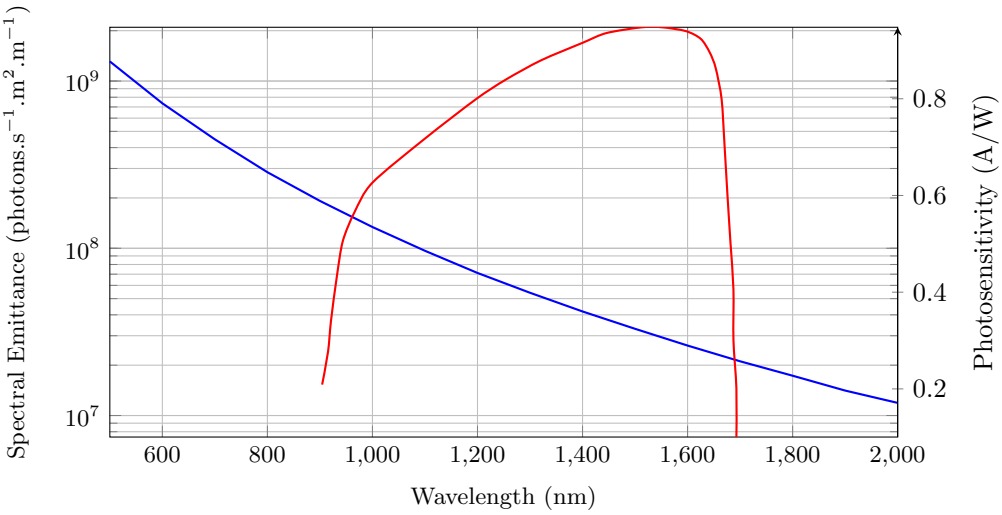

Figure F.1: Infrared Detector Calibration

The calibration of the detector was undertaken as shown in Figure F.2, with the incandescent light bulb positioned 0.5 m away from the source. The bulb had a rating of 60 W at 240 V and the supply voltage was varied from 0 to 225 V and the output voltage captured. The charge amplifier for the detector was set to low gain. The lens collected the scattered light and directed it to the sensor, ensuring a focused and higher output, which would be required as the emittance from corona was expected to be minimal. The 44 mV seen when there was no output from the light bulb is an offset, which could be corrected by tuning the charge amplifier.

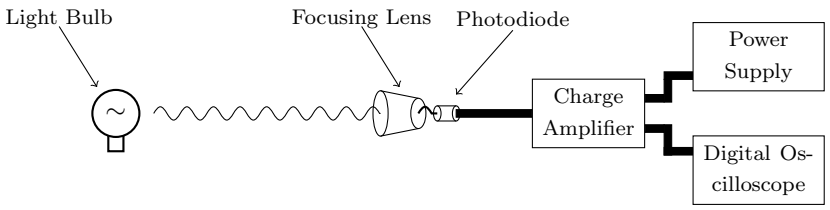

Figure F.2: Infrared Detector Calibration

Table F.1: Detector Calibration

Applied Voltage (V)	Power (W)	Sensor Output (V)	Sensor Output with Lens (V)
0	0	44m	44m
50	12.5	56m	140m
100	25	120m	1.02
125	31.25	172m	1.66
150	37.5	232m	2.64
200	50	376m	4.72
225	56.25	452m	5.68

References

[1] M. Kosch, S. Makinen, F. Sigernes, and O. Harang. "Absolute optical calibration using a simple tungsten light bulb: Experiment." *Proceedings of the 30th Annual European Meeting on Atmospheric Studies by Optical Methods*, 2003.

Appendix G

Code

The algorithm is coded and implemented in MATLAB.

G.1 Main Solver

```
function [Ne,Np,Nn,No] = fct_main(Ne_i,Np_i,Nn_i,No_i)

% Constants
eps = 8.85e-14;                 % [F/cm]
qe = -1.6e-19;                  % Electron Charge [C]
p = 760;                        % Pressure [torr]
ND = 101e3/(1.38e-23*293);      % Neutral Density P/kB/T [m-3]
Rep = 2e-7;                     % Recombination [cm3/s]
Rnp = 2e-7;                     % Recombination [cm3/s]
kd = 3e-10;                     % Excited and Negative Ion Recombination [cm3/s]
kq = 2.22e-22;                  % Excited Ion Quenching [cm3/s]
mup = 1*2.34;                   % Mobility of Positive Ions
mun = 1*2.7;                    % Mobility of Negative Ions
gamma = 0.01;                   % Secondary Ionisation due to Ion Bombardment
pq = 30;                        % PI - Quenching pressure
po = 0.22*p;

% Generic Data
T = 2000000;                    % Timesteps  max # is about 2147400000
dt = 2e-12;                     % Timestep [s]
gridT = 0:dt:T*dt-dt;
X = 800;                        % Grid Size
Xa = 0.02;                      % Position inner [cm]
Xc = 2.5;                       % Position outer [cm]
dx = 2.5/X;
gridX = (Xa:dx:Xc)';
dX = diff(gridX)';              % Grid Spacing Num = X - 1


Volt = 9000;                    % Applied Voltage [V]

X = length(gridX) + 2;

% Initialise Densities
Ne = zeros(X,1);
Np = zeros(X,1);
```

```
Nn = zeros(X,1);
No = zeros(X,1);

% Initialise Sources
Se = zeros(X,1);
Sp = zeros(X,1);
Sn = zeros(X,1);
So = zeros(X,1);
Sc = zeros(X,1);
Be = zeros(X,1);
Ae = zeros(X,1);
Sald = zeros(X,1);


% Initialise Photoionisation
Ip = zeros(X,1);
Pe = zeros(X,1);

% Initialise Diffusions
De = zeros(X,1);
Dp = ones(X,1);
Dn = ones(X,1);
Do = ones(X,1);

% Initialise Velocities
We = zeros(X-2,1);
Wp = zeros(X,1);
Wn = zeros(X,1);
Wo = zeros(X,1);

% Initialise Electric Field
E = zeros(X,1);
Er = zeros(X-1,1);
Ex = zeros(X-1,1);



% Initialise Voltage and Currents
I = zeros(1,T+1);
Ie = zeros(1,T+1);
Ii = zeros(1,T+1);
In = zeros(1,T+1);
Ib = zeros(1,T+1);

V = zeros(1,T+2);
Va = zeros(1,T+2);
Vb = zeros(1,T+2);
Vd = zeros(1,T+2);

% Create Seed Plasma
if Ne_i ==0
        Ne(2:X-1,1) = 1*exp(-(-gridX(1:X-2,1)+1).^2);
        Ni = Ne/2;
        Ne = Ni;
        Nn = Ne/2;
        Np = Ne;
else
        Ne = Ne_i;
        Np = Np_i;
        Nn = Nn_i;
        No = No_i;
end

[Ei,sigma_0,sigma_n] = fct_fsolve(0*qe*(Ne+Nn-Np),gridX,Volt,0,0);
Ei = Ei';
[muei, Dei, ioni, atti, exci] = bolsig_air (abs(Ei),ND);
```

```
for t = 1:T

t
t_loop = t/100;


Vv = Volt+V(t);

if Volt > 0
    Vv(Vv<0) = 0;
else
    Vv(Vv>0) = 0;
end

% Solve the Electric Field through Poisson's Equation 0,El(1,1)
Er = 1*fct_cylsolve(1*qe*(Ne+Nn-Np),gridX)';


Er(1:length(Er)-1,1) = Er(1:length(Er)-1,1)+diff(Er)/2;
Weight = ((1:length(Er)).^0.5)';
Weight = gridX/gridX(1)';


Er = Er./Weight.^2;

E = Er+Ei;

if Volt > 0
    E(E<0) = 0;
        Er(Er<0)= 0;
else
    E(E>0) = 0;
        Er(Er>0)= 0;
end


% Determine the Townsend Constants (alpha, eta, beta, We, De, etc)

[mue, De, ion, att, exc] = bolsig_air (abs(Ex),ND);


% Velocities

if abs(E) > 0
    We = -mue.*E;
    Wp = mup.*(E);
    Wn = -mun.*(E);
else
    We = -mue.*E;
        Wp = mup.*(E);
    Wn = -mun.*(E);
    De = Dei;
end


vNC = min(dX)^2/max(De)

CFL = max(abs(We))*dt/min(dX)

if isnan(CFL) || abs(CFL) > 1
    display('CFL')
    break
end

if isnan(vNC) || isinf(vNC)
    display('vNC')
    break
```

```
end

Debye = (pi*sqrt(100*eps*1.38e-23*1e4./(max(Ne*1e6).*qe.^2))*100)/min(dX)


% Solve the Drift-Diffusion Equation through FCT with Lax-W and Lax-F

Ne_p = fct(Ne,We,dX,De,0*Se,dt);
Np_p = fct(Np,Wp,dX,Dp,0*Sp,dt);
Nn_p = fct(Nn,Wn,dX,Dn,0*Sn,dt);

[Se,Sp,Sn,So] = fct_collision(Ne,Np,Nn,No,We,mue,mup,ion,att,exc,Rep,Rnp,kd,kq,gamma,gridX,dX,X,dx,Volt);

Se = dt/2*Se;
Sp = dt/2*Sp;
Sn = dt/2*Sn;
So = dt*So;

Ne = Ne_p'+Se;
Np = Np_p'+Sp;
Nn = Nn_p'+Sn;
No = No+So;


if Np(2:X-1,1) < 0
        display('problem')
end

if Nn(2:X-1,1) < 0
        display('problem')
end

Ne(Ne<0) = 0;
Ne(isnan(Ne)) = 0;
Np(Np<0) = 0;
Np(isnan(Np)) = 0;
Nn(Nn<0) = 0;
Nn(isnan(Nn)) = 0;
No(No<0) = 0;
No(isnan(No)) = 0;

% Solve the Current

Je = We(1:X-3,1).*Ne(2:X-2,1);
Jp = Wp(1:X-3,1).*Np(2:X-2,1);
Jn = Wn(1:X-3,1).*Nn(2:X-2,1);

Area = pi*Xa^2;

I(t+1) = Area*qe/(Volt)*sum((-Je+Jp-Jn).*Ei(1:length(Ei)-1,1).*dX');
Ie(t+1) = Area*qe/(Volt)*sum((-Je).*Ei(1:length(Ei)-1,1).*dX');
Ii(t+1) = Area*qe/(Volt)*sum((Jp).*Ei(1:length(Ei)-1,1).*dX');
In(t+1) = Area*qe/(Volt)*sum((-Jn).*Ei(1:length(Ei)-1,1).*dX');


if isnan(I(t+1))
    display('Current')
    break
end

% Solve the Circuit

V(t+1) = 1*(I(t+1)*1e3-I(t+1)*dt/3e-9);


if round(t_loop) == t_loop
    figure(1),subplot(2,3,1),semilogy(gridX(1:X-2,1),Ne(2:X-1,1),gridX(1:X-2,1),Np(2:X-1,1),
```

```
gridX(1:X-2,1),Nn(2:X-1,1),gridX(1:X-2,1),No(2:X-1,1))
    legend('elec','pion','nion','exc','all'),xlim([Xa Xc])%,ylim([1e0 1e12])
    subplot(2,3,2),semilogy(gridX(1:X-2,1),Ne(2:X-1,1),gridX(1:X-2,1),Np(2:X-1,1),
gridX(1:X-2,1),Nn(2:X-1,1),gridX(1:X-2,1),No(2:X-1,1))
    legend('elec','pion','nion','exc'),xlim([Xa 0.5]),ylim([1e-1 1e15])
    subplot(2,3,4),plot(gridX,Ei/1e3,gridX,E/1e3,gridX,
Er/1e3,gridX,Ex/1e3),xlim([Xa Xc])
    legend('initial','t','cylinder','x')
        subplot(2,3,5),plot(gridX,Ei/1e3,gridX,E/1e3,
gridX,Er/1e3,gridX,Ex/1e3),xlim([Xa 0.5])
    legend('initial','t','cylinder','x'),ylim([-100 100])
        subplot(2,3,3),plot(1e9*gridT(1,2:t),((Volt+V(1,2:t))/1e3))
    subplot(2,3,6),plot(1e9*gridT(1,2:t),1e3*I(1,2:t),1e9*gridT(1,2:t),1e3*Ie(1,2:t),
1e9*gridT(1,2:t),1e3*Ii(1,2:t),1e9*gridT(1,2:t),1e3*In(1,2:t))%,ylim([0 50])

        N_out(:,1) = gridX(1:X-2,1);
        N_out(:,2) = Ne(2:X-1,1);
        N_out(:,3) = Np(2:X-1,1);
        N_out(:,4) = Nn(2:X-1,1);
        N_out(:,5) = No(2:X-1,1);

        dlmwrite('N_out.txt',N_out,' ')

        E_out(:,1) = gridX;
        E_out(:,2) = E/1e3;
        E_out(:,3) = Er/1e3;

        dlmwrite('E_out.txt',E_out,' ')

        I_out(1:t,1) = dt*(1:t)/1e-9;
        I_out(1:t,2) = I(1,1:t)/1e-6;
        I_out(1:t,3) = Ie(1,1:t)/1e-6;
        I_out(1:t,4) = Ii(1,1:t)/1e-6;
        I_out(1:t,5) = In(1,1:t)/1e-6;

        dlmwrite('I_out.txt',I_out,' ')

end


end

        I_out(1:t,1) = dt*(1:t)/1e-9;
        I_out(1:t,2) = I(1,1:t)/1e-6;
        I_out(1:t,3) = Ie(1,1:t)/1e-6;
        I_out(1:t,4) = Ii(1,1:t)/1e-6;
        I_out(1:t,5) = In(1,1:t)/1e-6;

        dlmwrite('I_out.txt',I_out,' ')


 function [Ns] = fct(N,W,dX,D,S,dt)

[r,c] = size(N);

N = N';
W = W';
dX = dX;
D = D';
S = S';

% Initialise Solution Matrices
Nt = zeros(1,r);
Ns = zeros(1,r);

% Initialise Flux Limiters
```

```
phi_p1 = zeros(1,r);
phi_n1 = zeros(1,r);
phi_p2 = zeros(1,r);
phi_n2 = zeros(1,r);

P_p = zeros(1,r);
P_n = zeros(1,r);
Q_p = zeros(1,r);
Q_n = zeros(1,r);
R_p = ones(1,r);
R_n = ones(1,r);
C_p = zeros(1,r);
C_n = zeros(1,r);

N_max = zeros(1,r);
N_min = zeros(1,r);

%  Iterate through each element
for n = 2:r-2

%  Lower Order Solution for Drift - Lax-Friedrich
    F_hp = W*0.5*(N(n+1) + N(n)) - 0.5*dx/dt*(N(n+1) - N(n));
    F_hn = W*0.5*(N(n) + N(n-1)) - 0.5*dx/dt*(N(n) - N(n-1));

%  Lower Order Solution - Diffusion
    diffusion = dt*D(n-1)/dX(n-1)^2*(N(n+1)- 2*N(n)+ N(n-1));

%  Higher Order Solution for Drift - Lax-Wendroff
    F_hp = W*0.5*(N(n+1) + N(n))-W^2*dt/2./dX.*(N(n+1) - N(n));
    F_hn = W*0.5*(N(n) + N(n-1))-W^2*dt/2./dX.*(N(n) - N(n-1));

%  Anti-diffusive fluxes
    phi_p1(n) = (F_hp - F_lp);
    phi_n1(n) = (F_hn - F_ln);

%  Calculate solution
    Nt(n) = N(n) - dt/dX(n-1)*(F_lp-F_ln);

%  Iterate through flux correcting algorithm

   Nmax(n) = max([N(n+1),N(n),N(n-1),Nt(n+1),Nt(n),Nt(n-1)]);
   Nmin(n) = min([N(n+1),N(n),N(n-1),Nt(n+1),Nt(n),Nt(n-1)]);

   P_p(n) = max(0, phi_n1(n)) - min(0, phi_p1(n));
   P_n(n) = max(0, phi_p1(n)) - min(0, phi_n1(n));

   Q_p(n) = dX(n-1)*(Nmax(n)-Nt(n));
   Q_n(n) = dX(n-1)*(Nt(n)-Nmin(n));

   if P_p(n) > 0
    R_p(n) = min([1,Q_p(n)/(P_p(n)*dt)]);
   elseif P_p(n) == 0
    R_p(n) = 1;
   end

   if P_n(n) > 0
    R_n(n) = min([1,Q_n(n)/(P_n(n)*dt)]);
   elseif P_n(n) == 0
    R_n(n) = 1;
   end

   if phi_p1(n) >= 0;
     C_p(n) = min([R_p(n+1),R_n(n)]);
   elseif phi_p1(n) < 0
     C_p(n) = min([R_p(n),R_n(n+1)]);
   end
```

```
    if phi_n1(n) >= 0
      C_n(n) = min([R_n(n-1),R_p(n)]);
    elseif phi_n1(n) < 0
      C_n(n) = min([R_n(n),R_p(n-1)]);
    end

    phi_p2(n) = C_p(n)*phi_p1(n);
    phi_n2(n) = C_n(n)*phi_n1(n);

% Perform antidiffusion, add diffusion, add sources
     Ns(n) = Nt(n) - dt/dX(n-1)*(phi_p2(n)-phi_n2(n)) + diffusion + S(n);%

end
```

G.2 Electric Field Solver

```
function [EgridR,E0,Qa] = fct_fsolve(P,gridR,Volt,E,qa)%

  gridR = gridR';
  P = P';

  R = zeros(length(gridR),1); % [cm]
  dR = gridR(2)-gridR(1); % [cm]
  dX = diff(gridR);
  eps = 8.85e-14; %[F/cm]

  A = zeros(length(gridR),length(gridR));
  b = zeros(length(gridR),1);

  EgridR = zeros(1,length(gridR));


% Assign boundary conditions
  if E == 0
    A(1,1) = 1;
    A(1,2) = 0;
    b(1,1) = Volt;
    A(length(gridR),length(gridR))=1;
    A(length(gridR),length(gridR)-1)=0;
    b(length(gridR),1)=0;
  else
    A(1,1) = 1;
    A(1,2) = -1;
        b(1,1) = dX(1)*E;
    A(length(gridR),length(gridR))=1;
    A(length(gridR),length(gridR)-1)=0;
    b(length(gridR),1)=0;
  end


%% For each grid (assign a voltage and charge)
  for k = 2:length(gridR)-1
    A(k,k) = -2;
    A(k,k-1) = 1-dX(k)./gridR(k)/2;
    A(k,k+1) = 1+dX(k)/gridR(k)/2;
    b(k,1) = -dX(k)*dX(k)*P(1,k)/eps;
  end

  Vgrid = A\b;
  Vgrid = Vgrid';

  for k = 1:length(gridR)-1
    EgridR(1,k) = (Vgrid(1,k)-Vgrid(1,k+1))/dX(k);
  end

  EgridR(1,length(gridR))=EgridR(1,length(gridR)-1);

  EgridR(1,1);

  if E == 0
        Qa = EgridR(1,1)/eps;
        else
        Qa = 0;
  end
```

G.3 Poisson Electric Field Solver

```
function [Er] = fct_cylsolve (P,gridX)

gridX = gridX';
P = P';
dX = diff(gridX);
r = 1e-3;
eps = 8.85e-14;

[r,c] = size(gridX);

Er = zeros(1,c);
ft1 = zeros(1,c-1);
ft2 = zeros(1,c-1);
xt = zeros(1,c-1);


for l = 2:c-1

% Position of grid in relation to the grid
    xt(1,1:c-1) = (gridX(1,2:c)-gridX(1,l)); %[cm]
        xd = -gridX(1,l);

% Integration
    ft1 = xt./sqrt(xt.^2+r^2)-1;
        ft1 = P(2:c).*ft1.*dX(l-1);
    ft1(xt<0)=0;
        ft1(ft1>1)=1;
        ft1(isnan(ft1))=0;
        ft1(isinf(ft1))=0;


    ft2 = xt./sqrt(xt.^2+r^2)+1;
        ft2 = P(2:c).*ft2.*dX(l-1);
    ft2(xt>0)=0;
        ft2(ft2<-1)=-1;
        ft2(isnan(ft2))=0;
        ft2(isinf(ft2))=0;

    Er(1,l-1) = 1/2/eps*(sum(ft1)+sum(ft2));

end

        Er(isnan(Er))=0;
        Er(isinf(Er))=0;
```

G.4 Collision Solver

```
function [Se,Sp,Sn,So] = fct_collision(Ne,Np,Nn,No,We,mue,mup,ion,att,exc,Rep,Rnp,
kd,kq,gamma,gridX,dX,X,dx,Volt);

Se = zeros(X,1);
Sp = zeros(X,1);
Sn = zeros(X,1);
So = zeros(X,1);
Sc = zeros(X,1);
Be = zeros(X,1);
Ae = zeros(X,1);
Sa1d = zeros(X,1);

ND = 101e3/(1.38e-23*293);      % Neutral Density P/kB/T [m-3]
p = 760;
pq = 30;                        % PI - Quenching pressure
po = 0.22*p;

% Sources due to Collisions
Se(2:X-1,1) = (ion-att).*Ne(2:X-1,1).*abs(We) - Rep.*Ne(2:X-1,1).*Np(2:X-1,1)
+ kd*Nn(2:X-1,1).*No(2:X-1,1);
Sp(2:X-1,1) = ion.*Ne(2:X-1,1).*abs(We) - Rep.*Ne(2:X-1,1).*Np(2:X-1,1)
- Rnp.*Nn(2:X-1,1).*Np(2:X-1,1);
Sn(2:X-1,1) = att.*Ne(2:X-1,1).*abs(We) - Rnp.*Nn(2:X-1,1).*Np(2:X-1,1)
- kd*Nn(2:X-1,1).*No(2:X-1,1);
So(2:X-1,1) = exc.*Ne(2:X-1,1).*abs(We) - kd*Nn(2:X-1,1).*No(2:X-1,1)
- kq*0.22*ND*No(2:X-1,1);

% Sources due to Photoionisation

 Ip(2:X-1,1) = 0.2*(pq/(po+pq))*ion.*Ne(2:X-1,1).*abs(We);
 Ip(isnan(Ip))=0;
 Lp = downsample(Ip,2);
 gX = downsample(gridX,2);
 dPe = fct_photo(Lp,gX);
 Pe = interp(dPe,2);
 Pe = dX(1,1:X-3).^2.*Pe(1,1:X-3);

 Pe = Pe';

 Se(2:X-2,1) = Se(2:X-2,1) + Pe;
 Sp(2:X-2,1) = Sp(2:X-2,1) + Pe;

% Source due to Ion Bombardment
if Volt > 0
    Be(X-1,1) = 0*gamma*Np(X-2,1).*mup./mue(X-2,1);
else
    Be(2,1) = gamma*Np(2,1).*mup./mue(2,1);
end

Be(isnan(Be)) = 0;
Be(isinf(Be)) = 0;

Be = Be;

Se = Se+Be;

% Source due to Photoemission at cathode
if Volt > 0
else
Sc = fct_emission((ion).*Ne(2:X-1,1).*abs(We),gridX,2);
Sc = dx*Sc';
Se(2:X-1,1) = Se(2:X-1,1)+Sc(1:X-2,1);
end
```

```
% Source due to Background 10 to 20 pairs/cm3/s
Ae(2:X-1,1) = 10*ones(X-2,1);

 Se = Se+Ae;
 Sp = Sp+Ae;
```

G.5 Photoionisation Solver

```
function [Nphoto] = fct_photo (Iphoto,gridX)

gridX = gridX';
Iphoto = Iphoto';

[r,c] = size(gridX);

p = 760;                                    % [torr]
po = 0.22*p;

Nphoto = zeros(1,c);
Ntemp = zeros(1,c);
ft = zeros(1,c);
xt = zeros(1,c);

%% Photoionisation - Addition of electrons to model in all other zones except where the collisions happen??.

for l = 2:c

% Position of grid in relation to the grid
    xt(1,1:c-1) = (gridX(1,2:c)-gridX(1,l)); %[cm]
        xt(xt<0)=0;
%       xt = abs(xt);

% Absorbtion function in relation to the grid
    ft = (exp(-0.035*po*xt)-exp(-2*po*xt))./(xt*log10(2/0.035));
        ft(isnan(ft))=0;
        ft(isinf(ft))=0;
        ft(ft<0)=0;

 % Number of photo-electrons created in the grid due to all electrons created in other grids
        Ntemp = ft.*Iphoto(1,1:c)/4/pi./xt.^2;
        Ntemp(isnan(Ntemp))=0;
        Ntemp(isinf(Ntemp))=0;
        Ntemp(Ntemp<0)=0;

        % Total number of photo electrons in the grid
    Nphoto(1,l) = sum(Ntemp);

  end

        Nphoto(isnan(Nphoto))=0;
        Nphoto(isinf(Nphoto))=0;
        Nphoto(Nphoto<0)=0;
```

G.6 Photoemission Solver

```
function [Nphoto] = fct_emission (Iphoto,gridX,k)

gridX = gridX';
Iphoto = Iphoto';

if k > 2
    Iphoto = fliplr(Iphoto);
end


[r,c] = size(gridX);

p = 760;                                    % [torr]
po = 0.22*p;

Nphoto = zeros(1,c);
Ntemp = zeros(1,c);
ft = zeros(1,c);
xt = zeros(1,c);

%% Photoemission

% Position of grid in relation to the grid
    xt(1,1:c-1) = (gridX(1,2:c)); %[cm]

% Absorption function in relation to the grid
    ft = 0.001*Iphoto.*exp(-6*xt)/4/pi./xt.^2*pi;
        ft(isnan(ft))=0;
        ft(isinf(ft))=0;
        ft(ft<0)=0;

% Total number of photo electrons in the grid
    Nphoto(1,k) = sum(ft);

        Nphoto(isnan(Nphoto))=0;
        Nphoto(isinf(Nphoto))=0;
        Nphoto(Nphoto<0)=0;
```

G.7 Townsend and Transport Coefficient

```
function [mur, Dr, ion, att, exc] = bolsig_air (Er,N)

Er = Er;
% These values are calculated for p = 760 torr

O2 = 0.22;
N2 = 0.78;

% Electric field / N (Td) 1 Td = 1e-21 Vm2
E = [0,1,6.04,11.08,16.12,21.16,26.2,31.24,36.28,41.32,46.36,51.4,56.44,61.48,66.53,71.57,76.61,
81.65,86.69,91.73,96.77,101.8,106.8,111.9,116.9,122,127,132.1,137.1,142.1,147.2,152.2,
157.3,162.3,167.3,172.4,177.4,182.5,187.5,192.5,197.6,202.6,207.7,212.7,217.7,222.8,
227.8,232.9,237.9,242.9,248,253,258.1,263.1,268.1,273.2,278.2,283.3,288.3,293.3,298.4,
303.4,308.5,313.5,318.5,323.6,328.6,333.7,338.7,343.7,348.8,353.8,358.9,363.9,368.9,
374,379,384.1,389.1,394.2,399.2,404.2,409.3,414.3,419.4,424.4,429.4,434.5,439.5,444.6,
449.6,454.6,459.7,464.7,469.8,474.8,479.8,484.9,489.9,495,500,505,539.3,573.6,607.9,
642.2,676.6,710.9,745.2,779.5,813.8,848.1,882.4,916.7,951,985.3,1020,1054,1088,1123,
1157,1191,1226,1260,1294,1328,1363,1397,1431,1466,1500];

% Converts from Td to V/cm
E = E*N*1e-21/100;

% mobility x N [1/m/V/s]
mu = [6.44E+24,6.44E+24,2.59E+24,1.99E+24,1.77E+24,1.65E+24,1.58E+24,1.52E+24,
1.47E+24,1.43E+24,1.40E+24,1.36E+24,1.33E+24,1.31E+24,1.29E+24,1.27E+24,1.24E+24,
1.24E+24,1.22E+24,1.20E+24,1.19E+24,1.18E+24,1.16E+24,1.15E+24,1.14E+24,1.13E+24,
1.12E+24,1.12E+24,1.11E+24,1.10E+24,1.09E+24,1.08E+24,1.08E+24,1.07E+24,1.07E+24,
1.06E+24,1.05E+24,1.04E+24,1.04E+24,1.04E+24,1.04E+24,1.03E+24,1.03E+24,1.02E+24,1.01E+24,
1.01E+24,1.00E+24,9.98E+23,9.96E+23,9.91E+23,9.85E+23,9.80E+23,9.75E+23,9.71E+23,
9.66E+23,9.62E+23,9.58E+23,9.55E+23,9.51E+23,9.47E+23,9.44E+23,9.40E+23,9.37E+23,
9.34E+23,9.31E+23,9.28E+23,9.25E+23,9.21E+23,9.18E+23,9.15E+23,9.12E+23,9.10E+23,
9.07E+23,9.04E+23,9.01E+23,8.99E+23,8.96E+23,8.93E+23,8.91E+23,8.88E+23,8.85E+23,
8.83E+23,8.80E+23,8.78E+23,8.75E+23,8.73E+23,8.70E+23,8.68E+23,8.65E+23,8.63E+23,
8.61E+23,8.59E+23,8.57E+23,8.54E+23,8.52E+23,8.50E+23,8.48E+23,8.46E+23,8.44E+23,
8.42E+23,8.40E+23,8.38E+23,8.13E+23,7.98E+23,7.84E+23,7.70E+23,7.57E+23,7.46E+23,
7.35E+23,7.24E+23,7.14E+23,7.04E+23,6.95E+23,6.86E+23,6.78E+23,6.70E+23,6.62E+23,
6.55E+23,6.48E+23,6.41E+23,6.35E+23,6.28E+23,6.22E+23,6.17E+23,6.11E+23,6.05E+23,
6.00E+23,5.95E+23,5.90E+23,5.85E+23,5.81E+23,5.76E+23];

% -> cm2/V/s
mu = mu/N*100^2;

mur = interp1(E,mu,Er);
mur(isnan(mur))=0;%
if E > max(Er)
 mur = mu(1,1)
elseif E < min(Er)
 mur = mu(length(mu),1)
end
%mur(E>max(Er))=mu(length(mu),1);

% Mean energy (eV)
nrgy = [0,0.2247,0.7967,0.9565,1.014,1.047,1.071,1.093,1.118,1.152,1.199,1.262,
1.347,1.451,1.572,1.718,1.867,2.033,2.199,2.376,2.55,2.716,2.89,3.06,3.214,3.377,
3.528,3.672,3.816,3.954,4.079,4.205,4.334,4.461,4.572,4.678,4.78,4.884,5.007,5.113,
5.213,5.31,5.379,5.468,5.563,5.656,5.75,5.848,5.929,6.009,6.087,6.165,6.243,6.319,
6.398,6.476,6.553,6.63,6.705,6.781,6.855,6.93,7.005,7.078,7.15,7.222,7.293,7.364,
7.434,7.505,7.574,7.643,7.712,7.781,7.848,7.916,7.983,8.049,8.116,8.182,8.247,
8.312,8.377,8.442,8.506,8.571,8.635,8.698,8.762,8.825,8.889,8.952,9.014,9.077,
9.139,9.201,9.262,9.324,9.385,9.447,9.508,9.956,10.43,10.9,11.37,11.84,12.31,12.77,
13.23,13.69,14.15,14.61,15.07,15.53,15.99,16.45,16.9,17.36,17.82,18.27,18.73,19.19,
19.65,20.11,20.57,21.03,21.49,21.95,22.42,22.88,23.34];

energy = interp1(E,nrgy,Er);
```

```
energy(isnan(energy))=0;

%Diffusion coefficient x N [1/m/s]
D = [1.30E+24,1.30E+24,1.80E+24,1.89E+24,1.90E+24,1.90E+24,1.90E+24,1.90E+24,
1.89E+24,1.89E+24,1.90E+24,1.92E+24,1.95E+24,1.99E+24,2.05E+24,2.12E+24,2.19E+24,
2.28E+24,2.36E+24,2.45E+24,2.55E+24,2.63E+24,2.73E+24,2.82E+24,2.90E+24,2.99E+24,
3.07E+24,3.14E+24,3.22E+24,3.29E+24,3.36E+24,3.42E+24,3.49E+24,3.56E+24,3.61E+24,
3.66E+24,3.71E+24,3.76E+24,3.83E+24,3.88E+24,3.93E+24,3.98E+24,4.00E+24,4.04E+24,
4.09E+24,4.13E+24,4.18E+24,4.23E+24,4.26E+24,4.30E+24,4.33E+24,4.36E+24,4.39E+24,
4.43E+24,4.46E+24,4.49E+24,4.53E+24,4.56E+24,4.59E+24,4.62E+24,4.65E+24,4.68E+24,
4.72E+24,4.75E+24,4.78E+24,4.81E+24,4.84E+24,4.86E+24,4.89E+24,4.92E+24,4.95E+24,
4.98E+24,5.00E+24,5.03E+24,5.06E+24,5.08E+24,5.11E+24,5.14E+24,5.16E+24,5.18E+24,
5.21E+24,5.23E+24,5.26E+24,5.28E+24,5.31E+24,5.33E+24,5.35E+24,5.37E+24,5.40E+24,
5.42E+24,5.44E+24,5.47E+24,5.49E+24,5.51E+24,5.54E+24,5.56E+24,5.58E+24,5.60E+24,
5.62E+24,5.65E+24,5.67E+24,5.77E+24,5.92E+24,6.07E+24,6.21E+24,6.35E+24,6.49E+24,
6.62E+24,6.75E+24,6.88E+24,7.00E+24,7.13E+24,7.25E+24,7.37E+24,7.49E+24,7.61E+24,
7.73E+24,7.84E+24,7.96E+24,8.07E+24,8.18E+24,8.29E+24,8.41E+24,8.52E+24,8.63E+24,
8.74E+24,8.84E+24,8.95E+24,9.06E+24,9.16E+24,9.27E+24];

% -> cm2/s
D = D/N*100^2;

Dr = interp1(E,D,Er);
Dr(isnan(Dr))=0;

if E > max(Er)
 Dr = D(1,1)
elseif E < min(Er)
 Dr = D(length(D),1)
end

% Ionisation [m2]
a1d = [0,1.91E-25,5.98E-22,7.56E-22,7.15E-22,6.60E-22,6.14E-22,5.92E-22,5.96E-22,
6.33E-22,7.15E-22,8.41E-22,1.01E-21,1.20E-21,1.43E-21,1.67E-21,1.91E-21,2.13E-21,
2.35E-21,2.56E-21,2.74E-21,2.90E-21,3.06E-21,3.18E-21,3.28E-21,3.38E-21,3.45E-21,
3.51E-21,3.56E-21,3.60E-21,3.63E-21,3.65E-21,3.66E-21,3.67E-21,3.67E-21,3.67E-21,
3.66E-21,3.65E-21,3.65E-21,3.63E-21,3.62E-21,3.60E-21,3.58E-21,3.56E-21,3.54E-21,
3.51E-21,3.49E-21,3.47E-21,3.44E-21,3.42E-21,3.39E-21,3.37E-21,3.35E-21,3.32E-21,
3.30E-21,3.27E-21,3.25E-21,3.22E-21,3.20E-21,3.18E-21,3.15E-21,3.13E-21,3.11E-21,
3.08E-21,3.06E-21,3.04E-21,3.02E-21,2.99E-21,2.97E-21,2.95E-21,2.93E-21,2.91E-21,
2.89E-21,2.87E-21,2.85E-21,2.83E-21,2.81E-21,2.79E-21,2.77E-21,2.75E-21,2.73E-21,
2.71E-21,2.70E-21,2.68E-21,2.66E-21,2.64E-21,2.63E-21,2.61E-21,2.59E-21,2.58E-21,
2.56E-21,2.55E-21,2.53E-21,2.51E-21,2.50E-21,2.48E-21,2.47E-21,2.45E-21,2.44E-21,
2.42E-21,2.41E-21,2.31E-21,2.21E-21,2.12E-21,2.04E-21,1.96E-21,1.89E-21,1.82E-21,
1.76E-21,1.70E-21,1.65E-21,1.59E-21,1.54E-21,1.50E-21,1.45E-21,1.41E-21,1.38E-21,
1.34E-21,1.30E-21,1.27E-21,1.24E-21,1.21E-21,1.18E-21,1.15E-21,1.13E-21,1.10E-21,
1.08E-21,1.05E-21,1.03E-21,1.01E-21,9.92E-22];

ion_O = [0,0,0,0,0,1.66E-28,3.14E-27,2.23E-26,2.54E-27,1.62E-26,6.96E-26,2.25E-25,
5.97E-25,1.33E-24,2.66E-24,4.84E-24,8.09E-24,1.26E-23,1.87E-23,2.65E-23,3.62E-23,
4.78E-23,6.17E-23,7.76E-23,9.54E-23,1.16E-22,1.39E-22,1.63E-22,1.90E-22,2.19E-22,
2.50E-22,2.83E-22,3.18E-22,3.55E-22,3.94E-22,4.34E-22,4.77E-22,5.21E-22,5.68E-22,
6.16E-22,6.66E-22,7.17E-22,7.68E-22,8.22E-22,8.78E-22,9.35E-22,9.94E-22,1.05E-21,
1.11E-21,1.18E-21,1.24E-21,1.30E-21,1.37E-21,1.44E-21,1.51E-21,1.57E-21,1.64E-21,
1.71E-21,1.79E-21,1.86E-21,1.93E-21,2.01E-21,2.08E-21,2.16E-21,2.23E-21,2.31E-21,
2.39E-21,2.47E-21,2.55E-21,2.63E-21,2.71E-21,2.79E-21,2.87E-21,2.95E-21,3.04E-21,
3.12E-21,3.20E-21,3.29E-21,3.37E-21,3.46E-21,3.54E-21,3.63E-21,3.71E-21,3.80E-21,
3.89E-21,3.97E-21,4.06E-21,4.15E-21,4.24E-21,4.32E-21,4.41E-21,4.50E-21,4.59E-21,
4.68E-21,4.77E-21,4.86E-21,4.95E-21,5.04E-21,5.13E-21,5.22E-21,5.31E-21,5.90E-21,
6.62E-21,7.34E-21,8.08E-21,8.82E-21,9.56E-21,1.03E-20,1.11E-20,1.18E-20,1.25E-20,
1.33E-20,1.40E-20,1.47E-20,1.54E-20,1.61E-20,1.68E-20,1.75E-20,1.82E-20,1.89E-20,
1.95E-20,02E-20,2.08E-20,2.14E-20,2.21E-20,2.27E-20,2.33E-20,2.39E-20,2.45E-20,
2.50E-20,2.56E-20];

att_O = [3.5E-40,3.98E-40,4.82E-41,2.46E-29,1.01E-28,9.46E-27,1.23E-25,6.91E-25,
2.13E-24,5.46E-24,1.12E-23,1.96E-23,3.08E-23,4.38E-23,5.86E-23,7.51E-23,9.13E-23,
1.07E-22,1.22E-22,1.36E-22,1.48E-22,1.59E-22,1.70E-22,1.78E-22,1.84E-22,1.91E-22,
```

```
1.96E-22,2.00E-22,2.03E-22,2.06E-22,2.07E-22,2.08E-22,2.09E-22,2.09E-22,2.09E-22,
2.08E-22,2.08E-22,2.07E-22,2.06E-22,2.04E-22,2.03E-22,2.01E-22,1.99E-22,1.98E-22,
1.96E-22,1.94E-22,1.92E-22,1.90E-22,1.89E-22,1.87E-22,1.85E-22,1.83E-22,1.81E-22,
1.79E-22,1.77E-22,1.75E-22,1.73E-22,1.71E-22,1.70E-22,1.68E-22,1.66E-22,1.64E-22,
1.63E-22,1.61E-22,1.59E-22,1.58E-22,1.56E-22,1.54E-22,1.53E-22,1.51E-22,1.50E-22,
1.48E-22,1.47E-22,1.45E-22,1.44E-22,1.42E-22,1.41E-22,1.40E-22,1.38E-22,1.37E-22,
1.36E-22,1.34E-22,1.33E-22,1.32E-22,1.31E-22,1.30E-22,1.28E-22,1.27E-22,1.26E-22,
1.25E-22,1.24E-22,1.23E-22,1.22E-22,1.21E-22,1.20E-22,1.19E-22,1.18E-22,1.17E-22,
1.16E-22,1.15E-22,1.14E-22,1.08E-22,1.02E-22,9.61E-23,9.12E-23,8.67E-23,8.26E-23,
7.89E-23,7.55E-23,7.25E-23,6.96E-23,6.70E-23,6.46E-23,6.24E-23,6.03E-23,5.84E-23,
5.66E-23,5.49E-23,5.34E-23,5.19E-23,5.06E-23,4.93E-23,4.81E-23,4.70E-23,4.59E-23,
4.49E-23,4.40E-23,4.31E-23,4.22E-23,4.14E-23,4.07E-23];

ion_N = [0,0,0,0,0,4.95E-29,2.28E-27,1.91E-26,4.16E-30,6.76E-29,5.63E-28,3.09E-27,
1.28E-26,4.09E-26,1.11E-25,2.64E-25,5.58E-25,1.06E-24,1.88E-24,3.13E-24,4.93E-24,
7.39E-24,1.07E-23,1.50E-23,2.02E-23,2.68E-23,3.47E-23,4.39E-23,5.47E-23,6.72E-23,
8.12E-23,9.70E-23,1.15E-22,1.34E-22,1.56E-22,1.79E-22,2.04E-22,2.32E-22,2.62E-22,
2.93E-22,3.26E-22,3.62E-22,3.99E-22,4.38E-22,4.79E-22,5.23E-22,5.68E-22,6.15E-22,
6.64E-22,7.14E-22,7.67E-22,8.21E-22,8.77E-22,9.36E-22,9.95E-22,1.06E-21,1.12E-21,
1.18E-21,1.25E-21,1.32E-21,1.38E-21,1.45E-21,1.53E-21,1.60E-21,1.67E-21,1.75E-21,
1.82E-21,1.90E-21,1.98E-21,2.06E-21,2.14E-21,2.22E-21,2.30E-21,2.39E-21,2.47E-21,
2.56E-21,2.64E-21,2.73E-21,2.82E-21,2.91E-21,2.99E-21,3.08E-21,3.17E-21,3.27E-21,
3.36E-21,3.45E-21,3.54E-21,3.64E-21,3.73E-21,3.83E-21,3.92E-21,4.02E-21,4.11E-21,
4.21E-21,4.30E-21,4.40E-21,4.50E-21,4.60E-21,4.70E-21,4.79E-21,4.89E-21,5.54E-21,
6.33E-21,7.14E-21,7.95E-21,8.78E-21,9.60E-21,1.04E-20,1.12E-20,1.21E-20,1.29E-20,
1.37E-20,1.44E-20,1.52E-20,1.60E-20,1.67E-20,1.75E-20,1.82E-20,1.89E-20,1.96E-20,
2.03E-20,2.10E-20,2.16E-20,2.23E-20,2.29E-20,2.35E-20,2.42E-20,2.48E-20,2.53E-20,
2.59E-20,2.65E-20];


% m2 -> cm-1
a1d = a1d*N/100;
ion_O = ion_O*N/100;
att_O = att_O*N/100;
ion_N = ion_N*N/100;

a1dr = interp1(E,a1d,Er);
a1dr(isnan(a1dr))=0;
ion_Or = interp1(E,ion_O,Er);
ion_Or(isnan(ion_Or))=0;
att_Or = interp1(E,att_O,Er);
att_Or(isnan(att_Or))=0;
ion_Nr = interp1(E,ion_N,Er);
ion_Nr(isnan(ion_Nr))=0;

ion = O2*ion_Or + N2*ion_Nr;
att = O2*att_Or;
exc = O2*a1dr;
```

Appendix H

Experimental Setup and Results

H.1 Test Vessel

The test vessel is illustrated in Figure H.1, the test vessel was used for the majority of the experiments and applied in different manners. The electrodes consisted of:

- the brass rod with a diameter of 1 cm and a tip of 2.5 mm with an additional ball fitting at the top to prevent unwanted corona,
- the brass plate of diameter 9.85 cm located at the plane electrode (Gauss' law states that the plate will pick up a change in the state in-between the gap),
- the aluminium mesh with diameter of 15.75 cm and mesh aperture of 0.1cm acting as an side electrode (If the space charge is close to the mesh a change in flow will cause a small current to flow).

The side aluminium was connected to a tube that fit into the vacuum pump, slow moving air was ideal as it prevented turbulence.

For the needle plane experiments a needle replaced the rod and the gap length reduced to 9.5 cm.

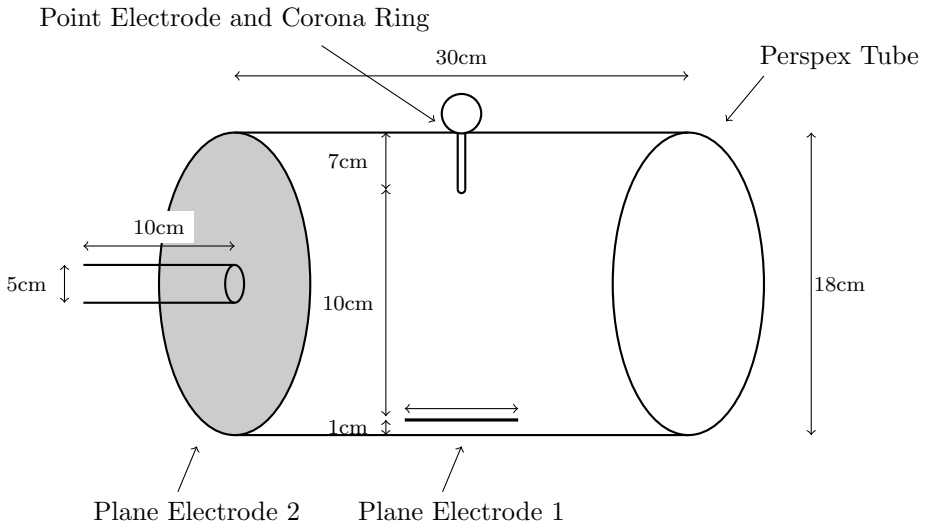

Figure H.1: Test Vessel

H.2 Initial Experiment

H.2.1 Measurement Procedure

The following measurement procedure was followed.

- Voltage was applied for 1 minute
- The repetition rate was sampled for 3 minutes where the highest and lowest repetition rates were recorded
- The airflow was applied for 1 minute
- The repetition rate was sampled for 3 minutes where the highest and lowest repetition rates were recorded
- The airflow was stopped
- The repetition rate was sampled for 2 minutes where the highest and lowest repetition rates were again recorded

H.2.2 Positive Corona

Temperature	25 °C
Pressure	(1700m)

Air Flow Speed		0 $m.s^{-1}$	
Supply Voltage (kV)	Repetition Rate (Hz)	Current Electrode 1 (μA)	Current Electrode 2 (μA)
37	460-510	2.44	72-188
37.5	50-106	2.40	40-65
39	Glow		Glow

Air Flow Speed		2.5 $m.s^{-1}$	
Supply Voltage (kV)	Repetition Rate (Hz)	Current Electrode 1 (μA)	Current Electrode 2 (μA)
37	460-510	2.44	72-188
37.5	50-106	2.40	40-65
39	Glow		Glow

H.3 Air Flow Experiment

H.3.1 Measurement Procedure

The following measurement procedure was followed.

- Voltage was applied for 1 minute
- The repetition rate was sampled for 3 minutes where the highest and lowest repetition rates were recorded
- The airflow was applied for 1 minute
- The repetition rate was sampled for 3 minutes where the highest and lowest repetition rates were recorded
- The airflow was stopped
- The repetition rate was sampled for 2 minutes where the highest and lowest repetition rates were again recorded

H.3.2 Positive Corona

Temperature	23.8 °C
Pressure	(1700m)
Relative Humidity	52.7

Air Flow Speed	0 $m.s^{-1}$		2.5 $m.s^{-1}$	
Supply Voltage (kV)	Repetition Rate (Hz)	Peak Current (mA)	Repetition Rate (Hz)	Peak Current (mA)
28	Burst corona		Burst corona	
29	Burst corona		Burst corona	
30	Burst corona		Burst corona	
31	Burst corona		Burst corona	
32	Burst corona		Burst corona	
33	623-678	2.12	Burst corona	
33.5	655-701	2.32	784-808	2.48
34	680-710	2.32	785-810	2.52
34.5	680-726	2.40	720-780	2.52
35	690-718	2.36	580-662	2.56
35.5	660-710	2.40	450-680	2.60
36	622-665	2.44	170-335	2.60
36.5	516-580	2.48	145-268	2.68
37	460-510	2.44	72-188	2.60
37.5	50-106	2.40	40-65	2.68
38	19-44	2.40	15-36	2.68
39	Glow		Glow	

Temperature	26 °C
Pressure	(1700m)
Relative Humidity	50.3

Air Flow Speed	0 m.s^{-1}		2.5 m.s^{-1}	
Supply Voltage (kV)	Repetition Rate (kHz)	Peak Current (μA)	Repetition Rate (kHz)	Peak Current (μA)
28	3.8-4.5	872	4.12-4.76	872
30	4.1-5.5	864	4.5-6.69	856
32	4.8-6.3	856	6.3-7.2	864
34	6.5-7.98	880	8.20-8.8	872
36	8.1-9.6	872	8.8-10.39	880
38	9.77-11.3	880	11.5-12.3	880
40	11.9-12.8	880	13.3-14.3	872
42	Breakdown			

H.3.3 Negative Corona

Temperature	24.4 °C
Pressure	(1700m)
Relative Humidity	48.5

Supply Voltage (kV)	Repetition Rate (kHz)	Peak Current (μA)
10	6.3-7.7	24
11	10-11.1	31.2
12	15-16.1	30.8
13	19.5-20.5	29.6
14	25.2-26	30
15	32.3-35.1	28.8
16	41.5-43.8	28.4
17	50.6-53.7	28
18	62.1-63.8	27.2
19	73.2-75.5	27.2
20	83.9-87.3	27.2
22	108.4-111.9	26.8
24	135.8-140.5	26.4
26	168.5-177.3	26.4
28	199-217.6	26
30	241-263.4	25.6
32	289-318.1	25.2
34	337.1-374.9	24.4
36	423.5-430.1	24
38	486.1-506.3	24
40	534.1-580.7	24

Temperature	25.5 °C
Pressure	(1700m)
Relative Humidity	46.5

Air Flow Speed	0 $m.s^{-1}$		2.5 $m.s^{-1}$	
Supply Voltage (kV)	Repetition Rate (kHz)	Peak Current (μA)	Repetition Rate (kHz)	Peak Current (μA)
10	16.1-25.6	29.6	14.8-15.2	29.2
12	24.9-25.8	28.8	23.8-24.8	28.8
14	37.2-38.2	28.4	34.8-36.8	28.4
16	52.4-53.5	28	48.4-50.1	28
18	68.3-69.6	27.6	63.2-66.1	27.6
20	86.4-88.8	27.2	81.9-84.9	27.2
24	136.5-138.8	26.4	131.5-135.9	26.4
26	165.1-168	26	162.3-165.4	26
28	198.2-200.8	26	195.1-203.7	25.6
30	238.9-240	25.6	236.1-240.9	25.6
32	279.1-291.9	26.4	288-291	25.6
34	377-390.1	24.4	344.2-353	24.4
36	420-486.1	22.8	420.4-446	24.4
38	537.8-568	21.6	486-505	22.4
40	575.6-622	21.6	533-568	22.4

Temperature	26.9 °C
Pressure	(1700m)
Relative Humidity	43.9

Air Flow Speed	0 $m.s^{-1}$	0.5 $m.s^{-1}$	1.5 $m.s^{-1}$	2.5 $m.s^{-1}$
Supply Voltage (kV)	Repetition Rate (Hz)	Peak Current (μA)	Repetition Rate (Hz)	Peak Current (μA)
10	15.4-17.4	27.2	14.4-15.4	27.4
20	85.18-88	26.8	76.7-80.2	280
30	234-236	24.8	222-236	25.6

Temperature	26.6 °C
Pressure	(1700m)
Relative Humidity	49.3

Air Flow Speed	0 $m.s^{-1}$	0.5 $m.s^{-1}$	1.5 $m.s^{-1}$	2.5 $m.s^{-1}$
Supply Voltage (kV)	Repetition Rate (Hz)	Repetition Rate (Hz)	Repetition Rate (Hz)	Repetition Rate (Hz)
10	18-19	16-18	14.5-16	14.5-16
14	40-42	37.8-39.8	37-38.8	34-36
18	72-75	71-74	66-69	63-66
22	110-118	115-116.6	107-108.9	94-108
24	130-135	131-133.5	126-129	119-123
28	189-195	192-193	184-186.9	170-174
30	224-228	224-227	217-220	197-209
32	264-268	262-264	253-258	236-243
34	299-308.9	303-304	291-294	266-279
36	325-339	317-325	314-317	301-304

H.4 Laser Excitation Experiment

H.4.1 Measurement Procedure

The following measurement procedure was followed.

- The laser was fired continuously into the gap
- Voltage was applied for 1 minute
- The repetition rate was sampled for 1 minutes where the highest and lowest repetition rates were recorded

Temperature	25 °C
Pressure	(1400m)

Laser Energy	800 mJ
Supply Voltage (kV)	Repetition Rate (Hz)
35	Burst corona
36	Burst corona
37	10
38	10-13
39	23-76
39.5	180-415
40	480-574
40.5	525-580
41	535-550

Laser Energy	0 mJ
Supply Voltage (kV)	Repetition Rate (Hz)
35	Burst corona
36	Burst corona
37	Burst corona
38	619-726
39	620-682
40	600-630
41	500-520
42	430-436
43	400
44	370
45	350

Laser Energy	800 mJ	118 mJ
Supply Voltage (kV)	Repetition Rate (Hz)	Repetition Rate (Hz)
35	Burst corona	20-40
36	Burst corona	50-78
37	Burst corona	500-660
38	30-90	690-725
39	600-650	717-740
40	600-650	684-692
41	500-530	530-560
42	430-440	450
43	390-400	400

Laser Energy	0 mJ	118 mJ
Supply Voltage (kV)	Repetition Rate (Hz)	Repetition Rate (Hz)
35	Burst corona	Burst corona
36	Burst corona	10
37	Burst corona	10-20
38	Burst corona	420-560
39	600-700	700-712
40	650-700	662-680
41	550-560	540-555
42	450-460	440-460
43	400	390-400

Appendix I

Associated Publications

"Investigation into HVDC corona: Discussion and initial modelling results", International Symposium on High Voltage Engineering, Hannover, Germany, August 2011. Swanson A and Jandrell I

"HVDC corona - Analysis of Corona through Modelling Techniques", International Symposium on High Voltage Engineering, Seoul, South Korea, August 2013. Swanson A, Grant M and Jandrell I

"HVDC corona - Experimental Setup and Measurement", International Symposium on High Voltage Engineering, Seoul, South Korea, August 2013. Swanson A, Grant M, Jandrell I and Hofsajer I